Federico Zenith

Control of fuel cells

Doctoral thesis
for the degree of philosophiæ doctor

Trondheim, June 2007

Norwegian University of Science and Technology
Faculty of Natural Sciences and Technology
Department of Chemical Engineering

NTNU

Norwegian University of Science and Technology

Doctoral thesis
for the degree of philosophiæ doctor

Faculty of Natural Sciences and Technology
Department of Chemical Engineering

This thesis was typeset in Palatino and AMS Euler by the author using LaTeX 2ε.

ISBN 978-82-471-1433-9 (printed version)
ISBN 978-82-471-1447-6 (electronic version)
ISSN 1503-8181

Doctoral theses at NTNU, 2007:65

Printed by NTNU-trykk

Abstract

This thesis deals with control of fuel cells, focusing on high-temperature proton-exchange-membrane fuel cells.

Fuel cells are devices that convert the chemical energy of hydrogen, methanol or other chemical compounds directly into electricity, without combustion or thermal cycles. They are efficient, scalable and silent devices that can provide power to a wide variety of utilities, from portable electronics to vehicles, to nation-wide electric grids.

Whereas studies about the design of fuel cell systems and the electrochemical properties of their components abound in the open literature, there has been only a minor interest, albeit growing, in dynamics and control of fuel cells.

In the relatively small body of available literature, there are some apparently contradictory statements: sometimes the slow dynamics of fuel cells is claimed to present a control problem, whereas in other articles fuel cells are claimed to be easy to control and able to follow references that change very rapidly. These contradictions are mainly caused by differences in the sets of phenomena and dynamics that the authors decided to investigate, and also by how they formulated the control problem. For instance, there is little doubt that the temperature dynamics of a fuel cell can be slow, but users are not concerned with the cell's temperature: power output is a much more important measure of performance.

Fuel cells are very multidisciplinary systems, where electrical engineering, electrochemistry, chemical engineering and materials science are all involved at various levels; it is therefore unsurprising that few researchers can master all of these branches, and that most of them will neglect or misinterpret phenomena they are unfamiliar with.

The ambition of this thesis is to consider the main phenomena influencing the dynamics of fuel cells, to properly define the control problem and suggest possible approaches and solutions to it.

This thesis will focus on a particular type of fuel cell, a variation of proton-exchange-membrane fuel cells with a membrane of polybenzimidazole instead of

the usual, commercially available Nafion. The advantages of this particular type of fuel cells for control are particularly interesting, and stem from their operation at temperatures higher than those typical of Nafion-based cells: these new cells do not have any water-management issues, can remove more heat with their exhaust gases, and have better tolerance to poisons such as carbon monoxide.

The first part of this thesis will be concerned with defining and modelling the dynamic phenomena of interest. Indeed, a common mistake is to assume that fuel cells have a single dynamics: instead, many phenomena with radically different time scales concur to define a fuel-cell stack's overall behaviour. The dynamics of interest are those of chemical engineering (heat and mass balances), of electrochemistry (diffusion in electrodes, electrochemical catalysis) and of electrical engineering (converters, inverters and electric motors). The first part of the thesis will first present some experimental results of importance for the electrochemical transient, and will then develop the equations required to model the four dynamic modes chosen to represent a fuel-cell system running on hydrogen and air at atmospheric pressure: cathodic overvoltage, hydrogen pressure in the anode, oxygen fraction in the cathode and stack temperature.

The second part will explore some of the possible approaches to control the power output from a fuel-cell stack. It has been attempted to produce a modularised set of controllers, one for each dynamics to control. It is a major point of the thesis, however, that the task of controlling a fuel cell is to be judged exclusively by its final result, that is power delivery: all other control loops, however independent, will have to be designed bearing that goal in mind.

The overvoltage, which corresponds nonlinearly to the rate of reaction, is controlled by operating a buck-boost DC/DC converter, which in turn is modelled and controlled with switching rules. Hydrogen pressure, being described by an unstable dynamic equation, requires feedback to be controlled. A controller with PI feedback and a feedforward part to improve performance is suggested. The oxygen fraction in the cathodic stream cannot be easily measured with a satisfactory bandwidth, but its dynamics is stable and disturbances can be measured quite precisely: it is therefore suggested to use a feedforward controller. Contrary to the most common approach for Nafion-based fuel cells, temperature is not controlled with a separate cooling loop: instead, the air flow is used to cool the fuel-cell stack. This significantly simplifies the stack design, operation and production cost. To control temperature, it is suggested to use a P controller, possibly with a feedforward component. Simulations show that this approach to stack cooling is feasible and poses no or few additional requirements on the air flow actuator that is necessary to control air composition in the cathode.

Acknowledgements

I would like to thank my supervisor, professor Sigurd Skogestad, for having offered me the opportunity of writing this work and for his support and patience in these four years.

This work would not have been possible without the collaboration of several professors, researchers and PhD students from the Department of Materials Technology at NTNU: I would like to thank professors Reidar Tunold and Børre Børresen and researchers Ole-Edvard Kongstein and Frode Seland, who were co-authors in my first paper, for their data, suggestions, and patience. Børre and Frode deserve additional thanks for helping me in obtaining the experimental data presented in chapter 2.

My thanks go to Helge Weydahl, also from the Department of Materials Technology and with whom I shared my office for three years, for many fruitful discussions, in particular about the electrochemical transient.

I would like to thank Steffen Møller-Holst from SINTEF for his invaluable efforts in coordinating various projects related to hydrogen and fuel cells.

I am thankful to all the colleagues I met during my stay at the Department of Chemical Engineering for creating a great work environment.

Finally, funding from Statoil AS and the Norwegian Research Council is gratefully acknowledged.

Contents

Abstract iii

Acknowledgements v

List of Figures xi

List of Tables xv

Notation xvii

1 Introduction 1
- 1.1 Thesis Overview . . . 1
- 1.2 Motivation . . . 2
- 1.3 Polybenzimidazole-Membrane Fuel Cells . . . 3
  - 1.3.1 Water Management in Nafion Membranes . . . 3
  - 1.3.2 Advantages of Polybenzimidazole Membranes . . . 4
- 1.4 Publications . . . 5
  - 1.4.1 Journal Articles . . . 5
  - 1.4.2 Conferences and Seminars . . . 6

I Dynamics of Fuel Cells 9

2 Experimental Measurements 11
- 2.1 Literature Review . . . 11
- 2.2 Laboratory Setup . . . 12
  - 2.2.1 Experimental Procedure . . . 13
  - 2.2.2 Uncertainty Analysis . . . 14
- 2.3 Results and Discussion . . . 15
  - 2.3.1 Polarisation Curve . . . 15

2.3.2 Resistance Steps . . . 16
2.3.3 Effect of Flow Disturbances . . . 18
2.4 Conclusions . . . 19

3 Electrochemical Modelling 23
3.1 Literature Review . . . 23
3.2 Modelling Principles and Assumptions . . . 24
3.3 Diffusion . . . 26
3.3.1 The Stefan-Maxwell Equations . . . 26
3.3.2 Simplified Diffusion . . . 27
3.3.3 Distributed Layer Thickness . . . 29
3.4 Calculating the Cell Voltage . . . 30
3.5 Dynamics . . . 33
3.6 Time Constants . . . 34
3.7 Parameter Estimation and Simulation . . . 36
3.8 Simulation . . . 38
3.9 Impedance Measurements . . . 38
3.10 Instantaneous Characteristics . . . 41
3.10.1 Transient Behaviour . . . 42
3.10.2 Graphical Representation of Time Constants . . . 44
3.11 Perfect Control of the Electrochemical Transient . . . 45
3.11.1 Implicit Limitations . . . 46
3.12 Conclusions . . . 46

4 Mass and Energy Modelling 49
4.1 Literature Review . . . 49
4.2 Mass Balances . . . 51
4.2.1 Dead-End Flows . . . 51
4.2.2 Open-End Flows . . . 52
4.3 Energy Balance . . . 57
4.3.1 Air Cooling . . . 57
4.3.2 External Heating for Cold Start-up . . . 58
4.3.3 Enthalpy-Balance Equations . . . 58
4.4 Cell Stacks . . . 60

II Control of Fuel Cells 65

5 Control Structure for Fuel Cells 67

5.1 Literature Review . . . 67
5.2 Dynamic Modes of Fuel Cells . . . 71
5.3 Controlling the Reaction Rate . . . 72
5.3.1 Manipulating the Reactant Feed . . . 73
5.3.2 Manipulating the External Circuit . . . 74
5.4 Controlling Reactant Concentrations . . . 75
5.5 Controlling Stack Temperature . . . 76
5.6 Conclusions . . . 77

6 Converter Control **83**
6.1 Choice of Converter Type . . . 84
6.2 Effects of Discontinuous Currents in the Input . . . 86
6.3 Identifying a Controlled Variable: DC Motors . . . 88
6.4 Pulse-Width Modulation . . . 91
6.4.1 Oscillation Frequency . . . 92
6.5 Pulse-Width Modulation: $\mathcal{H}_\infty$ Linear Control . . . 93
6.5.1 Plant Linearisation and Controllability Analysis . . . 94
6.5.2 Problem Formulation . . . 95
6.6 Pulse-Width Modulation: Feedforward Control . . . 101
6.6.1 Half-Delay Filtering . . . 102
6.7 Pulse-Width Modulation: Input-Output Linearisation . . . 104
6.7.1 Change of Variables . . . 105
6.7.2 Internal Dynamics . . . 107
6.7.3 Stabilisation of the Internal Dynamics . . . 109
6.7.4 Feedback with Input Bounds . . . 110
6.7.5 Feedforward with Internal Oscillation Dampening . . . 111
6.8 Switching Rules . . . 113
6.8.1 Control Rules . . . 114
6.8.2 Performance of the Switching Rules . . . 116
6.8.3 Computational Performance . . . 119
6.9 Conclusions . . . 120

7 Composition and Temperature Control **123**
7.1 Power Load on the Stack . . . 124
7.2 Pressure Control of Dead-End Flows (Anode) . . . 126
7.3 Composition Control of Open-End Flows (Cathode) . . . 130
7.3.1 Measurement Dynamics . . . 130
7.3.2 Time Constants of Composition Dynamics . . . 131
7.3.3 Feedforward Control . . . 131

7.3.4 Dimensioning Criterion Based on Actuator Power Consumption 133
7.4 Temperature Control 133
7.4.1 Optimal Reference Value for Temperature Control 135
7.4.2 Hydrogen in the Cathodic Flow as an Input Variable 136
7.4.3 Measurement Dynamics 136
7.4.4 Time Constants of Temperature Dynamics 137
7.4.5 Controller Synthesis and Simulation 137
7.4.6 Temperature Control with Hydrogen Combustion 140
7.5 Conclusions 143
7.5.1 Dimensioning Criteria 144

8 Conclusions **147**
8.1 Suggested Control Strategy 148
8.2 Further Work 149

A Model Code **151**

B $\mathcal{H}_\infty$ Synthesis Plots **153**

Index **161**

List of Figures

2.1 Laboratory setup for experiments 13
2.2 Experimental polarisation curve 15
2.3 Experimental steps in resistance 16
2.4 One particular resistance step 17
2.5 Voltage transients of resistance steps 18
2.6 Transients induced by oxygen flow 19

3.1 Composition profiles through a fuel cell 25
3.2 Simulated diffusion transient 27
3.3 Ideal and real layers 29
3.4 Ideal and real layers 30
3.5 Diagram of the fuel-cell model 33
3.6 Residual plot of parametric regression 36
3.7 Simulated transient 38
3.8 Simulated MOSFET transient 39
3.9 Impedance spectroscopy for a fuel cell 40
3.10 Polarisation curve and instantaneous characteristic 41
3.11 Phase-plane transients at current or voltage changes 42
3.12 Phase-plane transients at load changes 43
3.13 Graphical interpretation of the transient's driving force 45
3.14 Power overshoot at load changes 45

4.1 Flows in a fuel cell 50
4.2 Polarisation curves when consuming oxygen 55
4.3 Maximum power outputs from a fuel cell when consuming oxygen . 55
4.4 Flow layout for a PBI fuel cell 59
4.5 Air flow through fuel cells 61
4.6 Flow layout for a fuel-cell stack 62

5.1 Controlling a fuel cell with reactant flow . . . 68
5.2 Interactions of dynamics in fuel cells . . . 72
5.3 Linear control . . . 75
5.4 Proposed control structure . . . 78

6.1 Definition of duty ratio . . . 84
6.2 Scheme of a buck converter . . . 84
6.3 Scheme of a buck converter . . . 85
6.4 Scheme of a buck-boost converter . . . 86
6.5 Direct connection between fuel cell and converter . . . 87
6.6 Insertion of a capacitance between a fuel cell and a buck-boost converter 88
6.7 A typical model of a DC motor . . . 89
6.8 Cascade control layout . . . 91
6.9 Oscillations for constant duty ratio . . . 92
6.10 Weights for $\mathcal{H}_\infty$ synthesis . . . 96
6.11 $\mathcal{H}_\infty$ controller for various D . . . 98
6.12 $\mathcal{H}_\infty$-controlled system for various V_{in} and I_L . . . 100
6.13 Feedforward control by filtering of input D. . . . 101
6.14 The half-delay input filter . . . 103
6.15 Simulation of a series of steps with feedforward control . . . 103
6.16 Effect of disturbance with feedforward filter . . . 104
6.17 Values of ψ in the phase plane . . . 106
6.18 Effect of unstable internal dynamics, I . . . 108
6.19 Effect of unstable internal dynamics, II . . . 108
6.20 Steps in reference with oscillation dampening . . . 112
6.21 Step in disturbance with oscillation dampening . . . 112
6.22 Operating modes of a converter . . . 114
6.23 Switching rules . . . 116
6.24 Simulink implementation of the switching rules . . . 117
6.25 Transient for switching rules . . . 118
6.26 Case of zero reference and disturbance . . . 118

7.1 The New European Driving Cycle . . . 125
7.2 Effect of conversion on a cell's power output . . . 126
7.3 Cell conditions during the NEDC cycle . . . 127
7.4 Control diagram for pure hydrogen pressure in a dead-end manifold 128
7.5 Hydrogen pressure with a PI feedback controller and feedforward . . 129
7.6 Oxygen fraction with a feedforward controller . . . 132
7.7 Specific heats of main chemical species . . . 135

7.8 Performance of temperature control 139
7.9 Influence of composition control on temperature control 140
7.10 Air flow requirements of composition and temperature control 141
7.11 Start-up dynamics 142

8.1 Time scales of the dynamic modes of fuel cells 148
8.2 The suggested layout for control of a PBI fuel cell stack 149

B.1 $\mathcal{H}_\infty$ controller for various I_L 154
B.2 $\mathcal{H}_\infty$ controller for various V_{in} 155
B.3 $\mathcal{H}_\infty$ controller for various V_{in} and I_L 156
B.4 $\mathcal{H}_\infty$-controlled-system for various D 157
B.5 $\mathcal{H}_\infty$-controlled system for various I_L 158
B.6 $\mathcal{H}_\infty$-controlled system for various V_{in} 159

List of Tables

3.1 Dynamic model equations 34
3.2 Results of parameter regression 37

7.1 Parameters for vehicle dynamics 125

Notation

An effort has been made in this thesis to maintain unique and consistent meanings for most symbols. It was however decided to use the same symbol for more entities when the symbol is customary in both fields and its usage does not cause misunderstandings. In particular, both voltage and volume are usually denoted by the letter V: as they can occur simultaneously in a number of equations related to fuel cells, it was chosen to represent the least common of the two, volume, using the typeface $\mathcal{V}$.

A	Area	$[m^2]$
a	Activity	$[-]$
C	Capacitance	$[F]$
C_d	Drag coefficient	$[-]$
C_{rf}	Rolling friction coefficient	$[-]$
c_p	Molar specific heat	$[J/K\,mol]$
$\hat{c}_p$	Areal specific heat	$[J/K\,m^2]$
D	Diffusion coefficient	$[m^2\,s]$
	also Duty ratio	$[-]$
E	Reversible potential	$[V]$
F	Faraday constant	$[C]$
f	Frequency	$[Hz]$
g	Gravitational acceleration	$[m/s^2]$
	also Specific Gibbs free energy	$[J/mol]$
H	Enthalpy	$[J]$
$\dot{H}$	Enthalpy flow	$[W]$
h	Specific enthalpy	$[J/mol]$
I	Current	$[A]$
i	Current density	$[A/m^2]$
L	Inductance	$[H]$
k	Reaction constant	$[mol/m^2\,s]$
m	Mass	$[kg]$
N	Molar flux	$[mol/m^2\,s]$
n	Exchanged electrons	$[-]$
	also Number of moles	$[mol]$
$\dot{n}$	Molar flow	$[mol/s]$
P	Power	$[W]$
p	Pressure	$[Pa]$
	also Specific power	$[W/m^2]$
R	Ideal gas constant	$[J/mol\,K]$
	also Resistance	$[\Omega]$
r	Specific resistance	$[\Omega\,m^2]$
s	Laplace variable	$[rad/s]$
T	Period	$[s]$
	also Temperature	$[K]$
	also Torque	$[N\,m]$
t	Time	$[s]$
V	Voltage	$[V]$
$\mathcal{V}$	Volume	$[m^3]$
v	Velocity	$[m/s]$
X	Conversion	$[-]$
	also Reactance	$[\Omega]$
x	Molar fraction	$[-]$
Z	Impedance	$[\Omega]$

Greek Letters

α	Symmetry factor	$[-]$

ε	Porosity	[−]	ρ	Density	[kg/m^3]
ζ	Damping factor	[−]		*also* Probability density	[−]
η	Overvoltage	[V]	σ	Standard deviation	[−]
θ	Delay	[s]	τ	Time constant	[s]
Λ	Distributed thickness	[m]		*also* Tortuosity	[−]
λ	Equivalent layer thickness	[m]	Φ	Magnetic flux	[Wb]
μ	Mean	[−]	ω	Frequency	[rad/s]
ν	Stoichiometric coefficient	[−]			

Chapter 1

Introduction

1.1 Thesis Overview

This thesis is split in two main parts. The first part is on the dynamics of fuel cells, and the second one on how control can be applied.

The first part starts with some experiments pertaining the overvoltage dynamics of fuel cells, presented in chapter 2. Then, the following chapter interprets the results proposing a simplified electrochemical model, which is used to obtain estimates of four model parameters from experimental data. The model's structure is analysed to obtain a theorem proving that, under general assumptions, overvoltage dynamics poses no limit to the overall dynamic performance of the fuel cell. The cell is then studied from a process engineer's point of view, focusing on mass and energy balances. The effects of different cell-stacking configurations is also briefly considered.

The second part begins with chapter 5, in which an overall control strategy for fuel cells is outlined, selecting which control variables are suitable for the various control loops. The actual implementation of control strategies is presented in the two following chapters: chapter 6 considers the design of a controller for a DC/DC converter, whereas chapter 7 presents the control solutions for mass and energy balances.

The software written for this thesis is attached to the PDF version of this thesis, or can be obtained contacting the author. The terms of usage and installation instructions are given in appendix A.

1.2 Motivation

Fuel cells are devices that produce electric power by direct conversion of a fuel's chemical energy. They are being extensively studied in many research environments for the possibility they offer of converting energy without the losses associated with thermal cycles, thereby having the potential to increase efficiency. Compared to other power sources, they operate silently, have no major moving parts, can be assembled easily into larger stacks, and (when run on hydrogen) produce only water as a by-product.

Fuel cells are essentially *energy converters*. Fuel cells resemble batteries in many ways, but in contrast to them they do not store the chemical energy: fuel has to be continuously provided to the cell to maintain the power output.

Various designs for fuel cells have been proposed, the most popular being the proton-exchange-membrane fuel cell (PEM) (usually with a Nafion membrane), operating at temperatures up to about 100 °C, and the solid-oxide fuel cell (SOFC), operating at temperatures of about 800 °C or higher. Whereas the underlying principle is always to extract electricity without combustion, each design presents different problems and advantages, and has unique characteristics that make it more appropriate for different environments.

Fuel cells of various kinds have been proposed for many power-production tasks, ranging from pacemakers to power plants, but their adoption is still in its infancy. Most fuel cells are in research laboratories or in proof-of-concept applications, and no product powered by fuel cells has become commonplace on the market.

Possibly because of this focus on laboratory research, there has until recently not been much focus on control strategies for fuel cells. Because of the multidisciplinarity of the field, it has been common to investigate the control problem from one particular point of view, a common one being manipulating the gas flows entering the cell to control the power output. An objective of this thesis is to integrate previous work from different areas with new insights, in order to acquire a complete view of the control issues of fuel-cell systems.

A characteristic trait of fuel-cell research is how many fields it can involve. The reactions at the basis of its operation are the domain of electrochemistry, whereas the energy and mass balances implied in continuously feeding reactants to the cell belong to chemical engineering, which can also be involved in the pre-treating of reactants. Converting the cell's power output to the appropriate current and voltage requires the skills of electrical engineering. Applying control theory to such a multidisciplinary system is a challenging task.

1.3 Polybenzimidazole-Membrane Fuel Cells

More and more new types of fuel cells are appearing in the open literature. Whereas the most commonly researched are the Nafion-based PEM and solid-oxide fuel cells, many other types are being considered: some are older types that still present interesting aspects for researchers, such as the alkaline and molten-carbonate fuel cells, while others are entirely new concepts (such as microbial [1], formic-acid [2], and direct borohydride fuel cells [3]), or improvements of existing ones in various aspects, such as new electrolytes or catalysts for existing fuel cells.

This thesis does not intend to present control methods for all the currently studied designs: one-size-fits-all algorithms are unlikely to exist, given the large diversity in the characteristics of the various types of fuel cells. A particular type of fuel cell will therefore be selected.

In choosing the fuel cell to model in this thesis, various aspects have been considered. It was decided at an early stage that it should be a PEM cell, as these are among the best studied (also within the small body of fuel-cell control literature), and most comparable models in the literature deal with these. However, PEM cells whose membranes are Nafion-based, which is the case in the majority of publications, present a serious issue for control: water management. It was therefore decided to study another kind of PEM, but before discussing this we will illustrate the shortcomings of Nafion membranes from the point of view of the control engineer.

1.3.1 Water Management in Nafion Membranes

Nafion membranes rely on liquid water to conduct protons through the membrane, but water content varies during operation as a consequence of reaction and evaporation. Too low water content will compromise the conductivity of the membrane, whereas too much water will flood the cathode and block the reaction. As a result, the acceptable target window of cell temperature versus relative humidity in the cathode gas is uncomfortably small [4, 5]. Since cells are usually electrically connected in series to form stacks, the failure of a single cell to carry the stack current will have a disrupting effect on the whole stack: the more the cells in a stack, the larger the likelihood that such a failure will happen. In addition, the failing cell will still be subject to the current the rest of the stack is pushing through it, causing reverse electrolysis that may rapidly ruin the catalyst and force the cell to be replaced.

In practical applications, water management is dealt with by humidifying the gas flows entering the stack and forcing the cathode gas flow to pass all cathodic sides in series, to mechanically remove any liquid water: this is however feasible

only in very small stacks, as already noticed by Litz and Kordesch [6] in 1965: with many cells, the pressure drop rapidly increases to very high levels, with increasing costs and loss of efficiency of the fuel-cell system (Corbo et al. [7] claim that the energetic cost of the air compressor is by far the largest one among ancillary units). However, operating all cells in parallel, with all cells connected to the same entering and exiting manifolds, may block some cells where flooding is occurring: as the gases will take the path of least resistance, these cells will remain flooded. Again, because of the usual electrical series connections, flooding of a single cell can block the whole stack's current.

Any approach to manage a membrane's water content based on feedback control suffers from the fundamental problem that the liquid water content in each cell is difficult to measure: both dry-out and flooding will result in a drop in voltage. Schumacher et al. [5] suggested inferring flooding from drops in voltage, and dry-out from variations in a cell's impedance at 1 kHz. However, even being able to measure the water content, it is not obvious what should be done in case a cell is dry while another is flooded at the same time[1]: it would be necessary to add new manipulated variables, such as flow-regulating valves for each cell, and devise a complex control system.

1.3.2 Advantages of Polybenzimidazole Membranes

The newer polybenzimidazole membranes (PBI) offer an alternative to Nafion, with different opportunities and challenges. They do not rely on liquid water to transport protons through the membrane, but (in most cases) on phosphoric-acid doping [8, 9, 10, 11, 12, 13], which increases their conductivity from about 10^{-12} S/cm [14, 15] to 6.8×10^{-2} S/cm. Phosphoric-acid doped PBI fuel cells can function at temperatures as high as 200 °C [12].

Not relying on liquid water, PBI cells can operate well beyond 100 °C without any need for pressurisation: this generates a number of very interesting properties, in particular from the point of view of controllability [16]:

- As the phosphoric acid concentration does not change significantly over time[2], membrane conductivity is more predictable and reliable.

[1] This could easily happen if an entering air flow, passing through all the cells in series, were not pre-humidified and sufficiently turbulent: the first cells could dry out, whereas the last ones would be saturated with the vapour produced by the previous ones.

[2] In laboratory experiments, the anode gas is usually bubbled through H_3PO_4 before entering the cell to make up for any losses.

- Since water is produced in vapour form, cathode flooding cannot occur. It is also much easier to model diffusion with the Stefan-Maxwell equations, as all diffusing species are in gas phase: modelling the mass transport in Nafion fuel cells implies the difficulty of dealing with a separate liquid phase in a porous material.

- High temperatures increase anodic tolerance to poisons such as CO. CO is a common poison in hydrogen obtained by reforming, and must be kept below 10 ppm in Nafion-membrane fuel cells. At the higher temperatures made attainable by PBI membranes, tolerance was measured to be 3 % in hydrogen at current densities up to 0.8 A/cm^2 at 200 °C [17]. Since this reduces the purity constraint on the anode gas, there is no need for complex purification systems for reformate gases, their control loops and the losses in dynamic performance they would introduce.

- The higher temperatures of exhaust gases allow better stack cooling, since off-gases remove more heat. It could be possible to discard the separate and expensive cooling system that Nafion-based fuel cells require.

On the other hand, PBI membranes are a more recent technology than Nafion, and hence less material is available in the literature about their properties. PBI is not readily commercially available as Nafion is, and membranes have often to be prepared in-house, impairing the reproducibility of its properties.

Because PBI membranes have much better controllability properties compared to Nafion-based ones, it was decided that this thesis would concentrate on this type of fuel cells.

1.4 Publications

1.4.1 Journal Articles

- Federico Zenith and Sigurd Skogestad, *Control of fuel-cell power output*, Journal of Process Control 17 (2007) 333–347. Contains the proof of theorem 3.11.1 about perfect control of fuel cells, and the theory outlined in section 6.8 about control of DC/DC converters with switching rules.

- Federico Zenith, Frode Seland, Ole Edvard Kongstein, Børre Børresen, Reidar Tunold and Sigurd Skogestad, *Control-oriented modelling and experimental study of the transient response of a high-temperature polymer fuel cell*, Journal of Power Sources 162 (2006) 215–227. Presents the experimental data of chapter 2 and

most of the analysis of chapter 3, introducing the concept of instantaneous characteristic.

1.4.2 Conferences and Seminars

- Federico Zenith, *Control of Fuel Cells*, lecture at the Institute of Energy Technology of Aalborg University, December 13, 2006. It treats, albeit superficially, all chapters up to chapter 6.

- *Control of fuel cells—Power control with pulse-width modulation*, presentation at the Nordic Hydrogen Seminar 2006 in Oslo, Norway, February 7, 2006. Essentially the same as the presentation in Denmark on January 27, but delivered to a hydrogen-oriented audience rather than a control-oriented one.

- *Control of fuel cells connected to DC/DC converters*, presentation delivered at the 2006 Nordic Process Control Workshop in Lyngby, Denmark, January 27, 2006. Control of buck-boost converters by pulse-width modulation: half-delay feedforward technique.

- *Control of a fuel-cell powered DC vehicle motor*, paper and presentation delivered at the AIChE 2005 Annual meeting, November 2, 2005, in Cincinnati, OH, USA. Modelling and control of buck-boost converters by means of switching rules. Applications to cascade control of DC motors.

- *Dynamics and control of polybenzimidazole fuel cells*, paper and presentation held at the ECOS 2005 conference in Trondheim, Norway. Analysis of possible manipulated variables (air flow, rheostats, DC/DC converters). Simulation of impedance measurements for parameter estimation.

- *Dynamic modelling for control of fuel cells*, paper and presentation delivered at the AIChE 2004 Annual meeting, November 10, 2004, in Austin, TX, USA. Analytic expression of the time constants through an overvoltage transient, first presentation of the theorem of perfect control for overvoltage dynamics.

- *Modelling and control of fuel cells*, presentation delivered at the 12$^{\text{th}}$ Nordic Process Control Workshop, August 19, 2004, in Gothenburg, Sweden. Description of PBI fuel cells in a control perspective and presentation of laboratory results.

- *Modelling and experimental study of the transient response of fuel cells*, poster presented at the 9$^{\text{th}}$ Ulm Electrochemical Talks, May 17–18, 2004, in Neu-Ulm,

Germany. Presents an initial modelling of the transient in overvoltage caused by a step in the external circuit's resistance.

Bibliography

[1] Frank Davis and Séamus P. J. Higson. Biofuel cells—recent advances and applications. *Biosensors & Bioelectronics*, 22:1224–1235, 2007.

[2] S. Ha, Z. Dunbar, and R. I. Masel. Characterization of a high performing passive direct formic acid fuel cell. *Journal of Power Sources*, 158:129–136, 2006.

[3] George H. Miley, Nie Luo, Joseph Mather, Rodney Burton, Glenn Hawkins, Lifeng Gu, Ethan Byrd, Richard Gimlin, Prajakti Joshi Shrestha, Gabriel Benavides, Julia Laystrom, and David Carrol. Direct $nabh_4/h_2o_2$ fuel cells. *Journal of Power Sources*, 165:509–516, 2007.

[4] James Larminie and Andrew Dicks. *Fuel Cell Systems Explained*. Wiley, 1st edition, 1999.

[5] J. O. Schumacher, P. Gemmar, M. Denne, M. Zedda, and M. Stueber. Control of miniature proton exchange membrane fuel cells based on fuzzy logic. *Journal of Power Sources*, 129:143–151, 2004.

[6] Lawrence M. Litz and Karl V. Kordesch. Technology of hydrogen-oxygen carbon electrode fuel cells. In George J. Young and Henry R. Linden, editors, *Fuel Cell Systems*, volume 47 of *Advances in chemistry*, pages 166–187. American Chemical Society, 1965.

[7] P. Corbo, F. E. Corcione, F. Migliardini, and O. Veneri. Experimental assessment of energy-management strategies in fuel-cell propulsion systems. *Journal of Power Sources*, 157:799–808, 2006.

[8] J. S. Wainright, J.-T. Wang, D. Weng, R. F. Savinell, and M. Litt. Acid-doped polybenzimidazoles: A new polymer electrolyte. *Journal of the Electrochemical Society*, 142(7): L121–L123, July 1995.

[9] R. Bouchet, R. Miller, M. Duclot, and J. L. Souquet. A thermodynamic approach to proton conductivity in acid-doped polybenzimidazole. *Solid State Ionics*, 145:69–78, 2001.

[10] Hongting Pu, Wolfgang H. Meyer, and Gerhard Wegner. Proton transport in polybenzimidazole with H_3PO_4 or H_2SO_4. *Journal of Polymer Science*, 40(7):663–669, 2002.

[11] Alex Schechter and Robert F. Savinell. Imidazole and 1-methyl imidazole in phosphoric acid doped polybenzimidazole electrolyte for fuel cells. *Solid State Ionics*, 147: 181–187, 2002.

[12] Ronghuan He, Qinfeng Li, Gang Xiao, and Niels J. Bjerrum. Proton conductivity of phosphoric acid doped polybenzimidazole and its composites with inorganic proton conductors. *Journal of Membrane Science*, 226:169–184, 2003.

[13] Y.-L. Ma, J. S. Wainright, M. H. Litt, and R. F. Savinell. Conductivity of PBI membranes for high-temperature polymer electrolyte fuel cells. *Journal of the Electrochemical Society*, 151(1):A8–A16, 2004.

[14] Shaul M. Aharoni and Anthony J. Signorelli. Electrical resistivity and ESCA studies on neutral poly(alkylbenzimidazoles), their salts, and complexes. *Journal of Applied Polymer Science*, 23:2653–2660, 1979.

[15] Herbert A. Pohl and Richard P. Chartoff. Carriers and unpaired spins in some organic semiconductors. *Journal of Polymer Science A*, 2:2787–2806, 1964.

[16] Jianlu Zhang, Zhong Xie, Jiujun Zhang, Yanghua Tang, Chaojie Song, Titichai Navessin, Zhiqing Shi, Datong Song, Haijiang Wang, David P. Wilkinson, Zhong-Sheng Liu, and Steven Holdcroft. High temperature PEM fuel cells. *Journal of Power Sources*, 160:872–891, 2006.

[17] Qinfeng Li, Ronghuan He, Ji-An Gao, Jens Oluf Jensen, and Niels J. Bjerrum. The CO poisoning effect in PEMFCs operation at temperatures up to 200 °C. *Journal of the Electrochemical Society*, 150(12):A1599–A1605, 2003.

Part I

Dynamics of Fuel Cells

Chapter 2

Experimental Measurements

In order to study the response of a polybenzimidazole fuel cell to variable resistive loads, experiments were carried out on a PBI membrane-electrode assembly, prepared in-house at Department of Materials Technology of NTNU. The experiments focused on the electrochemical properties of the cell, and care was taken to avoid interference from temperature transients and reactant depletion.

2.1 Literature Review

One of the first investigations of the dynamic properties of low-temperature PEM fuel cells was published by Argyropoulos et al. [1, 2], who applied a series of currents through a direct methanol fuel cell. They noted how transients in voltage were quick and often overshot their steady-state value, yielding transient operation that was actually better than at steady state.

A series of tests on the effect of a manipulated reactant input for direct-methanol fuel cells was conducted by Sundmacher et al. [3], which highlighted the delay between reactant shut-off and its effect on cell voltage, in the range of 200 s. The authors assumed that current could be determined independently.

Johansen [4] studied the dynamics and control of a fuel cell with a polybenzimidazole membrane, using a transistor load. When changing the transistor load, he noted that transients in voltage were in the order of milliseconds. When using reactant feed instead, response would be quick only when increasing feed, and would be much slower when decreasing it.

Weydahl et al. [5] studied, in a similar fashion, the transients of alkaline fuel cells, this time with a resistive load, whose resistance was stepped between various values, identifying a characteristic path in the voltage-current plot. Weydahl's PhD

thesis [6] contains many other experimental measurements of the dynamics of both alkaline and PEM fuel cells under various conditions, with variable resistive loads, currents, gas flows and compositions.

Kallo et al. [7] performed a series of dynamic tests on a direct methanol fuel cell, identifying three main factors in the dynamic response: the charge double layer's capacitance, catalyst poisoning and reactant crossover.

It has been shown by Rao and Rengaswamy [8] that current does not change stepwise during specific transients, such as when changing the external resistance, but instead follows a certain pattern, which may be described as a step change followed by what appears to be an exponential relaxation.

Benziger et al. [9] investigated the behaviour of fuel cells with a slowly changing external resistance. Using a Nafion membrane, they noticed how the output voltage would rapidly change when passing a certain threshold value in the applied external resistance, in a way similar to the ignited state of CSTR reactors. They concluded that this discontinuity was due to the water balance, as an increased water content would swell the membrane and improve contact with the catalyst layer. Their studies concerned the time range of 10^3 to 10^4 seconds, which is far beyond the time range of transients in overvoltage.

The effect of a large number of parameters on a PEM fuel cell's performance was studied by Yan et al. [10], who concluded that the most influential parameters were inlet humidities and temperature.

2.2 Laboratory Setup

The laboratory setup is sketched in figure 2.1. The load was a variable-resistance board, implemented with two resistances in parallel; in series with one of these resistances, a switch could be opened and closed manually, changing the total resistance of the circuit. The value of the resistances could be selected manually from the 11 positions of two corresponding knobs. The resistance board had been previously developed by Helge Weydahl in a related study [5].

The cell could be kept at a given temperature by a custom-made external electric heater with a feedback control loop, consisting of a thermocouple and an electronic control unit (West 6400 1/16 DIN profile controller). It should be noted that, whereas the laboratory setup needed make-up heat because of its small size, an application will probably need cooling instead, since the reaction heat will be sufficient to maintain its temperature.

The fuel cell, with a membrane area of $2 \times 2\,\mathrm{cm}^2$, ran on 99.5 % hydrogen and 99.5 % oxygen, both at atmospheric pressure. Oxygen was fed to the cell directly,

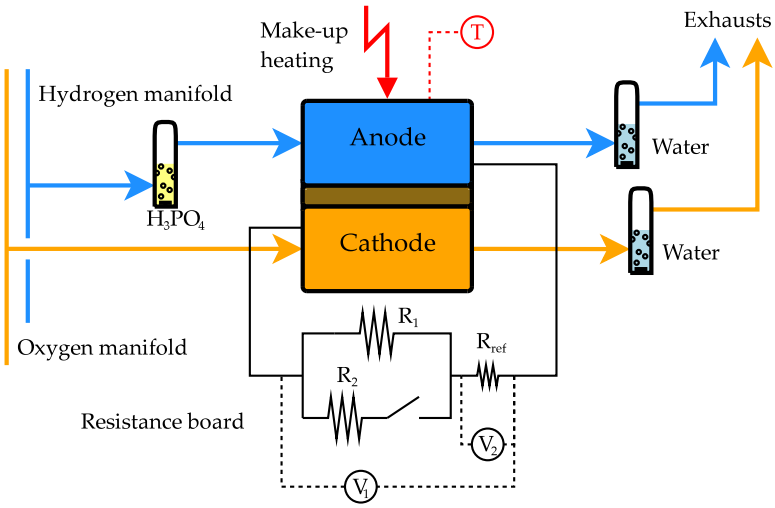

Figure 2.1: The laboratory setup for the experiments. Resistances R_1 and R_2 can be set to 11 different values each. The fuel cell's voltage is measured by voltmeter V_1 and passed to the data-acquisition unit. Resistance R_{ref}, known and fixed, is used to measure the current; its voltage is measured by V_2.

whereas hydrogen was bubbled through a 37.5 % H_3PO_4 solution, in order to make up for any loss of phosphoric acid in the cell's membrane. Both exhaust streams were bubbled through distilled water, to provide a simple visual feedback. All streams were controlled with a flow-control unit by Hi-Tek.

To acquire data, an Agilent 34970A data-acquisition unit was used; the data was later exported from its interface program to produce plots.

A polarisation curve for the cell was measured using a Wenking HP 96-20 potentiostat, whose voltage was set by a Wenking MVS 98 Scan Generator. When measuring the polarisation curve, the potentiostat substituted the resistance board in figure 2.1.

2.2.1 Experimental Procedure

Some general conditions were maintained in all tests:

- The cell was kept at a constant temperature of 150 °C;
- The oxygen flow was kept at 3.7 cm^3/s;
- The hydrogen flow was kept at 5.8 cm^3/s.

Since the data acquisition unit could only make voltage measurements, the current passing through the circuit was always calculated from the voltage over a known, small resistance, integrated in the resistance board. The voltages measured by the data-acquisition unit and the times at which they were taken were the only measurement recorded. In order to have synchronous data for current and voltage, the time vectors associated with current and voltage outputs were merged; each of the outputs was then linearly interpolated on the merged time vector.

For variable-resistance tests, the fuel cell was connected to the resistance board. After having reached steady state in cell temperature and voltage, the data acquisition unit was turned on and the board's switch was flipped. For consecutive tests, the switch could be flipped again after reaching a steady state in voltage. The data could then be saved as a comma-separated value file. To obtain maximum detail, the data-acquisition unit was set to record data as fast as possible (about every 0.1 seconds).

To obtain a polarisation curve, the fuel cell was connected to the potentiostat instead of the resistance board. Because of the slow secondary dynamics, the measurement took about 18 hours: the potentiostat cycled between 0.825 and 0 V at a sweep rate of 25 µV/s. In order to obtain a manageable number of data points, the data-acquisition unit was set to record data every 10 seconds.

The MEA was prepared as described in Seland et al. [11], and it was tested in a commercially available fuel cell (ElectroChem, Inc.) with one reference electrode probe, double serpentine flow field, originally designed for low-temperature PEM fuel cells.

2.2.2 Uncertainty Analysis

The preparation of the membrane-electrode assembly is likely to have a major impact on the fuel cell's properties. Since PBI membranes are not commercially available in standard form, the variability encountered in reproducing the membrane may impair the reproducibility of the measurements reported in this thesis.

The influence of oxygen flow might depend on the number and shape of the cathode channels. Precision in hydrogen flow, instead, has been found to be of little consequence. The performance of the flow controllers and of the temperature controller will also influence the resulting data, but this will result in systematic error rather than uncertainty.

The precision with which the board's resistances are known is going to have a direct influence the reliability of the measurements of current. Any unaccounted nonlinearities would also disturb the measurements.

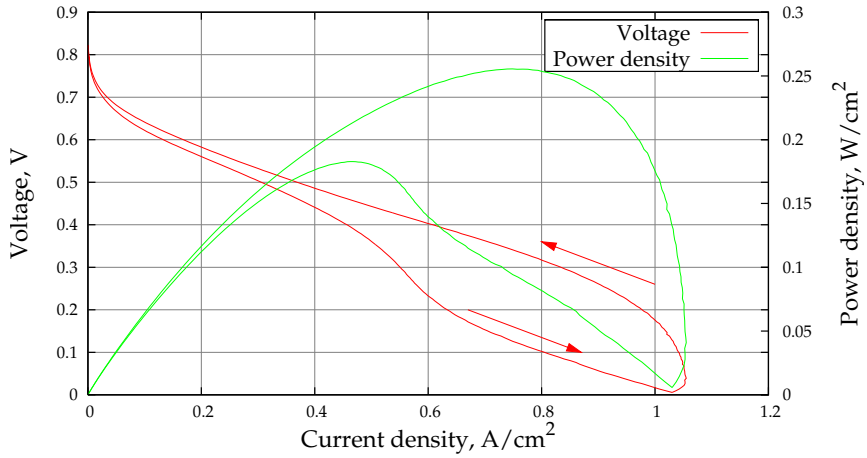

Figure 2.2: Experimental polarisation curve of a PBI fuel cell at 150 °C, measured with a sweep rate of 25 µV/s. The arrows indicate the direction of the hysteresis cycle.

Some transients had time constants in the same order of magnitude or even faster than the sampling rate. It is possible that some important points might be missed if a fast transient is not sampled with a sufficiently fast sensor, resulting in a significantly different shape of the measured transient.

2.3 Results and Discussion

2.3.1 Polarisation Curve

The polarisation curve obtained at the conditions described in the previous section is shown in figure 2.2. It presents a fairly large hysteresis, a behaviour previously observed in other experiments on similarPBI cells [12].

Liu et al. [12] showed that the cathodic reaction is first-order with respect to the concentration of H^+ ions, which depends on the partial pressure of water vapour: it might then be tempting to blame the hysteresis on the lag in water formation. However, given how slowly the polarisation curve was sampled, this is unlikely to be the only reason. Likewise, temperature transients, caused by the varying power output, should not have influenced such a slow sampling. Other possible causes include changes in the access of oxygen to the reaction sites or changes in the catalyst during the cycle.

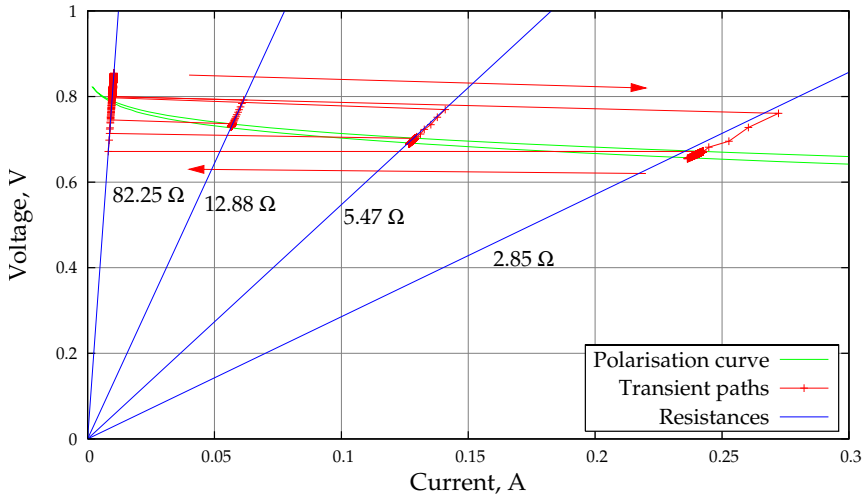

Figure 2.3: Path of experimental operating points in the V-I diagram after step changes in the external circuit's resistance, starting from 82.25 Ω and then switching back. The arrows indicate the path in the V-I plane, and the markers are spaced by about 0.06 s.

2.3.2 Resistance Steps

The results obtained by switching from an initial resistance to a smaller one and back are shown in figures 2.3 and 2.4. It can be seen how the operating point moves from one resistance's characteristic to the other along almost parallel, straight lines. The reason why the lines are not exactly parallel might be that sampling is not continuous, and the operating point might have moved from the initial point on the new resistance characteristic by the time a new sample is measured.

As a reference, the polarisation curve is plotted as well. The last transient is not exactly on the expected characteristic of its external resistance, most likely due to imprecision in the calculation of the resistance value.

It is clear that some transients are faster than others in the descent to steady-state; this can be seen by the number of markers, roughly spaced by 0.06 seconds, on the trajectories in the V-I plane. It appears that the electrochemical transient was faster the lower the resistance.

Zooming in on a specific transient provides further information. In figure 2.4 the second transient, the one to 5.47 Ω, is represented in the V-I plane; the marks on the line represent the sampling points. It can easily be seen that the descent to steady state on the characteristic of the 5.47 Ω resistance was faster than the ascent to steady state on the 82.25 Ω one, when the switch on the resistance board was

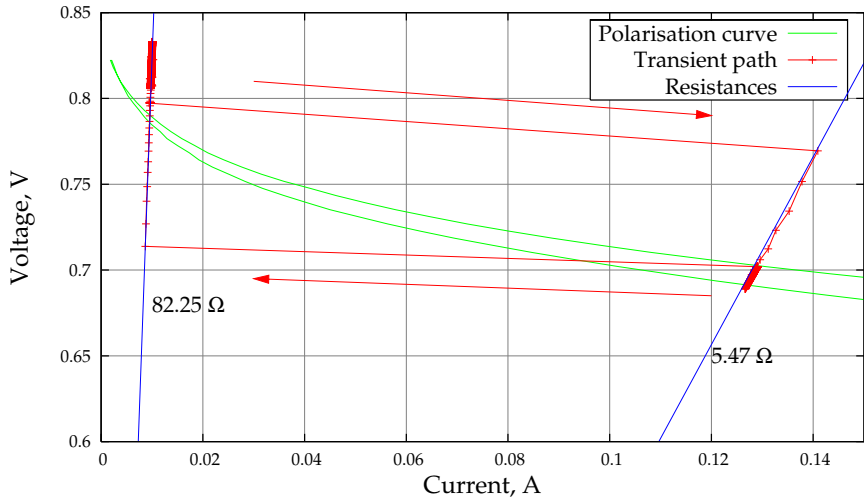

Figure 2.4: Zoom on an experimental transient path for a step change in the external resistance. Some drift is visible around the steady states. The markers are spaced by about 0.06 s.

turned back off.

There is an indication, in other words, that the electrochemical transient can exhibit different time constants depending on both the start and the end point. This behaviour could be related to the phenomenon observed by Johansen [4], where the same proportional controller performed too aggressively in some operating ranges, and too mildly in others.

The values assumed by the voltage are plotted versus time in figure 2.5. The experiments are the same as in figure 2.3. It can be seen that, after a transient in the order of magnitude of one second, a slower transient of generally smaller amplitude appears.

Wang and Wang [13] measured a similar behaviour for a low-temperature PEM fuel cell, which had also been described by Ceraolo et al. [14]. In both cases, the authors noted that slow transients in proton concentration are the cause of these transients. Since protons in the amorphous H_3PO_4 phase are important in PBI fuel cells too [12], the mechanism could be similar in principle. Compared to Wang and Wang's measurements, transients in PBI fuel cells appear to be slower.

It can be seen from figures 2.3 and 2.5 that all the transients to lower values of resistance seem to reach first the lower branch of the polarisation curve, to rise again to the upper one as proton concentration increases. However, the transients back to the initial, larger resistance are much larger than the gap between the branches

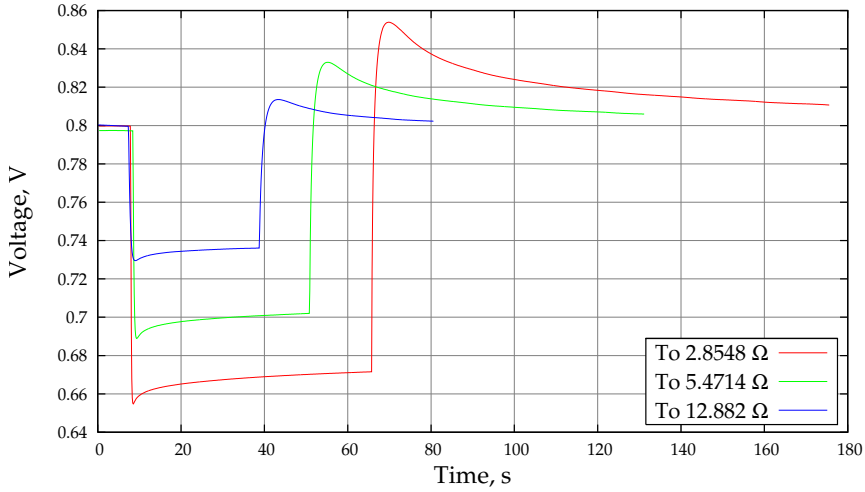

Figure 2.5: Experimental voltage transients after step changes in external resistance, starting from 82.25 Ω and switching back. The data is the same as in figure 2.3.

of the polarisation curve; they show larger overshoots for transients arriving from higher values of current, possibly because of higher concentration of protons. This would seem to strengthen the case for a role of water in the hysteresis of the polarisation curve of figure 2.2, but, on the other hand, these transients are much faster (in the order of 10 s) than the sampling rate of the polarisation curve, which would have had enough time to reach the steady state.

These slower transients are not considered to be an important issue, since in a control perspective, they can easily be controlled by a simple PI feedback controller.

2.3.3 Effect of Flow Disturbances

It was noted that just changing the oxygen flow rate would change the open-circuit voltage significantly, as shown in figure 2.6. It was initially supposed that variations in temperature could be the cause of this behaviour: in the experimental setup sketched in figure 2.1, gases enter the cell at ambient temperature, and could have cooled the cathode to a temperature lower than that measured by the thermocouple. However, subsequent experiments with gas pre-heating showed that the difference was minimal.

The anode turned out to be less sensitive to inlet hydrogen flow. In fact, changing the hydrogen flow would not cause any measurable disturbance to the operating point.

It can be supposed that variations in proton concentration at the cathode are the

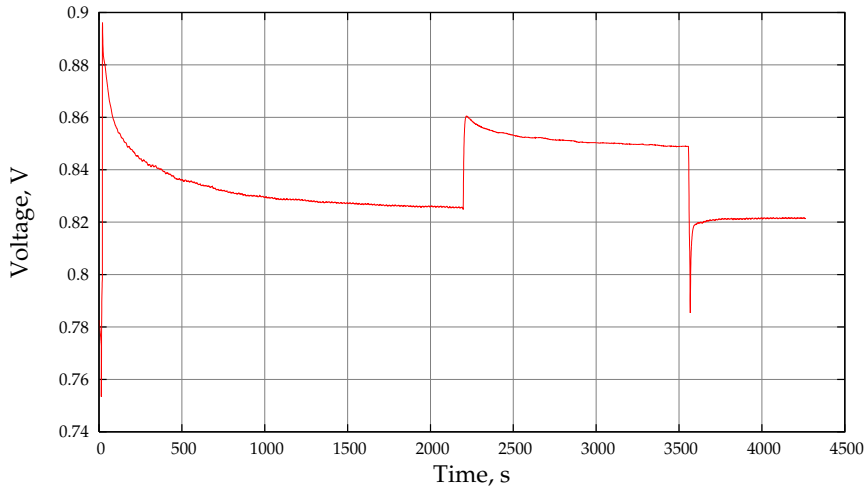

Figure 2.6: Experimental measure of the effect of a step in oxygen flow from 3.7 to 18 cm^3/s at 150 °C on open-circuit voltage. The initial step occurs when oxygen flow is started at the beginning of the experiment. The second step, at about $t = 2200\,s$, occurs when oxygen flow is stepped up; the last step, at about $t = 3600\,s$, when oxygen flow is stepped back down.

cause of these transients too. When oxygen flow is increased, there is an immediate increase in voltage due to higher oxygen partial pressure, and a subsequent decrease due to reduction in proton concentration, caused by the reduced water partial pressure at the reaction site[1]. Conversely, when oxygen flow is reduced, there is a sharp reduction in voltage due to lower oxygen partial pressure, followed by a recovery of proton concentration, faster than the previous transient.

This asymmetry in the dynamics of proton concentration has already been noted by Ceraolo et al. [14].

2.4 Conclusions

A laboratory setup to gather data about the transient behaviour of PBI fuel cells has been presented. Data has been gathered about the steady-state polarisation curve with a very slow scan, and transients have been studied by stepping the value of the resistance connected to the fuel cell: this has highlighted a particular pattern.

[1] Even if we are at open circuit, crossover current is causing some reaction to take place, and some water to be formed.

Some other transients, slower than the ones just mentioned, have also been observed. Whereas their nature is not clear, their importance is argued to be limited for control, as their slow development can easily be compensated for by a feedback loop.

Bibliography

[1] P. Argyropoulos, K. Scott, and W. M. Taama. Dynamic response of the direct methanol fuel cell under variable load conditions. *Journal of Power Sources*, 87:153–161, 2000.

[2] P. Argyropoulos, K. Scott, and W. M. Taama. The effect of operating conditions on the dynamic response of the direct methanol fuel cell. *Electrochimica Acta*, 45:1983–1998, 2000.

[3] K. Sundmacher, T. Schultz, S. Zhou, K. Scott, M. Ginkel, and E. D. Gilles. Dynamics of the direct methanol fuel cell (DMFC): experiments and model-based analysis. *Chemical Engineering Science*, 56:333–341, 2001.

[4] Rune L. Johansen. Fuel cells in vehicles. Master's thesis, Norwegian University of Science and Technology, 2003.

[5] Helge Weydahl, Steffen Møller-Holst, Trygve Burchardt, and Georg Hagen. Dynamic behaviour of an alkaline fuel cell – results from introductory experiments. In *1st European Hydrogen Energy Conference*, Grenoble, September 2003. CP4/123.

[6] Helge Weydahl. *Dynamic behaviour of fuel cells*. PhD thesis, Norwegian University of Science and Technology, Trondheim, August 2006.

[7] Josef Kallo, Jim Kamara, Werner Lehnert, and Rittmar von Helmolt. Cell voltage transients of a gas-fed direct methanol fuel cell. *Journal of Power Sources*, 127:181–186, 2004.

[8] R. Madhusudana Rao and Raghunathan Rengaswamy. Study of dynamic interactions of various phenomena in proton exchange membrane fuel cells (pemfc) using detailed models for multivariable control. In *AIChE Annual Meeting*, 2005.

[9] Jay Benziger, E. Chia, J. F. Moxley, and I.G. Kevrekidis. The dynamic response of PEM fuel cells to changes in load. *Chemical Engineering Science*, 60:1743–1759, 2005.

[10] Qiangu Yan, Hossein Toghiani, and Heath Causey. Steady state and dynamic performance of proton exchange membrane fuel cells (PEMFCs) under various operating conditions and load changes. *Journal of Power Sources*, 161(1):492–502, 2006.

[11] Frode Seland, Torstein Berning, Børre Børresen, and Reidar Tunold. Improving the performance of high-temperature PEM fuel cells based on PBI electrolyte. *Journal of Power Sources*, 160(1):27–36, 2006.

[12] Zhenyu Liu, Jesse S. Wainright, Morton H. Litt, and Robert F. Savinell. Study of the oxygen reduction reaction (ORR) at Pt interfaced with phosphoric acid doped polybenzimidazole at elevated temperature and low relative humidity. *Electrochimica Acta*, 51:3914–3923, 2005.

[13] Yun Wang and Chao-Yang Wang. Transient analysis of polymer electrolyte fuel cells. *Eletrochimica Acta*, 50:1307–1315, 2005.

[14] M. Ceraolo, C. Miulli, and A. Pozio. Modelling static and dynamic behaviour of proton exchange membrane fuel cells on the basis of electro-chemical description. *Journal of Power Sources*, 113:131–144, 2003.

Chapter 3

Electrochemical Modelling

This chapter will present a model of the essential electrochemical dynamics of PBI fuel cells. The electrochemical reaction is the purpose of the cell, and it is necessary to understand it to estimate what control performance we can expect from a fuel-cell stack.

To limit the model to as few parameters as possible, only two dynamic modes will be investigated: the multicomponent diffusion of reactants and the dynamics of the cathodic overvoltage. The model will then be compared to the measurements from the previous chapter with a parameter regression. Finally, a qualitative analysis of the structure of the model will be carried out to determine under what conditions and with what limitations a cell's power output can be modified.

3.1 Literature Review

Most of the vast literature available on fuel cells deals with steady-state conditions. However, interest in dynamic operation of fuel cells has been increasing in recent years.

Many models provided in the literature were intended more for simulation or parameter estimation rather than control analysis, and they usually consider current density as a parameter that can be arbitrarily set by the operator. The reason for this choice is likely that fuel-cell models tend to be simpler and more elegant in this layout, and require a minimum of iterative loops. Furthermore, in a laboratory setup current can indeed be arbitrarily set using a galvanostat.

However, this approach is not satisfactory for process control, because in a real application the current is determined by the characteristics of the fuel cell and of what it is connected to [1]. Many dynamic models described in the literature will

therefore need some revision before they can be useful for control: a proper means of control has to be clearly identified.

Ceraolo et al. [2] developed a dynamic model of a PEM fuel cell that also included the dynamic development of the catalytic overvoltage. Whereas they did not apply their results to control, they produced a model that could easily be modified for control applications by adding an iterative loop on top of it; they also included a model for multicomponent diffusion on the cathode side based on the Stefan-Maxwell equations.

A simple linearised model of a fuel-cell stack was introduced by Yerramalla et al. [3], who used it to simulate transients occurring upon steps in the current passing through the stack. However, as the overvoltage was modelled with the Tafel equation and its transient was neglected, the model might not be reliable for the first part of simulated transients.

Krewer et al. [4] were among the first to recognise and model the feedback loop between a cell stack's voltage and the current through the load. They also included a modelling of charge accumulation in the charge double layer, and tried to reproduce a cell's transient behaviour with linear transfer functions for anode, cathode and membrane of a direct methanol fuel cell.

Pathapati et al. [5] produced a model that calculated the overvoltage as in Amphlett et al. [6], adding the effects of transients in overvoltage and non-steady-state gas flow. A similar model, with a more detailed modelling of the overvoltage, has been proposed by Lemeš et al. [7].

Shan and Choe [8] presented a fuel-cell model that considered the dynamics of temperature, membrane conductivity, proton concentration in the cathode catalyst layer and reactant concentration. The current, however, was considered the input of the system rather than being determined by the external load. The thermal model was especially detailed as it allowed to see the evolution of the temperature profile across a cell without resorting to computational fluid dynamics. Temperature appeared to be fairly uniform with few kelvins of difference between the various components.

3.2 Modelling Principles and Assumptions

The model presented here was originally conceived as a first step in a control analysis and synthesis for PBI-based PEM fuel cells. This model has also been found suitable to describe the transient behaviour of alkaline fuel cells, when operating in conditions where diffusion phenomena are not important [9]; it is expected that, except for diffusion-related issues, most results will hold for Nafion-based fuel cells

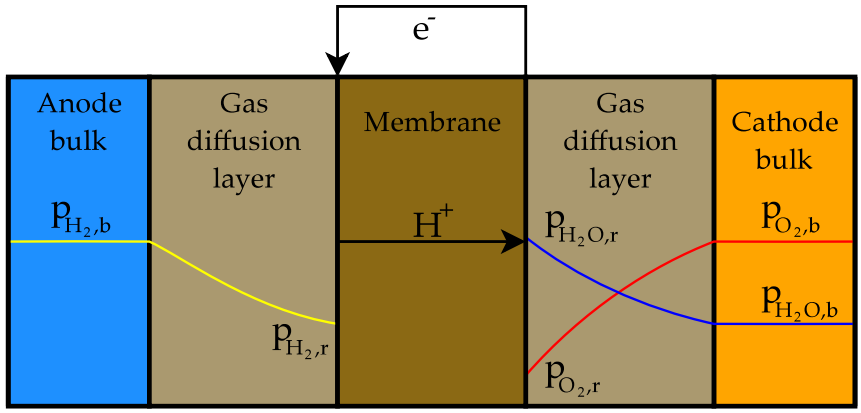

Figure 3.1: Qualitative composition profiles of the reacting species in a PEM fuel cell. Reactions occur at both interfaces between the membrane and the two gas-diffusion layers. Sizes are not to scale.

as well.

For the purposes of process control, high modelling accuracy is usually not necessary: it is more common to produce a model that captures the essential behaviour of the system, and let a feedback loop even out the smaller inconsistencies as they were disturbances. It is more important to predict variations in the frequency range of interest than, for example, slow variations that can be taken care of by a PI controller.

In a generic PBI fuel cell, our electrochemical model will assume there is a constant value for the bulk partial pressure $p_{i,b}$ of a generic species i in the anode and cathode channels. These species are consumed or produced at the interface between the gas-diffusion layer of each electrode and the proton-conducting membrane; water is produced on the cathodic side. Figure 3.1 shows some possible qualitative profiles across the gas diffusion layers.

The partial pressures of species at the reaction sites, $p_{i,r}$, are those that determine the reaction kinetics. These values are however fairly difficult to obtain, as they require to solve a system of partial differential equations (the Stefan-Maxwell and continuity equations): in this case, an approximate algebraic expression would be much more useful.

The model tries to reach an acceptable compromise between the number of parameters and accuracy. Many parameters have been lumped and some phenomena have been neglected or simplified, either in order to save computational time, or

because their dynamics were considered too fast to be of any interest in a controller synthesis.

The following assumptions have been made in the development of this model:

- Diffusion transients reach immediately their steady state, and the concentration profile of each species is linear with distance from reaction site to bulk;
- The anodic overvoltage is neglected;
- Transients are instantaneous also for the concentration of species in amorphous phosphoric acid, which depends on the partial pressures of the species at the reaction sites;
- The inverse (anodic) reaction on the cathode is first-order with respect to water vapour;
- The ohmic loss in the cell is linear with current;
- Cathodic capacitance is constant;
- Crossover current is constant.

3.3 Diffusion

3.3.1 The Stefan-Maxwell Equations

A preliminary analysis was run to establish the influence of diffusion transients on the response of fuel cells, to validate the first assumption of the previous section. Using actual data and formulas as reported by Ceraolo et al. [2], a PBI fuel-cell cathode's reaction surface was modelled, with tortuosity $\tau = 7$, porosity $\varepsilon = 0.4$, distance from reaction site to bulk $L = 0.3\,\text{mm}$, and a temperature of $T = 150\,°\text{C}$. These parameter values are believed to be severe enough to produce a worst-case estimate of the time constant of the diffusion transient. The diffusion process involved water vapour, oxygen and nitrogen, and was modelled with Stefan-Maxwell's equations, in the following form:

$$\frac{\varepsilon}{\tau^2}\frac{\partial p_i}{\partial x} = \sum_{k=1}^{n} \frac{RT}{p\,D_{ik}}\left(p_i N_k - p_k N_i\right) \tag{3.1}$$

These are then coupled with the continuity equations:

$$\frac{\varepsilon}{RT}\frac{\partial p_i}{\partial t} + \frac{\partial N_i}{\partial x} = 0 \tag{3.2}$$

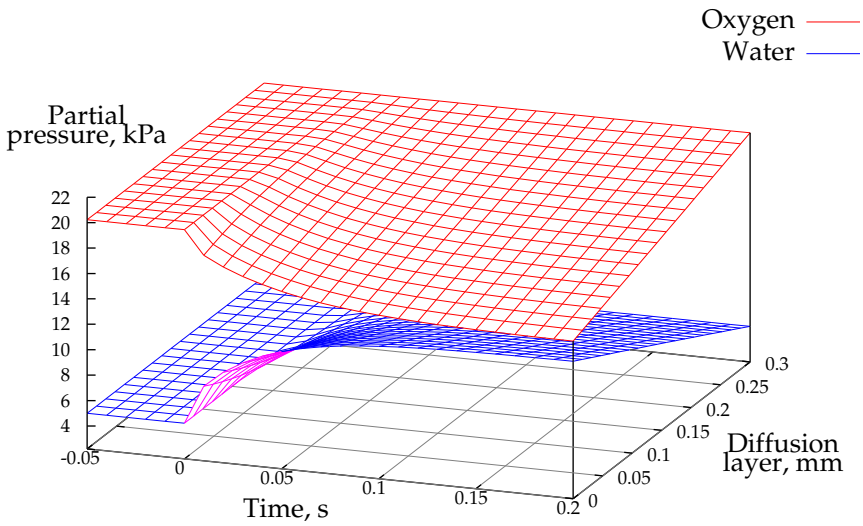

Figure 3.2: Simulated concentration transient on the cathode of a PBI fuel cell; the current steps from 0 to 800 A/m^2 at $t = 0$.

Since diffusion transients are driven by the reactant consumption, they will not in any case be faster than that. If diffusion dynamics is shown to be faster than reactant consumption, assuming instantaneous transients for diffusion is an acceptable approximation.

Furthermore, the diffusion transient can have a noticeable effect on the reaction rate only if the partial pressures at the reaction sites are sufficiently low, that is, when the cell is close to the mass-transport barrier.

The result of diffusion modelling is shown in figure 3.2. This model predicts transients, without overshoots, in the order of 10^{-1} s in case of steps in the reaction rate[1]. As long as the time constants of transients in reaction rate are larger than 10^{-1} s, the diffusion transients may safely be assumed to be instantaneous, but they may be more important when transients in reaction rate are faster.

3.3.2 Simplified Diffusion

To simplify the Stefan-Maxwell equations, we assume that diffusion transients settle immediately, and that all partial-pressure profiles are linear from bulk to reaction site. We can then easily integrate:

[1]We will shortly see that such steps are in fact impossible, since reactant consumption varies continuously as a function of overvoltage.

$$p_i(x) \simeq p_{i,r} + \frac{\partial p_i}{\partial x} x \tag{3.3}$$

Since the Stefan-Maxwell multicomponent diffusion equation (3.1) is valid for any positive distance $x \leqslant L$ from the reaction site, we can evaluate it with the bulk values of partial pressures, $p_{i,b} = p_i(L)$, which are known; furthermore, since we are neglecting the diffusion transient, we can assume that the flows of oxygen, nitrogen and water will be constant in x and directly related to the reaction current density i_r, that is the current corresponding to reactant consumption:

$$N_{O_2} = -\frac{i_r}{4F} \tag{3.4}$$

$$N_{H_2O} = \frac{i_r}{2F} \tag{3.5}$$

$$N_{N_2} = 0 \tag{3.6}$$

Inserting this in the Stefan-Maxwell equation (3.1–3.3), the resulting direct formulæ are:

$$p_{O_2,r} = p_{O_2,b} - \frac{L\tau^2}{\varepsilon} \frac{RT}{4F} \left(\frac{2p_{O_2,b} + p_{H_2O,b}}{p D_{O_2,H_2O}} + \frac{p_{N_2,b}}{p D_{O_2,N_2}} \right) i_r \tag{3.7}$$

$$p_{H_2O,r} = p_{H_2O,b} + \frac{L\tau^2}{\varepsilon} \frac{RT}{4F} \left(\frac{2p_{O_2,b} + p_{H_2O,b}}{p D_{O_2,H_2O}} + 2\frac{p_{N_2,b}}{p D_{H_2O,N_2}} \right) i_r \tag{3.8}$$

It can be seen that, in this approximation, the reaction-site partial pressures vary linearly with reaction-current density. Incidentally, we can obtain an approximate expression of the current i_L at the mass-transport barrier, which occurs when $p_{O_2,r} \to 0$, by rearranging equation 3.7:

$$i_L = p_{O_2,b} \frac{\varepsilon}{L\tau^2} \frac{4F}{RT} \left(\frac{2p_{O_2,b} + p_{H_2O,b}}{p D_{O_2,H_2O}} + \frac{p_{N_2,b}}{p D_{O_2,N_2}} \right)^{-1} \tag{3.9}$$

While this expression is not an exact one, it is very useful as a rough, inexpensive estimate, and as a first guess in more detailed, iterative solution algorithms.

In equations 3.7, 3.8 and 3.9 the components of group $\frac{L\tau^2}{\varepsilon}$ always appear together. It is not possible to estimate L, τ and ε separately in this model, so they will be integrated in a new variable, $\lambda = \frac{L\tau^2}{\varepsilon}$. λ represents the thickness of an equivalent diffusion layer that would result in the same reaction-site partial pressures as in the porous electrode.

a) b)

Figure 3.3: Diffusion layer a) has uniform properties and only one value for λ; a real layer as b) has different properties at different points.

3.3.3 Distributed Layer Thickness

The previous sections implicitly assumed a deterministic value for the effective thickness λ. However, as illustrated in figure 3.3, the actual picture is more complex. The points on the electrode area have different properties, resulting in different values for λ. As the electrochemical system is a nonlinear function of reaction-site partial pressures (and, by equations 3.7 and 3.8, of λ), the shape of the distribution may influence the overall polarisation curve.

To test this possibility, the model will implement the possibility of using a distributed equivalent layer thickness, Λ, which will follow a lognormal distribution.

The lognormal distribution's probability density function of a random variable X is usually reported as:

$$\rho(x) = \begin{cases} \dfrac{1}{\sqrt{2\pi}\sigma_Y\, x}\, e^{-\frac{[\ln(x)-\mu_Y]}{2\,\sigma_Y^2}} & \text{if } x \geqslant 0; \\ 0 & \text{if } x < 0. \end{cases} \tag{3.10}$$

The mean μ_Y and the variance σ_Y^2 used in equation 3.10 are not the ones of random variable X, but of the corresponding normal distribution $Y = \ln(X)$. The mean μ and variance σ^2 of X are instead given by:

$$\mu = e^{\mu_Y + \frac{\sigma_Y^2}{2}} \tag{3.11}$$

$$\sigma^2 = e^{2\,\mu_Y + \sigma_Y^2} \left(e^{\sigma_Y^2} - 1\right) \tag{3.12}$$

Some lognormal distributions are shown in figure 3.4.It can be noticed how the mean does not in general correspond to the maximum in the density function.

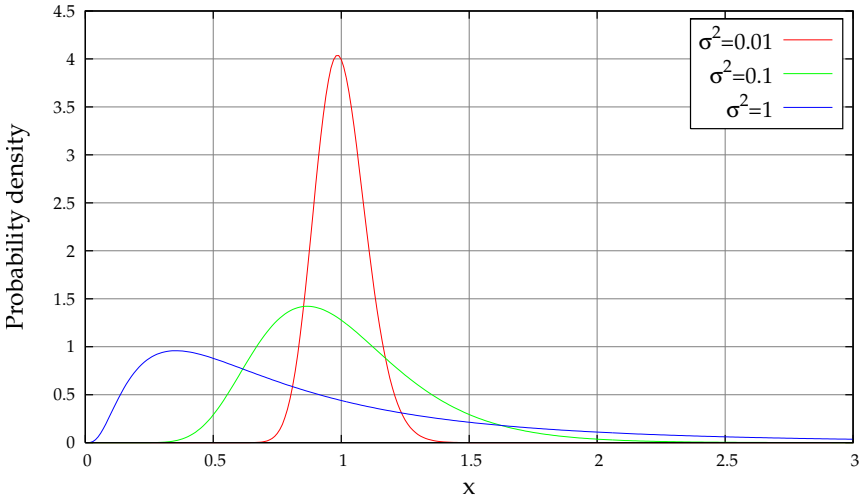

Figure 3.4: Some examples of lognormal distributions. All these have a mean value of 1.

The lognormal distribution, compared to the more common normal distribution, offers the significant advantage of being exactly zero for all $\lambda \leqslant 0$, which represent physically meaningless values.

Given a function that depends on the distributed variable Λ, it is possible to obtain its overall value for the whole range of λ values with a weighed integration. For ease of notation, we will indicate this operation with $\mathcal{I}[\,]$:

$$\mathcal{I}[f(\Lambda)] = \int_0^\infty f(\lambda)\rho(\lambda)\,d\lambda \tag{3.13}$$

3.4 Calculating the Cell Voltage

The steady-state cell voltage is calculated subtracting catalytic and resistive losses from the reversible electrochemical potential:

$$V = E^{rev} - r_{MEA}\,(i + i_c) - \eta \tag{3.14}$$

The reversible cell potential E^{rev} can be found from well-known thermodynamic data:

$$E^{rev} = -\frac{\Delta g_f^0}{n\,F} + \frac{R\,T}{n\,F}\ln\left(\frac{a_{O_2}\,a_{H_2}}{a_{H_2O}}\right) \tag{3.15}$$

Δg_f^0 is calculated at standard conditions, and the activities are those at the reaction sites. In the case of a distributed Λ, since reaction-site partial pressures and activities depend on the specific value of λ through equations 3.7 and 3.8, in is necessary to integrate the last term:

$$E^{rev} = -\frac{\Delta g_f^0}{n\,F} + \frac{R\,T}{n\,F}\left\{\mathcal{I}\left[\ln(a_{O_2})\right] + \mathcal{I}\left[\ln(a_{H_2})\right] - \mathcal{I}\left[\ln(a_{H_2O})\right]\right\} \tag{3.16}$$

E^{rev} will in this case be a function of i_r and Λ. Note that $\mathcal{I}$ may refer, depending on which term is integrated, to the thickness distribution of the cathode or the anode.

The crossover current i_c lumps together the parasitic losses, such as electronic conductivity in the membrane. It is generally small, and is important only at low values of current, where it prevents the cell from reaching reversible voltage at open circuit. Its value is usually assumed constant in the literature.

The ohmic loss is immediately found as the product of the membrane-electrode assembly's specific resistance and the sum of circuit and crossover current density, $r_{MEA}\,(i + i_c)$.

The model is able to simulate overvoltage effects on the anode, but these are of minor importance in normal operation. They will be therefore neglected, and only the cathode will be considered: unless differently specified, it will be understood from now on that all electrochemical terms refer to the cathode.

At steady state, the reaction current density i_r is equal to the circuit current density i plus the crossover current density i_c; i_r represents the reaction rate resulting from the Butler-Volmer equation, i the actual current flowing in the external circuit divided by the cell's area, and i_c the internal losses such as permeation of reactants through the membrane or electronic conductivity of the membrane.

Liu et al. [10] have studied the oxygen reduction reaction at the cathode of a PBI fuel cell. Their results indicate that the rate-determining step is first-order with respect to oxygen and protons:

$$O_2 + H^+ + e^- \longrightarrow O_2H \tag{3.17}$$

The remaining steps from O_2H to H_2O are faster, and can be assumed to be instantaneous. The oxygen term is the oxygen present in amorphous H_3PO_4, and the concentration of protons can be promoted by water:

$$H_3PO_4 + H_2O \rightleftharpoons H_2PO_4^- + H_3O^+ \tag{3.18}$$

In the data range of interest, the data provided by Liu et al. seems to indicate that the concentration of H^+ is approximately proportional to the partial pressure of water vapour.

There are no equivalent studies for the inverse reaction of water oxidation, so it will be simply assumed to be first-order with respect to water.

$$\tfrac{1}{2}H_2O \longrightarrow H^+ + e^- + \tfrac{1}{4}O_2 \tag{3.19}$$

Assuming that the activity of oxygen in the amorphous H_3PO_4 phase is proportional to the partial pressure of oxygen at the reaction site (with no transient modelled), the following expression results for the exchange current density [11]:

$$i_0 = n\,F\,k \left(\frac{p_{O_2}}{p_0}\right)^{\alpha} \left(\frac{p_{H_2O}}{p_0}\right)^{\frac{1+\alpha}{2}} \tag{3.20}$$

where n is equal to 1 and p_0 is the standard pressure (101 325 Pa). Finally, Liu et al. also provided an estimate for the symmetry factor α, in the range 0.42–0.44; $\alpha = 0.43$ will be assumed.

Reaction current density i_r, representing the current corresponding to the reaction rate per unit area, can then be calculated for a given activation overvoltage η, which represents the voltage loss associated to reaction kinetics, according to the Butler-Volmer equation [11]:

$$i_r = i_0 \left(e^{\alpha \frac{n\,F}{R\,T}\eta} - e^{-(1-\alpha)\frac{n\,F}{R\,T}\eta}\right) \tag{3.21}$$

If we are considering a distributed Λ, we would then obtain the value of i_r by the following relationship:

$$i_r(\eta, \Lambda) = \mathcal{I}[i_r(\eta, \lambda)] \tag{3.22}$$

Since equation 3.21, which binds η and the reaction current density i_r, cannot be explicitly inverted directly as $\eta = f(i_r)$, an iterative algorithm is necessary. However, if we assume that the second exponential term in equation 3.21 is much smaller than the first one, we obtain the Tafel equation:

$$\begin{aligned} \eta &= \frac{R\,T}{\alpha\,n\,F} \ln\left(\frac{i_r}{i_0}\right) && \text{for } i_r > i_0 \\ \eta &= 0 && \text{for } i_r \in [0, i_0] \end{aligned} \tag{3.23}$$

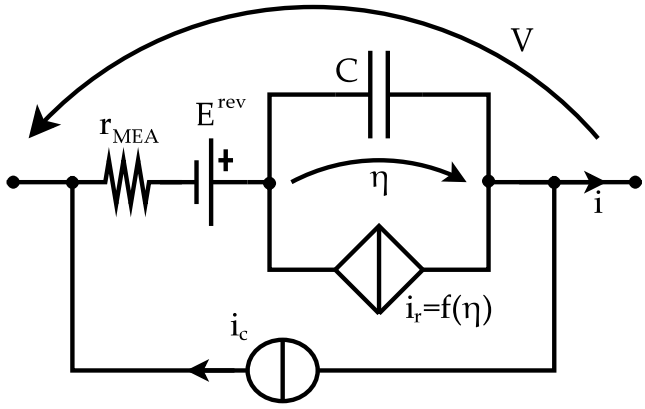

Figure 3.5: Diagram of the fuel-cell model.

The Tafel equation is not very accurate for low values of η and is not invertible for $i_r < i_0$, but is a very useful, inexpensive estimate in most situations.

3.5 Dynamics

Transients occur when $i_r \neq i + i_0$, because this indicates that there is a charge imbalance that will change the value of overvoltage η. The dynamic equation describing the transient is as follows [2]:

$$\dot{\eta} = \frac{i + i_c - i_r}{C} \tag{3.24}$$

This is the only differential equation that we will consider in order to simulate the transient of the fuel cell. As already mentioned, all diffusion transients will be neglected, and any capacitance or inductance in any part of the load is neglected as well. Capacitance C is assumed to be constant, but some authors reported it to be variable [12]. C represents the sum of an electrostatic double layer capacitance, a pseudocapacitance due to charge stored by adsorbed and intermediate products at the surface, and the charge stored in the diffusion layers [13].

The external load applied to the model is allowed to vary with time, and is described by a function of the form $I = f(V, t)$. It has been chosen to use this form instead of $V = g(I, t)$ to allow the implementation of loads such as MOSFETs, where there can be infinite values of I for one value of V.

Figure 3.5 represents the model graphically. There, one can see the internal resistance r_{MEA}, the reversible potential E^{rev}, the capacitor C and its overvoltage η. The

Overvoltage differential equation	$\dot{\eta} = \frac{i + i_c - i_r}{C}$	(3.24)
Butler-Volmer equation	$i_r = i_0 \left(e^{\alpha \frac{nF}{RT} \eta} - e^{-(1-\alpha) \frac{nF}{RT} \eta} \right)$	(3.21)
Exchange current density	$i_0 = n F k \left(\frac{p_{O_2,r}}{p_0} \right)^{\alpha} \left(\frac{p_{H_2O,r}}{p_0} \right)^{\frac{1+\alpha}{2}}$	(3.20)
Oxygen diffusion	$p_{O_2,r} = f(i_r, p_{i,b}, \Lambda, T)$	(3.7)
Water diffusion	$p_{H_2O,r} = g(i_r, p_{i,b}, \Lambda, T)$	(3.8)

Table 3.1: Summary of the main equations used in the model.

bipole in parallel with the capacitor is a nonlinear voltage-controlled current generator, which represents the Butler-Volmer law imposing a current i_r as a function of η (and many other parameters, as per equation 3.21). This bipole is often modelled as a nonlinear resistance [5], or a linearised value in an area of interest. Incidentally, ideal generator E^{rev} and resistance r_{MEA} can be viewed as a Thevenin equivalent circuit.

The actual integration of equation 3.24 is not very simple, since i_r is a function of many parameters (including η itself) through the Butler-Volmer equation (3.21). Furthermore, the exchange current density i_0 in that equation depends on the reaction-site concentrations of the reactants (equation 3.20), which, in turn, depend on their consumption rate, proportional to i_r. An iterative loop, consisting of equations 3.7, 3.8, 3.20 and 3.21, is therefore necessary to calculate i_r at all integration steps, and this is the major computational cost of the simulation. This phenomenon could be approximated assuming a constant i_0, but a separate, empirical term should then be introduced in equation 3.14 to model mass-transport losses. The complete set of equations to solve is summarised in table 3.1.

3.6 Time Constants

Given the state x of a dynamic system, a time constant is the factor τ in the following differential equation:

$$\tau \dot{x} = -x \tag{3.25}$$

Forcing terms were neglected in this equation for sake of simplicity. We will now show how to obtain an analytic relationship for the time constant of the elec-

trochemical transient of fuel cells.

The external characteristic is assumed to be a generally nonlinear, purely resistive load of the type $V = \Psi(i)$. The reversible voltage E^{rev}, the cell's internal resistance r_{MEA} and the crossover current i_c are assumed to be constant. The time derivative of the cell's voltage is then expressed as:

$$\frac{dV}{dt} = \frac{d}{dt}\left[E^{rev} - \eta - r_{MEA}\,(i + i_c)\right] = -\frac{d}{dt}(\eta + r_{MEA}\,i) \tag{3.26}$$

Since the operating point has to be on the load's characteristic as well as on the cell's instantaneous one, we can write:

$$\frac{dV}{dt} = \frac{d\Psi}{dt} = \frac{d\Psi}{di}(i)\,\frac{di}{dt} \tag{3.27}$$

Inserting in equation 3.26 and rearranging:

$$\frac{di}{dt} = -\left[r_{MEA} + \frac{d\Psi}{di}(i)\right]^{-1}\frac{d\eta}{dt} = -\left[r_{MEA} + \frac{d\Psi}{di}(i)\right]^{-1}\frac{i + i_c - i_r}{C} \tag{3.28}$$

The overvoltage's time derivative is:

$$\frac{d\eta}{dt} = \frac{i + i_c - i_r}{C} = \frac{d\eta}{di_r}(i_r)\,\frac{di_r}{dt} \tag{3.29}$$

Rearranging:

$$\frac{di_r}{dt} = \left[\frac{d\eta}{di_r}(i_r)\right]^{-1}\frac{i + i_c - i_r}{C} \tag{3.30}$$

Subtracting equation 3.30 from equation 3.28, we obtain the following relationship:

$$\frac{d(i + i_c - i_r)}{dt} = -\underbrace{\frac{1}{C}\left\{\left[r_{MEA} + \frac{d\Psi}{di}(i)\right]^{-1} + \left[\frac{d\eta}{di_r}(i_r)\right]^{-1}\right\}}_{1/\tau}(i + i_c - i_r) \tag{3.31}$$

Assuming that C and r_{MEA} are constant, that functions $\Psi(i)$ and $\eta(i_r, \ldots)$ are given, the time "constant" τ depends essentially on i and i_r:

$$\tau(i, i_r) = \frac{C}{\left[r_{MEA} + \frac{d\Psi}{di}(i)\right]^{-1} + \left[\frac{d\eta}{di_r}(i_r)\right]^{-1}} \tag{3.32}$$

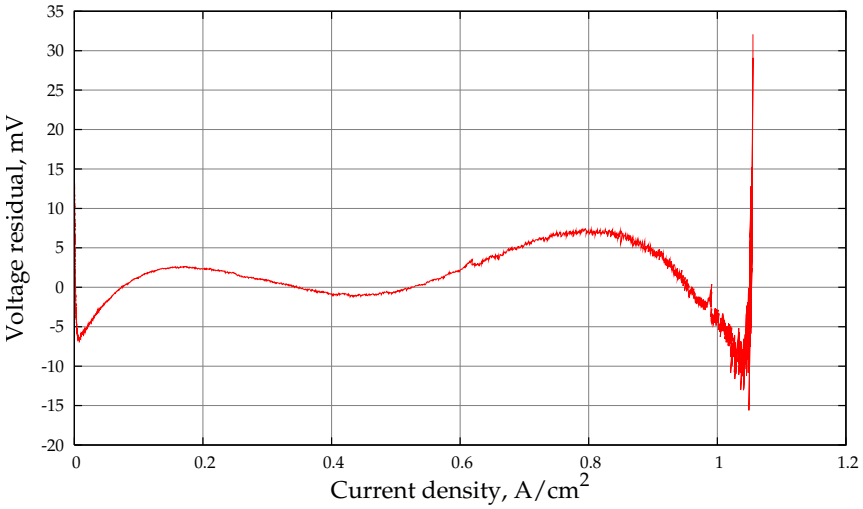

Figure 3.6: Plot of residuals (sample minus model values) for the model applied to the upper branch of the polarisation curve shown in figure 2.2.

The reasons for using $i + i_c - i_r$ instead of the more natural η are that it is possible to find expression 3.31 explicitly, without solving numerically the Butler-Volmer equation (3.21), and that it is not necessary to add a forcing term to account for external effects, since they are already included through Ψ; furthermore, the term $i + i_c - i_r$ always returns to zero at the end of a transient, since it is its driving force.

3.7 Parameter Estimation and Simulation

A parameter regression was carried out to verify whether and how well the proposed model fitted the results. It was noticed that whereas parameter estimation seems difficult because of the large hysteresis of the polarisation curve in figure 2.2, the model fits very well the upper branch of the curve. However, the lower branch does not qualitatively fit, even with different values. This parameter regression assumes a non-distributed layer thickness.

The residuals are plotted in figure 3.6, where it can be seen that the model predicts the cell's voltage in the upper branch with an approximation of ± 10 mV until it reaches the mass-transport limit. The results of the parameter regression are shown in table 3.2.

There is significant correlation between internal resistance r_{MEA} and reaction

	Estimate	Standard deviation	Units	Correlation matrix			
k	115.7	55.9	$\mu mol/m^2\,s$	1	−0.590	0.672	0.847
λ	25.82	0.349	mm	−0.590	1	−0.740	−0.648
i_c	33.63	93.94	A/m^2	0.672	−0.740	1	0.518
r_{MEA}	26.07	5.96	$\mu\Omega\,m^2$	0.847	−0.648	0.518	1

Table 3.2: The results of the parameter regression for parameters k, λ, i_c and r_{MEA} with the data of the upper branch of the polarisation curve presented in figure 2.2.

constant k, since in most experimental points the effect of increased resistance is similar to that of a reduced reaction constant. Similarly, there is high correlation between crossover current density i_c and the effective thickness of the diffusion layer λ: since information about λ is gathered mostly at data points close to the mass-transport barrier, an increase in i_c will have an effect similar to a reduction in λ, because it will move the barrier to the left in the plot.

To reduce these correlations, one may gather data points from conditions where the effects of these parameters are going to vary independently, such as different values of temperature or gas composition.

As noted, the model does not fit the lower branch of the polarisation curve. It is possible that the lower branch follows different kinetics, or that other factors, such as catalyst deactivation and transients in proton concentration, interfered in the measurement and caused the hysteresis observable in the scan of figure 2.2.

It was not possible to perform a proper parameter estimation for the cathodic capacitance, as the slower secondary transients shown in figure 2.5 are not well understood, and would have interfered in the regression procedure. Furthermore, the exact time of switching could not be logged in the measurements with sufficient precision. However, a value in the range of 1 to $2\,kF/m^2$ seems to reproduce the observed behaviour with acceptable approximation.

It was found that using a lognormally distributed Λ for the cathode would not result in an improved fit. The distribution's standard deviation is very highly correlated with λ, and the negligible increase in accuracy is considered not to be worth the large overhead in terms of computational effort.

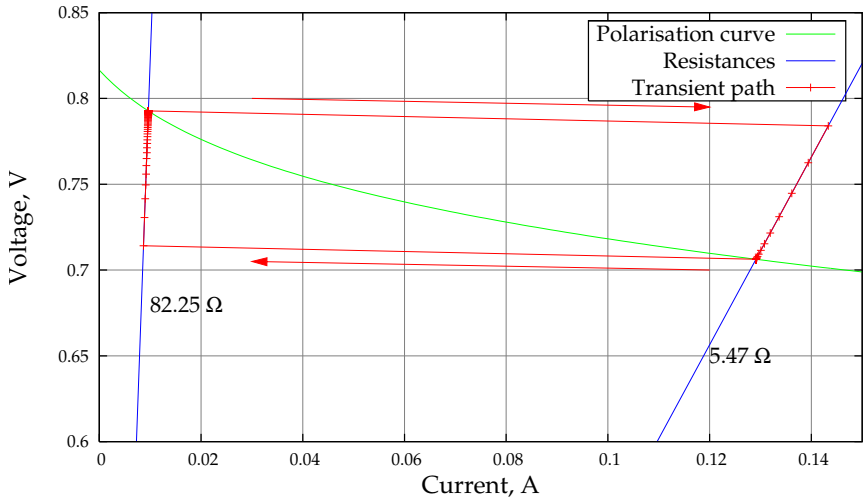

Figure 3.7: Simulated transient trying to replicate the experiment in figure 2.4. The value assumed for the capacitance is $1500\,\mathrm{F/m^2}$. The markers are spaced by 0.06 s, except those at switching points that are spaced 1 µs.

3.8 Simulation

With the parameters given in table 3.2, a simulation has been carried out to replicate the experimental measurements of figure 2.4; its results are presented in figure 3.7.

The model allows also to simulate other types of loads, such as MOSFETs. In figure 3.8, the transient associated to a IRF1404 power MOSFET by International Rectifier, Inc. is simulated.

3.9 Impedance Measurements

A common method to extract information from electrochemical systems is measuring the electrochemical impedance [14]. With this technique, a fuel cell is initially kept at a constant base voltage or current, and then small sinusoidal perturbations of a certain frequency are added. The amplitude ratio and phase shift between voltage and current oscillations provide a complex function of oscillation frequency, the impedance $Z(\omega) = R(\omega) + iX(\omega)$, whose real part is termed resistance and the imaginary part reactance. Impedance can also be seen as a transfer function between current and voltage.

The resistance and reactance associated to the model pictured in figure 3.5 are fortunately fairly easy to calculate. For ease of notation, we denote $R_c = \eta/I$:

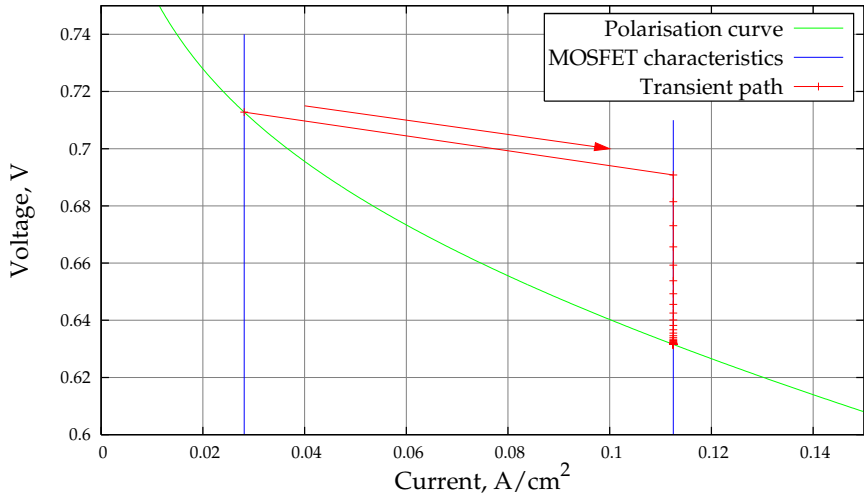

Figure 3.8: The simulated transient resulting from having changed the gate voltage of a MOSFET from 3.05 to 3.1 volts, when this MOSFET is operating as the load of a PBI fuel cell at 150 °C. The markers are spaced by 0.01 s, except for the switching instant when there is a spacing of 1 µs.

$$R(\omega) = R_{MEA} + \frac{R_c}{1 + (\omega\, R_c\, C)^2} \tag{3.33}$$

$$-X(\omega) = \frac{\omega\, R_c^2\, C}{1 + (\omega\, R_c\, C)^2} \tag{3.34}$$

These equations do not account for anodic effects and diffusion phenomena; the latter cannot be modelled explicitly because of the complexity of the Stefan-Maxwell equations. However, in experimental data, a Warburg impedance due to diffusion may appear at low values of frequency.

We can extract information about R_{MEA} and R_c from an impedance spectroscopy by taking the limits to zero and infinity of the expression given for the cell's impedance:

$$\lim_{\omega \to \infty} Z(\omega) = R_{MEA} \tag{3.35}$$

$$\lim_{\omega \to 0} Z(\omega) = R_{MEA} + R_c \tag{3.36}$$

Calculating the values of impedance for various values of ω, one can plot the impedance values in the Nyquist plane, as in figure 3.9. The semicircle is a common

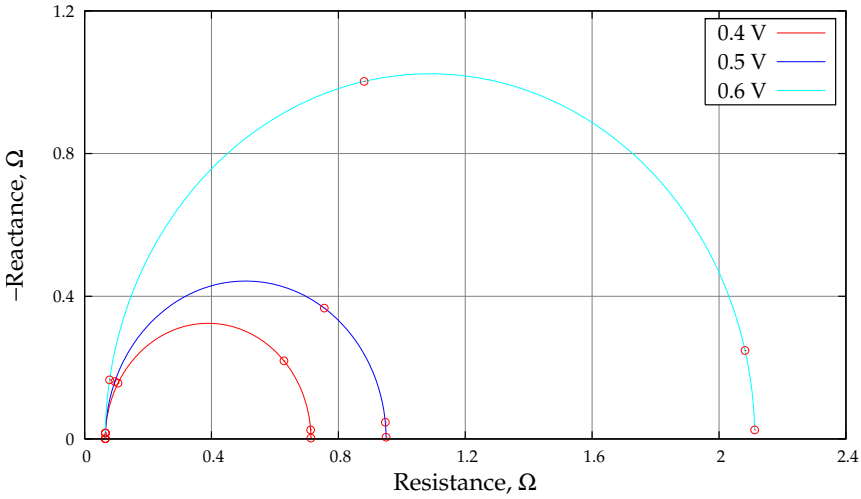

Figure 3.9: Plot of the impedance of a fuel cell at various values of cell voltage for frequencies from 10^{-2} to 10^{3} rad/s. The lowest values of frequency are on the right, and each marker on the curves indicates a ten-fold increase in frequency. Model parameters are as in table 3.2, cell area is $4\,\mathrm{cm}^2$.

result for fuel cells: another (usually much smaller) semicircle may also appear in experimental data, representing the anode.

Impedance measurements can be a good source of information about the capacitance C of the model: it can be demonstrated that, at the point of minimum reactance (the summit of the semicircle in figure 3.9), the following relation holds:

$$\omega_{\text{summit}} = \frac{1}{R_c\, C} \tag{3.37}$$

The diameter of the semicircle is R_c; as overvoltage η is not linear with current I, the semicircles will have different diameters for different operating conditions. At open circuit, $R_c \to \infty$ since $I = 0$ and $\eta > 0$ (because of the small crossover current): the circle will degenerate into a vertical line passing by $R = R_{\text{MEA}}$.

Since the model can easily calculate the impedance of a fuel cell, it may be possible to perform a parameter estimation for the model's capacitance C at frequencies where the slower transients noticed in figure 2.5 are not important and do not interfere with the measurements.

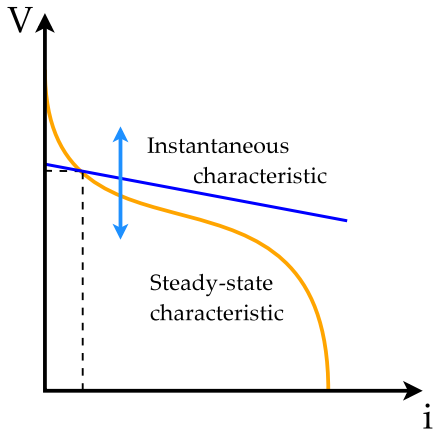

Figure 3.10: The steady-state polarisation curve and the instantaneous characteristic on a V-i plane. The instantaneous characteristic moves up or down depending on the value of overvoltage η.

3.10 Instantaneous Characteristics

Polarisation curves represent steady-state values[2], and do not contain information about the way fuel cells behave during transients. To include this information in the same plot, we define the *instantaneous characteristic* to be the locus of all points in the V-i plane that can be reached instantaneously by the fuel cell. To define it, it is important to examine which terms of the polarisation curve are going to change in a transient, and how so.

The instantaneous characteristic comes from equation 3.14, where the terms V and i can change stepwise, whereas η evolves dynamically and continuously in time according to equation 3.24. Reaction current density i_r, which represents the consumption of reactants, is a continuous, strictly increasing function of η, according to the Butler-Volmer equation [16]: i_r is therefore as continuous in time as η is. To any value of η corresponds one and one only value of i_r, so the state of the fuel cell may be described by i_r just as well as by η: it is possible to express each one as a function of the other[3]. The reversible voltage E^{rev} will also not have a discontinuity

[2]At least ideally so. The slow secondary transients that often appear in laboratory tests (such as those described by Benziger et al. [15]) are often hidden behind an averaging of the obtained values in much of the available literature.

[3]On the other hand, the Butler-Volmer equation, expressing $i_r = f(\eta)$, cannot be solved explicitly for η, and requires an iterative loop. The Tafel equation (3.23) is a very good approximation of $\eta = f(i_r)$ for sufficiently large values of i_r [17].

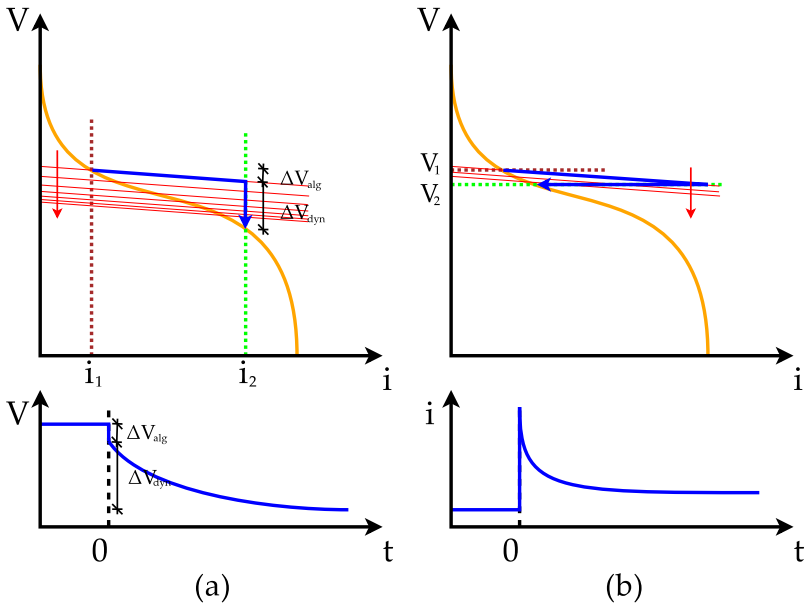

Figure 3.11: Transients in the phase plane and in time when stepping (a) the cell current or (b) the cell voltage using a galvanostat or a potentiostat, respectively.

at step time, since it depends on i_r.

The equation for the cell voltage can be rewritten, highlighting the dynamic and the algebraic parts:

$$V(t,i) = \underbrace{E^{rev} - \eta}_{V_{dyn}(t)} \underbrace{- r_{MEA} \cdot (i + i_c)}_{V_{alg}(i)} \tag{3.38}$$

If a stepwise change occurs in i at time t_0, V_{dyn} will remain continuous, and it will have a single value at that time. V_{alg} will instead change instantaneously with i, and will present a discontinuity.

The instantaneous characteristic described by equation 3.38 can be seen as a line in the V-i plane, rising or descending according to the value of $V_{dyn}(t)$. It will be a straight line if r_{MEA} is constant, as shown in figure 3.10.

3.10.1 Transient Behaviour

We can now turn our attention to how specific transients develop. The values of voltage and current will be determined by the intersection between the instantaneous characteristics of the cell and the characteristic of the load. If the intersection

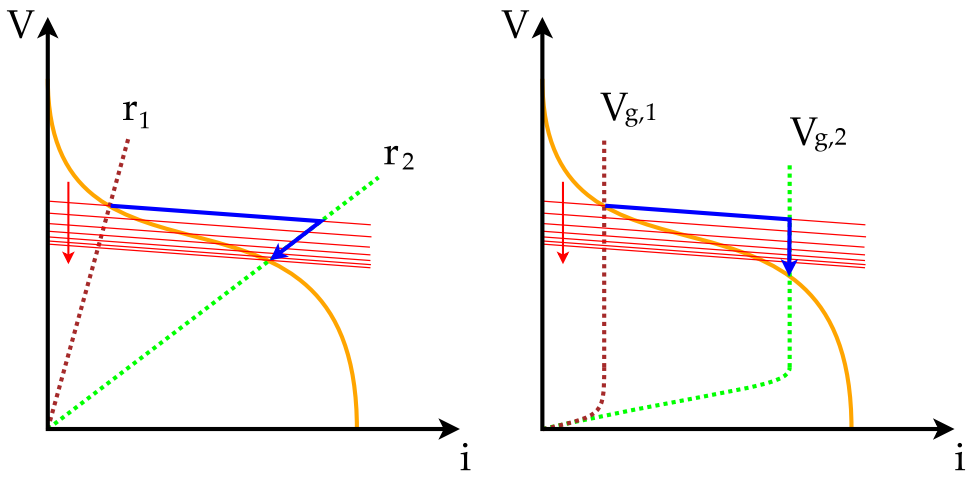

Figure 3.12: Transients in the phase plane obtained by changing the external circuit's characteristic, on the left with a resistance (stepping from r_1 to r_2) connected to the fuel cell, and on the right with a MOSFET whose gate voltage is stepped from $V_{g,1}$ to $V_{g,2}$.

point is not on the steady-state polarisation curve, the cell's instantaneous characteristic will rise or descend until the operating point will be brought to the intersection between the load characteristic and the polarisation curve.

In general, the load may be represented by an instantaneous characteristic as well, but for ease of treatment we consider only loads with constant characteristics.

In figures 3.11 and 3.12, a few simple transients have been sketched. They all start from a steady-state point on the polarisation curve, and illustrate the path of the operating point to reach the new steady state. All transients can be divided in two parts:

1. After the step in external load has taken place, the operating point instantaneously moves to the intersection of the current instantaneous characteristic and the new load;

2. Remaining on the external load's characteristic, the operating point follows the movement of the instantaneous characteristic, until it settles on the intersection between the external load and the polarisation curve.

Whereas the plots in figure 3.11 imply the presence of a current or voltage generator, those in figure 3.12 assume loads that can be changed with little or no external

power supply. A resistance step may be performed with a simple switch or using a rheostat; a step in the gate voltage of a MOSFET[4] will require a voltage source, but this source will have to provide only a negligible amount of power.

3.10.2 Graphical Representation of Time Constants

As previously stated, the catalytic overvoltage varies according to the differential equation:

$$\frac{d\eta}{dt} = \frac{i + i_c - i_r}{C} = \frac{i - (i_r - i_c)}{C} \tag{3.39}$$

Since the level of the instantaneous characteristic is determined by the value of η, the right-hand side in equation 3.39 represents also the "speed" at which the instantaneous characteristics moves vertically on the plot. It is relatively easy to find i and $i_r - i_c$ graphically: the circuit current, i, is at the intersection of the instantaneous characteristic with the external load; the reaction current minus the crossover current, $i_r - i_c$, is at the intersection of the instantaneous characteristic with the polarisation curve.

The latter claim can be demonstrated as follows: the polarisation curve represents the steady-state points, and the instantaneous-characteristic represents all points with the same η and i_r: their intersection is the steady state with the same reaction current i_r of the transient operating point. Since at steady state, by equation 3.24, $i_r - i_c = i$, the projection of this intersection on the i axis is $i_r - i_c$, as illustrated in figure 3.13.

An interesting side effect is that some transients may have different time constants depending on how "close" to the polarisation curve their trajectory is. If a transient trajectory consists of points "close" to the polarisation curve[5], the driving force of equation 3.39 (that is $i - (i_r - i_c)$) is small, and the transient will be slower. This has been verified experimentally [19], and simulation indicates that times in the order of 10 s are common to reach steady state in open circuit. Settling times for most transients are in the range between 0.1 and 10 s.

[4]For a process engineer, MOSFETs can be thought as valves that allow more current through them when their gate voltage is increased. For a detailed treatise of MOSFETs, see e.g. Mohan et al. [18].

[5]More rigorously: points lying on an instantaneous characteristic whose intersection with the polarisation curve is close, with distance being measured along the i axis.

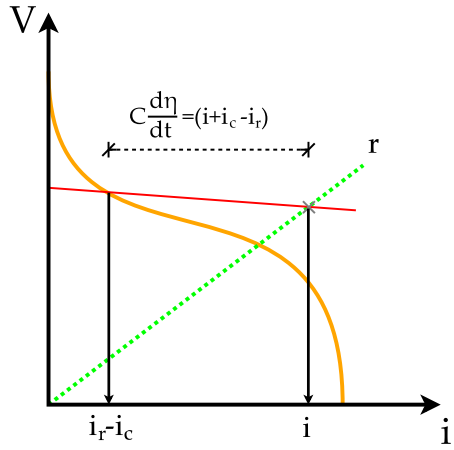

Figure 3.13: The distance between the intersections of the instantaneous characteristic with the external load and with the polarisation curve represents the driving force of the transient.

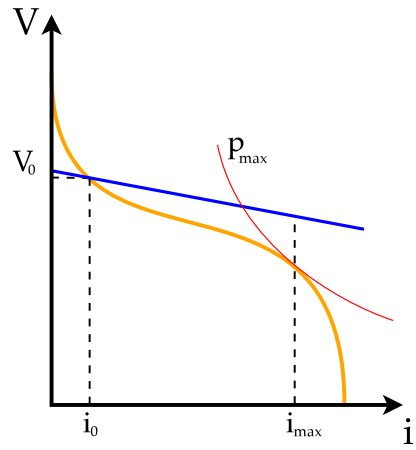

Figure 3.14: At current i_{max}, where the steady-state power output is maximum, the instantaneous characteristic from point (i_0,V_0) has a higher voltage than the polarisation curve.

3.11 Perfect Control of the Electrochemical Transient

An important result can be obtained observing the instantaneous characteristics in the previous figures. We see clearly that they pass by the current corresponding to the maximum power output with a higher voltage than the polarisation curve, as exemplified in figure 3.14. It is an immediate observation that this means that we can, at least in theory, step the power output of the fuel cell even beyond the maximum nominal value. We shall now seek to properly formalise this finding.

We define p_{max} to be the maximum power output of a fuel cell, and i_{max} to be its corresponding current on the steady-state polarisation curve.

Theorem 3.11.1 (Perfect control of the electrochemical transient)**.** *Given a fuel cell having its steady-state voltage expressed by* $V(i) = E^{rev} - \eta(i_r) - r_{MEA}(i)\,(i + i_c)$*, with overvoltage* $\eta(i_r)$ *strictly increasing with* i_r *and internal resistance* $r_{MEA}(i)$ *continuous in* i*, it is always possible to instantaneously step the power output to any value between zero and its maximum steady-state value from any operating point lying on an instantaneous characteristic that intersects the polarisation curve at some* $i \in [0, i_{max}]$.

Proof. Given any $i_0 \in [0, i_{max}]$, we can identify the corresponding instantaneous characteristic $V(i) = E^{rev} - \eta(i_0 + i_c) - r_{MEA}(i)\,(i + i_c)$. Since $\eta(i_r)$ is strictly increasing

with i_r, $\eta(i_{max} + i_c) \geqslant \eta(i_0 + i_c)$.

Subtracting the steady-state characteristic from the instantaneous one at $i = i_{max}$, we obtain $-\eta(i_0 + i_c) + \eta(i_{max} + i_c) \geqslant 0$, meaning that the instantaneous characteristic will have a higher voltage at $i = i_{max}$, and thereby a larger power output than the steady-state characteristic.

Power along the instantaneous characteristic varies continuously, according to the formula $p(i) = V(i)\, i$, because $r_{MEA}(i)$ is also assumed continuous. It is trivial that power output can be set to zero by choosing $i = 0$. For the intermediate-value property, $\exists\, i : p(i) = p, \forall p \in [0, p_{max}]$. □

This theorem guarantees, therefore, that there is a way to immediately change to any value of power output in the complete power range of the fuel cell, from zero to maximum, under very general conditions. This means there is no inherent limitation to how fast control we can achieve in the electrochemical domain, even though practical issues such as measurement time and computation time will eventually pose a limit.

This has also other implications: if incorrectly controlled, a fuel cell might exhibit large spikes in power output, which may damage equipment connected to it. This might be especially important in microelectronics appliances.

3.11.1 Implicit Limitations

Theorem 3.11.1 delivers an important result, but makes some implicit assumptions. The assumption about the form of the function describing the polarisation curve is especially important, since the curve is expected to be only a function of the circuit and reaction currents: other factors such as temperature, catalyst poisoning, reactant concentration are left out.

Therefore, *the theorem is valid only in the context of a certain set of states* that define the polarisation curve: we are only guaranteed that we can instantly reach the maximum power output for those conditions of temperature, composition, and other variables defining the cell's state. This may be less than the nominal power output that the fuel cell is supposed to deliver in design conditions. In such a case, other control variables may be used to modify these states, and might pose some performance limits: for instance, a temperature increase cannot occur stepwise.

3.12 Conclusions

A dynamic model for fuel cells has been developed in this chapter. After evaluating the effect of diffusion of reactants through a porous layer, it was concluded

that transients in diffusion may be safely assumed to be instantaneous. The data gathered in chapter 2 can be fit with four parameters for steady-state simulation, namely reaction constant and equivalent layer thickness of the cathode, crossover current, and specific ohmic resistance. The possibility of simulating a distributed layer thickness was added, but it appears that its effect is too small to significantly improve the model's fit. Furthermore, it has a heavy computational cost.

The dynamic part of the model included only the overvoltage transient, because it is considered to be the most important. This transient frequently results in overshoots in power output. It was not possible to make a precise parameter regression for the model's capacitance as secondary unmodelled dynamics would have disturbed the result. In future works, impedance spectroscopy may be used to estimate this parameter in frequency ranges where the secondary dynamics do not interfere with measurements.

The overvoltage transient was illustrated graphically by introducing the concept of instantaneous characteristic, which has been used to explain qualitatively the shape of some transients. A theorem was demonstrated to show how the power overshoot associated to the overvoltage transient can make perfect control of the power output theoretically possible.

Bibliography

[1] Jay B. Benziger, I. G. Kevrekidis, M. B. Satterfield, W. H. J. Hogarth, and J. P. Nehlsen. The power performance curve for engineering analysis of a fuel cell. In *AIChE Annual Meeting*, 2005.

[2] M. Ceraolo, C. Miulli, and A. Pozio. Modelling static and dynamic behaviour of proton exchange membrane fuel cells on the basis of electro-chemical description. *Journal of Power Sources*, 113:131–144, 2003.

[3] Sampath Yerramalla, Ased Davari, Ali Feliachi, and Tamal Biswas. Modeling and simulation of the dynamic behaviour of a polymer electrolyte membrane fuel cell. *Journal of Power Sources*, 124:104–113, 2003.

[4] U. Krewer, T. Schultz, and K. Sundmacher. Direct methanol polymer electrolyte fuel cell: Transfer function analysis of current-voltage dynamics. In *Fuel Cell Research Symposium: Modeling and Experimental Validation*. Swiss Federal Institute of Technology, March 2004. http://www.energie-schweiz.ch/internet/03309/index.html.

[5] P. R. Pathapati, X. Xue, and J. Tang. A new dynamic model for predicting transient phenomena in a PEM fuel cell system. *Renewable energy*, 30:1–22, 2005.

[6] J. C. Amphlett, R. F. Mann, B. A. Peppley, P. R. Roberge, and A. Rodrigues. A model predicting transient responses of proton exchange membrane fuel cells. *Journal of Power Sources*, 61:183–188, 1996.

[7] Zijad Lemeš, Andreas Vath, Th. Hartkopf, and H. Mäncher. Dynamic fuel cell models and their application in hardware in the loop simulation. *Journal of Power Sources*, 154: 386–393, 2006.

[8] Yuyao Shan and Song-Yul Choe. A high dynamic PEM fuel cell model with temperature effects. *Journal of Power Sources*, 145:30–39, 2005.

[9] Federico Zenith, Helge Weydahl, Ingrid Anne Lervik, Trygve Burchardt, Steffen Møller-Holst, Sigurd Skogestad, and Georg Hagen. Modelling and experimental study of the transient response of fuel cells. In *9th Ulm ElectroChemical Talks*, pages 82–83, 2004.

[10] Zhenyu Liu, Jesse S. Wainright, Morton H. Litt, and Robert F. Savinell. Study of the oxygen reduction reaction (ORR) at Pt interfaced with phosphoric acid doped polybenzimidazole at elevated temperature and low relative humidity. *Electrochimica Acta*, 51:3914–3923, 2005.

[11] John Newman and Karen E. Thomas-Alyea. *Electrochemical Systems*, chapter 8: Models for Electrode Kinetics, pages 212–213. John Wiley & Sons, 3rd edition, 2004.

[12] Arvind Parthasarathy, Bhasker Davé, Supramaniam Srinivasan, A. John Appleby, and Charles R. Martin. The platinum microelectrode/Nafion interface: An electrochemical impedance spectroscopic analysis of oxygen reduction kinetics and Nafion characteristics. *Journal of the Electrochemical Society*, 139(6):1634–1641, June 1992.

[13] John Newman and Karen E. Thomas-Alyea. *Electrochemical Systems*. John Wiley & Sons, 3rd edition, 2004.

[14] J. Ross Macdonald and William R. Kenan. *Impedance Spectroscopy, emphasizing solid materials and systems*. Wiley-Interscience, 1987.

[15] Jay Benziger, E. Chia, J. F. Moxley, and I.G. Kevrekidis. The dynamic response of PEM fuel cells to changes in load. *Chemical Engineering Science*, 60:1743–1759, 2005.

[16] Carl H. Hamann, Andrew Hamnet, and Wolf Vielstich. *Electrochemistry*. Wiley-VCH, 1998.

[17] James Larminie and Andrew Dicks. *Fuel Cell Systems Explained*. Wiley, 1st edition, 1999.

[18] Ned Mohan, Tore M. Undeland, and William P. Robbins. *Power Electronics: Converters, Applications and Design*. John Wiley & Sons, Inc., 2nd edition, 1995.

[19] Federico Zenith, Frode Seland, Ole Edvard Kongstein, Børre Børresen, Reidar Tunold, and Sigurd Skogestad. Control-oriented modelling and experimental study of the transient response of a high-temperature polymer fuel cell. *Journal of Power Sources*, 162(1): 215–227, 2006.

Chapter 4

Mass and Energy Modelling

Most dynamic models of fuel cells published in the open literature are based on mass and energy balances. Some of these are very detailed in the phenomena they model, and there are also applications of computational fluid dynamics to obtain two- or three-dimensional simulations in which temperature, compositions, pressure and current density can have variable values in every point of the fuel cell.

These studies are of high value, but are also computationally demanding. As this thesis is concerned with control of fuel cells, a simpler model will be presented. The goal of this model, rather than high accuracy, is to present the essential dynamic phenomena of interest for control. For this simpler task, a lumped (zero-dimensional) model with some simplifying assumptions was chosen. Any deviations between the simple model and the real behaviour of the fuel cell may be taken care of by a feedback loop in the control system.

4.1 Literature Review

One of the first dynamic models for fuel-cell systems was published in the literature by He [1] in 1994. He considered a molten-carbonate fuel-cell stack fed with reformate hydrogen, and focused mostly on mass flows and energy balance of the pre-processing plant and of the cell stack. The electrochemical model was comparatively simple, with no dynamics and being, essentially, a Thevenin equivalent circuit with a voltage generator and a resistance.

A dynamic model for PEM fuel cells by Amphlett et al. [2] appeared in 1996, and was subsequently quoted in a large number of papers. It was a thermal model with a basic, empirical modelling of the overvoltage effects. Current was considered a system input, and the catalytic overvoltage was assumed to vary instantly as a

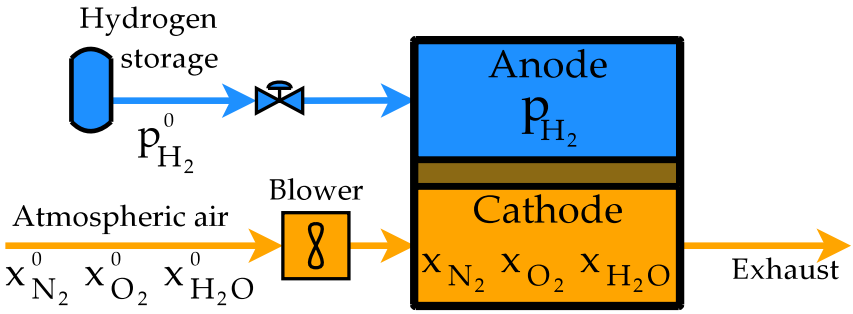

Figure 4.1: A possible configuration for the reactant flows of a fuel cell. The anodic flow is pure hydrogen and is dead-ended, whereas the cathodic flow is atmospheric air and has an exhaust to take out water and nitrogen as oxygen in replenished.

function of temperature, oxygen concentration and current. The model predicts well the behaviour of the stack in a time scale of minutes, but, since it does not consider the transient in overvoltage, it might be less accurate in the scale of seconds and lower.

The issue of managing the water-content dynamics in Nafion membranes was recognized by van Bussel et al. [3], who identified the possibility of great variations in current density in the same cell when operated on dry gases, and stressed the beneficial effect of higher water content in the anode gas.

The model presented by Meng and Wang [4] provided a detailed simulation of flows in three dimensions using computational fluid dynamics. Their model included transients in reactant concentration in bulk and diffusion layers for both electrodes, water production, diffusion and electro-osmosis, but it did not include the overvoltage transient. Similar models have been proposed by Nguyen et al. [5] and Zou et al. [6].

A three-dimensional dynamic model focused on water transport has been studied by Wang and Wang [7, 8]. They concluded that anode back-diffusion would take some seconds to compensate for an anodic dry-out caused by an increase in current, causing significant voltage losses at the anode. In extreme conditions, these losses may reverse the cell voltage. Gas-diffusion transient were found to be much faster, in the range of 10^{-1} to 10^{-2} s.

4.2 Mass Balances

Of the many possible flow configurations to deliver reactants to a fuel cell, the one chosen for this thesis is shown in figure 4.1. The essential difference between fuel cells and batteries is that fuel cells have a continuous feed of fuel and oxidant (for example hydrogen and air), whereas batteries contain the reactants themselves. The requirement on the presence of species is twofold:

1. Mass balances require that a sufficient amount of reactants is present in both electrodes of the fuel cell to sustain the reaction;

2. Reaction kinetics requires reactants to be present in concentrations higher than a certain threshold, ideally as high as possible, in order to reduce the catalytic losses in voltage and increase efficiency.

As expressed by equation 3.20, the exchange current density depends on the presence of reactants, and possibly other species. Any variation in exchange current density i_0 is going to be directly mirrored into the reaction current density i_r, since the Butler-Volmer equation (3.21) states that $\mathrm{i}_\mathrm{r} \propto \mathrm{i}_0$. In fact, the expression for exchange current density is the one and only point where the electrochemical model presented in chapter 3 interacts with reactant concentration.

Gases are usually fed into a fuel-cell stack through a manifold from which the gases can enter the single cells. The cells may be connected in parallel, with a single manifold connecting all the cells, or in series, with each cell's outlet feeding the next cell's inlet, or a mixture of these approaches, possibly with many smaller manifolds spanning a certain number of cells. If the gas entering a manifold contains inert components, or if reaction products are going to appear on that side of the cell, an exit manifold will be required. We will first consider the mass and energy balances for a single cell, and we will then look at how the manifold layouts influence our analysis.

4.2.1 Dead-End Flows

Some gas flows do not need an outlet, since all of the entering flow is going to be consumed and no products will be generated on that side of the fuel cell. This is generally the case of pure hydrogen fed to the anode of PEM fuel cells. In the case of Nafion membranes, hydrogen may also be humidified to improve membrane conductivity and avoid dry-out, and water will permeate to the cathode along with the protons.

For the case of an anode fed on pure hydrogen, the equation of mass conservation is simply:

$$\frac{d\,n_{H_2}}{d\,t} = \dot{n}_{H_2} - \frac{i_r\,A}{2\,F} \tag{4.1}$$

Assuming that the ideal gas law is valid, $n_{H_2} = \frac{p_{H_2}\,\mathcal{V}}{R\,T}$, which after derivation gives:

$$\frac{d\,n_{H_2}}{d\,t} = \frac{\mathcal{V}}{R\,T}\left(\frac{d\,p_{H_2}}{d\,t} - \frac{p_{H_2}}{T}\frac{d\,T}{d\,t}\right) \tag{4.2}$$

Inserting expression 4.1 and rearranging as a dynamic equation of pressure:

$$\frac{d\,p_{H_2}}{d\,t} = \frac{R\,T}{\mathcal{V}}\left(\dot{n}_{H_2} - \frac{i_r\,A}{2\,F}\right) + \frac{p_{H_2}}{T}\frac{d\,T}{d\,t} \tag{4.3}$$

The last term may be neglected if temperature transients are sufficiently slow, since transients in pressure are typically faster than ones in temperature.

In a real system there are always some impurities associated with hydrogen: therefore, some form of periodic purging will be necessary even for dead-end flows. This has not been modelled here because it is assumed to be a discontinuous and relatively rapid process. If the fraction of impurities in the entering flow is significant, an open-end flow layout may be more appropriate.

4.2.2 Open-End Flows

When flows passing through the fuel cell contain inert components, poisons, or receive some reaction products such as water, they require an outlet to remove these non-reacting species.

In all types of PEM fuel cells, this is always the case for cathodic gases, as water forms on the cathode and must be disposed of. In the important case of air-fed cells, inerts in the form of nitrogen represent almost 80 % of the entering molar flow, and in addition to that comes air humidity. This is also the case for anodic gases whenever hydrogen is not pure, for instance when hydrogen gas has been produced by a reformer and is still contains amounts of carbon oxides and water vapour.

Diffusion Limits

The main problem posed by inert gases is the appearance of diffusion limits. Simplifying the Stefan-Maxwell equations, an approximate limit to the reaction current has been obtained in equation 3.9, considering only the cathode. At this limiting

current, the steady-state partial pressure of oxygen at the reaction surface reaches zero: this limit is often named the mass-transport barrier in the literature.

The limiting current, as can be seen in equation 3.9, is proportional to the partial pressure of oxygen in the bulk (outside the diffusion layer) for small oxygen concentrations. When oxygen is more dominant, the dependence becomes weaker, and eventually disappears when pure hydrogen is fed and $p_{H_2O,b} = p_{N_2,b} = 0$. Even if the cell is fed pure oxygen, however, the mass-transport barrier will not disappear, as water still has to exit the diffusion layer. To move the current limit to higher values and allow more power output from the cell, therefore, it is necessary to increase the fraction of oxygen in the cathode gases. The simplest approach is to increase the inlet flow to purge inerts and bring oxygen closer to its inlet concentration.

For the case of an impure hydrogen flow on the anodic side, in presence of CO, CO_2 and H_2O (as would be the case for the outlet of a hydrocarbon reformer), an expression similar to equation 3.9 can be derived:

$$i_{L,a} = p_{H_2,b} \frac{2F}{\lambda R T} \left(\frac{p_{CO,b}}{p D_{H_2,CO}} + \frac{p_{CO_2,b}}{p D_{H_2,CO_2}} + \frac{p_{H_2O,b}}{p D_{H_2,H_2O}} \right)^{-1} \tag{4.4}$$

Again, to increase the current limit one would have to increase the partial pressure of hydrogen in the bulk gas, $p_{H_2,b}$. However, whereas air is obtained for free from the environment, the anode exhaust gases would still contain valuable hydrogen. Therefore, when operating open-ended, the anode outlet may deliver gas to a utility that may make use of it, such a gas turbine, a burner for a heating unit, or a purifying unit from which the remaining hydrogen can be extracted and recycled back to the anode.

Effects of Bulk Oxygen Concentration

As the partial pressure of oxygen in the cathode's bulk influences the shape of the cell's polarisation curve, a series of simulations has been performed with parameters from table 3.2 to determine its effect.

The composition of air in a fuel cell's cathode changes as oxygen reacts with hydrogen to form water vapour. For a given oxygen conversion, the number of moles for the three gas species considered (oxygen, nitrogen and water) and their total is:

$$\begin{cases} n_{O_2} = n^0_{O_2}\,(1 - X) \\ n_{N_2} = n^0_{N_2} \\ n_{H_2O} = n^0_{H_2O} + 2\,X\,n^0_{O_2} \\ \sum_i n_i = \sum_i n^0_i + X\,n^0_{O_2} \end{cases} \tag{4.5}$$

Where X is conversion and n^0_i is the initial number of moles of generic species i. Since the molar fraction of a generic species i is by definition $x_i = \frac{n_i}{\sum_i n_i}$, the molar fractions will be a function of conversion according to the following relations:

$$\begin{cases} x_{O_2} = \dfrac{x^0_{O_2}\,(1 - X)}{1 + x^0_{O_2}\,X} \\ x_{N_2} = \dfrac{x^0_{N_2}}{1 + x^0_{O_2}\,X} \\ x_{H_2O} = \dfrac{x^0_{H_2O} + 2\,x^0_{O_2}\,X}{1 + x^0_{O_2}\,X} \end{cases} \tag{4.6}$$

We will assume that the initial feed has a total pressure of 101 325 Pa (a standard atmosphere). The partial pressure of water is assumed to correspond to 1700 Pa, the vapour pressure of water at approximately 15 °C, or a relative humidity of 53 % at 25 °C. The remaining dry air is assumed to be made up of 20 % oxygen and 80 % nitrogen.

With various values of X, the polarisation curve calculated with equation 3.14 changes as shown in figure 4.2. It is noticeable how the mass-transport barrier recedes almost linearly with conversion, and that some conversion is actually beneficial at low currents: the reason is that an increase in water vapour will increase the exchange current density (3.20), actually promoting the reaction. This latter positive effect is however limited in extent.

The maximum power outputs for the polarisation curves of figure 4.2 are shown in figure 4.3 as a function of conversion, along with the corresponding oxygen and water molar fractions. It is noticeable how the maximum available power varies almost linearly with all of these variables.

These results are valid for a fuel cell whose cathodic bulk partial pressures are as given by equation set 4.6. This is the case for a fuel cell whose open-end cathode manifold operates as a steady-state CSTR (with perfect mixing), and with no perturbations in the entering composition.

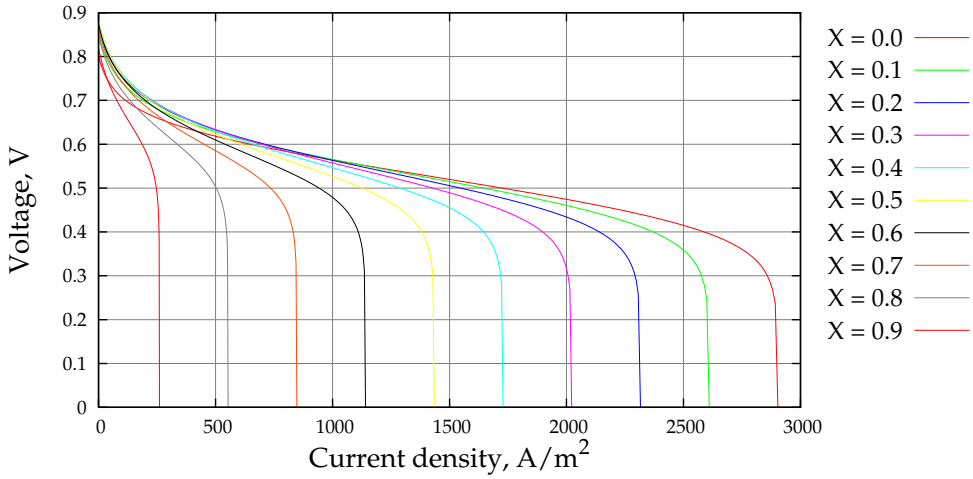

Figure 4.2: Polarisation curves of a fuel cell as oxygen conversion advances due to the reaction. The cell's parameters are those reported in table 3.2.

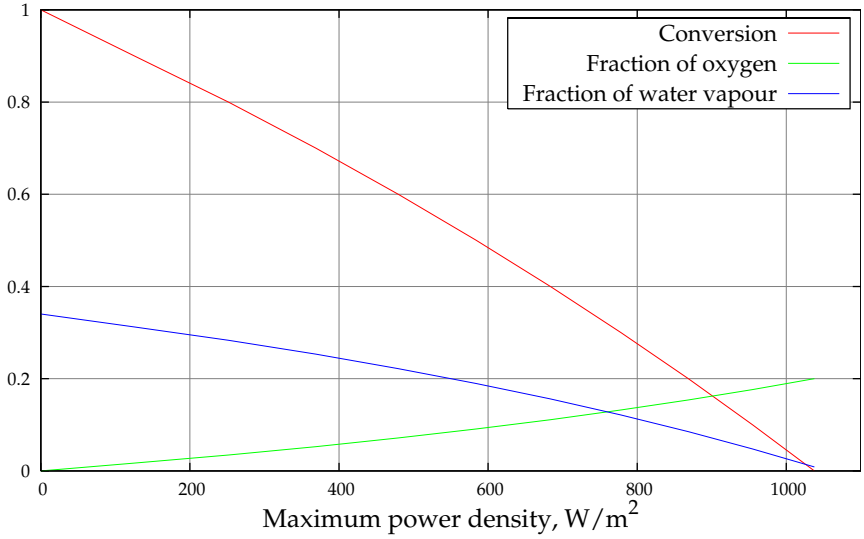

Figure 4.3: The maximum allowable conversion in the cathode's bulk (with corresponding molar fractions of oxygen and water vapour) for various levels of power output from a fuel cell.

Figure 4.3 can therefore be used to derive a simple rule-of-thumb for fuel cells of the type investigated in this thesis: a fuel cell's maximum power output is approximately proportional to oxygen partial pressure. This implies that the air flow in the cathode should be large in order to produce more power.

Mass-Balance Equations for Open-End Flows

For a generic species i, the dynamic mole balance in an open-end flow is:

$$\frac{d\,n_i}{d\,t} = \dot{n}^{in}\,x_i^{in} - \dot{n}^{out}\,x_i + \nu_i\,\frac{i_r\,A}{F} \tag{4.7}$$

The stoichiometric factor ν_i indicates how many moles of the species are produced or consumed for every mole of electrons transferred. Since the anodic and cathodic reactions are, respectively:

$$\begin{aligned} \tfrac{1}{2}H_2 &\longrightarrow H^+ + e^- \\ \tfrac{1}{4}O_2 + H^+ + e^- &\longrightarrow \tfrac{1}{2}H_2O \end{aligned} \tag{4.8}$$

we have that $\nu_{O_2} = -\frac{1}{4}$, $\nu_{H_2} = -\frac{1}{2}$, $\nu_{H_2O} = \frac{1}{2}$ and $\nu_{N_2} = 0$.

When pressure is constant, the total outlet molar flow depends only on the transients in reaction rate and temperature, and can be calculated by the following relation:

$$\dot{n}^{out} = \dot{n}^{in} + \overbrace{\sum_i \nu_i\,\frac{i_r\,A}{F}}^{\text{Reaction}} + \overbrace{\frac{p\,\mathcal{V}}{R\,T^2}\frac{d\,T}{d\,t}}^{\text{Heat expansion}} \tag{4.9}$$

Inserting this expression for $\dot{n}^{out}$ into equation 4.7 and assuming constant pressure, the molar balance becomes:

$$\begin{aligned} \frac{p\,\mathcal{V}}{R\,T}\frac{d\,x_i}{d\,t} - x_i\cancel{\frac{p\,\mathcal{V}}{R\,T^2}\frac{d\,T}{d\,t}} &= \dot{n}^{in}\,\left(x_i^{in} - x_i\right) + \frac{i_r\,A}{F}\left(\nu_i - x_i\sum_j \nu_j\right) - x_i\cancel{\frac{p\,\mathcal{V}}{R\,T^2}\frac{d\,T}{d\,t}} \\ \frac{p\,\mathcal{V}}{R\,T}\frac{d\,x_i}{d\,t} &= \dot{n}^{in}\,\left(x_i^{in} - x_i\right) + \frac{i_r\,A}{F}\left(\nu_i - x_i\sum_j \nu_j\right) \end{aligned} \tag{4.10}$$

Fortunately, the heat expansion term cancels out when expressing the dynamics in terms of molar fraction rather than number of moles. This is a series of differential equations in molar fractions x_i. In a control setting, we can view $\dot{n}^{in}$ as the

manipulated variable, since it can be set with an air blower or a compressor, and i_r as a disturbance, since it is a consequence of the external load connected to the fuel cell. It is well worth remarking that this system is nonlinear.

4.3 Energy Balance

Energy balance and temperature dynamics are important topics for PEM fuel cells. Nafion-based PEM cells operate in a narrow temperature range, usually around 80 °C (more if pressurised), whereas PBI membranes can operate in a range spanning from 125 to 200 °C. High temperatures may be exploited to reduce the catalytic overvoltage by increasing the value of reaction constant k in table 3.2, or to increase tolerance to catalyst poisons such as CO.

Temperature control in Nafion-based PEM cells is usually taken care of by a dedicated cooling system for all but the smallest cell stacks [9]. This cooling system requires additional channels to be machined out in the cell's bipolar plates, which are the most expensive part of a fuel cell [9], adding to their cost and complicating design. The necessity of such a cooling system arises from the low temperatures of exhaust gases, which reduce their associated enthalpy flow, making it difficult to remove all the heat generated by the cell only by means of the exhaust flows.

4.3.1 Air Cooling

Fuel cells with PBI instead of Nafion as membrane material operate at higher temperatures, and the need for of a separate cooling system could be eliminated by simply feeding the cell stack additional air at ambient temperature [10]. To quickly verify this possibility, we will consider a simple back-of-the-envelope calculation for the case of maximum power output from a PBI fuel cell with parameters from table 3.2, at 150 °C and fed with pure hydrogen and dry air at standard ambient temperature (25 °C). Our goal is to find out what air excess ratio, defined as the ratio of air fed to the cell versus the required stoichiometric air flow, is necessary to remove all produced heat at the operating point of maximum power output[1].

The overall reaction in the fuel cell is the well-known oxidation of hydrogen:

$$H_2 + \tfrac{1}{2}O_2 \rightleftharpoons H_2O_{(g)} \tag{4.11}$$

As shown in figure 4.3, the maximum electric power output is about $1\,kW/m^2$; the corresponding polarisation curve in figure 4.2 indicates a voltage of about 0.35 V

[1] Since the maximum power output is also the point of minimum efficiency for normal operation of fuel cells, it will also be the point of maximum heat output.

at maximum power. The standard enthalpy of reaction 4.11 does not change much with temperature, and in the temperature range we are interested in (125 to 200 °C) it is about $\Delta h_r^0 \approx -243\,\mathrm{kJ/mol}$. As the energy we are taking out of the system as electric power is $0.35\,\mathrm{V} \times 2\,\mathrm{F} = 67.5\,\mathrm{kJ/mol}$, a cell at maximum electric power output will produce about 175 kJ/mol of heat.

The stoichiometric quantity of air for the reaction is 2.5 moles per mole of product water, as 0.5 moles of oxygen are required by reaction 4.11. The heat capacity of air in the temperature range of interest is about 30 J/mol K. Assuming that air enters the cell at a standard temperature of 25 °C and leaves it at 150 °C, and that the reaction of oxygen to water does not significantly alter the flow's heat capacity, a stoichiometric air flow will remove $30\,\mathrm{J/mol\,K} \times 2.5\,\frac{\mathrm{mol_{air}}}{\mathrm{mol_{H_2O}}} \times (150 - 25)\,\mathrm{K} = 9375\,\mathrm{J/mol}$ from the cell. The air excess ratio that will dissipate the cell's heat output will then be about $\frac{175000}{9375} \approx 18.6$. Whereas this value may appear high, it is not unusual for fuel cells [9], and will be required only in the case of maximum power output.

This approximate calculation has shown that cooling a PBI fuel-cell stack by using only air as a cooling medium is possible.

4.3.2 External Heating for Cold Start-up

When the stack is at low temperatures, typically at start-up, it might be difficult to bring it to operational temperature, as the reaction cannot proceed at too low temperatures and internal heat generation is therefore not possible.

In order to provide a separate heat input, we will consider the possibility of injecting and burning hydrogen in the air inlet stream to raise its temperature. This method is wasteful of hydrogen, but has the benefit of simplicity in analysis and realisation, and delivers heat directly where it is needed (the cathode's reactants), instead of heating first the whole stack and its plates. This layout is presented in figure 4.4.

4.3.3 Enthalpy-Balance Equations

The main sources and sinks of heat for the fuel cell of figure 4.4 are entering and exiting flows, the heat generated by the cell, and losses to the environment. An enthalpy balance around the stack and the burner yields:

$$\frac{\mathrm{d}\,H}{\mathrm{d}\,t} = \dot{H}^{\mathrm{in}} - \dot{H}^{\mathrm{out}} - \overbrace{i_r\,V\,A}^{\text{Electric power}} - \dot{H}^{\mathrm{loss}} \tag{4.12}$$

This simple model assumes only one temperature to be representative of the

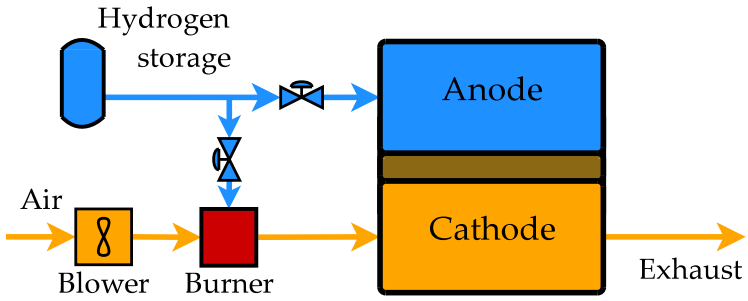

Figure 4.4: Flow layout for a PBI fuel cell with air cooling and heating with hydrogen combustion.

whole cell. Indeed, according to results published by Shan and Choe [11], temperatures across the various elements of a cell (plates, gas channels, MEA) tend to be fairly uniform. In fact, in a later study, the same authors [12] noted that the temperature in a whole stack is quite uniform, with the exception of the cells at the ends of the stack. Their studies were however focused on low-temperature PEM fuel cells, and should be verified for PBI membranes.

The relationship between enthalpy content of a cell and its temperature may be extracted by data published in the literature [11], where one can find that the heat capacity per cell area is about $7\,\mathrm{kJ/K\,m^2}$. It is therefore:

$$\frac{\mathrm{d}\,H}{\mathrm{d}\,t} = A\,\hat{c}_p\,\frac{\mathrm{d}\,T}{\mathrm{d}\,t} \tag{4.13}$$

The entering enthalpy flow also contains the heat generated by the combustion of hydrogen when heating of the cell is required, as for example in a cold start. It will therefore be equal to the enthalpy associated to the ambient air plus the entering hydrogen flow:

$$\dot{H}^{in} = \dot{n}_{air}\,h_{air}(T_0) + \left(\dot{n}_{H_2} + \dot{n}^{c}_{H_2}\right)\,h_{H_2}\left(T_{H_2}\right) \tag{4.14}$$

Temperature T_{H_2} may be significantly different from ambient temperature T_0, as hydrogen from storage may undergo a significant expansion, be evaporated from liquid state, or heated in order to dissociate it from hydrides. Modelling the dynamics of hydrogen inlet temperature is beyond the scope of this thesis, and we will assume that hydrogen has been brought to ambient conditions, and that therefore $T_{H_2} = T_0$.

We assumed that the only output in our fuel cell is the cathode's. The cathode gas composition will change as oxygen is consumed, and the total outlet molar flow will be larger or equal than the entering one.

$$\dot{H}^{out} = \sum_i \dot{n}_i^{out} h_i(T) \tag{4.15}$$

$\dot{n}_i^{out}$ represents the sum of the entering flow of species i, $\dot{n}_i^{in}$, plus the moles created (or minus the ones consumed) by the reaction between hydrogen and oxygen. Lastly, there is a small effect of thermal expansion of gases if temperature is varying. If pressure is constant, the outlet molar flow for species i is:

$$\dot{n}_i^{out} = \overbrace{\dot{n}_i^{in}}^{\text{Entering}} + \overbrace{\nu_i \left(\dot{n}_{H_2}^{c} + \frac{i_r A}{2F} \right)}^{\text{Reaction with } H_2} + \overbrace{x_i \frac{p \mathcal{V}}{R T^2} \frac{dT}{dt}}^{\text{Heat expansion}} \tag{4.16}$$

The functions $h_i(T)$ depend on the temperature T of the cell's cathode.

The heat loss to the environment, $\dot{H}^{loss}$, would generally be a beneficial factor as the main issue in a functioning PBI fuel-cell stack would be removing heat from the stack rather than withholding it. However, its actual expression will depend on the stack materials and layout: for sake of simplicity, we will assume $\dot{H}^{loss} = 0$.

4.4 Cell Stacks

As fuel cells can produce only limited voltages, usually below 1 V, the obvious method to electrically connect a stack of fuel cells is to connect them in series, to produce larger voltages.

Other networks in need of a layout are the ones used to deliver the reactants at cathodes and anodes. The flows can be arranged in series through all cells, or with a common manifold for all cell inlets, or with a combination of these.

The series flow layout guarantees that the same flow rate will pass through all cells, and obstacles to flow, such as liquid water accumulation in Nafion-based cells, can be removed mechanically by the flow itself. With a parallel layout, instead, the cell in which liquid water accumulates would cause more resistance to flow, leading to less flow in the cell, less water removal, and lower concentration of reactants that might even deplete. In these conditions, reaction would halt in the cell: this has far-reaching consequences, as the current through the whole stack would be halted, since the stack is still electrically connected in series.

However, since the series flow layout assumes that all the flow will pass through each cell, the stack's pressure drop will rapidly increase with the number of cells.

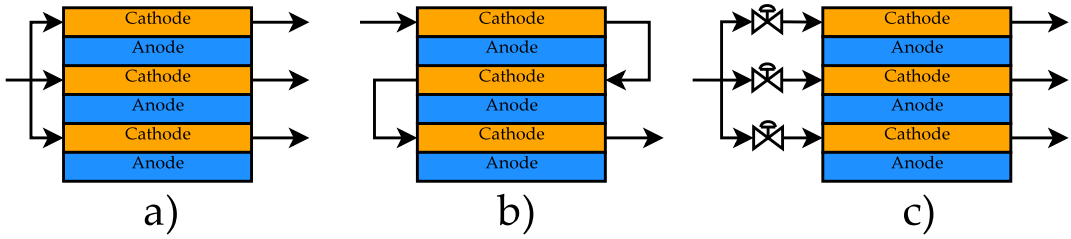

Figure 4.5: Various arrangements of the air flow through a fuel-cell stack: a) parallel flow, b) serial flow, and c) sequentially exhausted flow [13].

If a parallel-connected stack has a pressure drop $\Delta p_{parallel}$, the pressure drop of the same stack, with a series flow layout and the same total stack flow, will have to be multiplied with the number of cells n, as the pressure drop through the n cells will sum up from stack inlet to stack outlet, and with its square n^2, since the flow of all n cell will pass through each cell and pressure drop increases roughly with the square of flow. Therefore, the pressure drop of series-connected stacks will be much higher than for parallel-connected ones:

$$\Delta p_{series} \approx n^3 \, \Delta p_{parallel} \tag{4.17}$$

For a stack of 50 cells, not a particularly large number, the series layout's pressure drop will be an impressive 125 000 times the pressure drop of an equivalent parallel-connected stack. Furthermore, the series flow will change its composition and temperature while travelling through the cells, collecting heat and reaction products, and causing each cell to be under different conditions. These limitations of series-flow arrangements were already apparent to Litz and Kordesch [14] in 1965, and series layouts are therefore applied in shorter stacks only, such as those investigated by Dhathathreyan et al. [15]. In larger stacks, such as those that could be used in vehicles, compression costs represent the main energy losses of ancillary plants in the system [16], and a large increase in pressure drop is unacceptable.

Nafion-based PEM fuel-cell stacks need the qualities of both layouts: the water-removal capability of the series layout and the scalability of the parallel layout. Nguyen and Knobbe [13] devised a conceptually simple approach where cells are sequentially exhausted, so that liquid water accumulation is staved off and the gas stream must not travel needlessly through all cells; however, this requires a series of regulating valves for each cell. As the cells operate batch-wise between each water purging, the frequency of this water purging must be sufficiently rapid so that oxygen is not depleted: with large stacks and high currents, the required switching

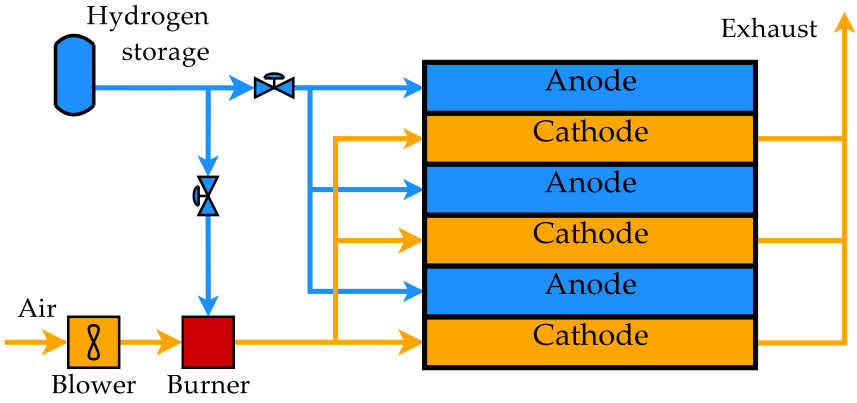

Figure 4.6: The flow layout considered in this thesis, here exemplified for a three-cell stack.

rate may prove to be very high and unpractical. This approach was further refined by Knobbe et al. [17], who suggested installing a separate valve at the outlet of each cell, and the possibility of purging the cells by group rather than one by one. The main categories of flow layouts are sketched in figure 4.5.

PBI-based PEM fuel cells, instead, do not require any water management, and can be stacked with much simpler parallel layouts for both anodic and cathodic flows. Karimi et al. [18] have investigated various possible layouts for parallel flow in fuel cells, simulating the pressure drop and voltage spread of a 51-cell stack with different inlet and outlet positionings; they found that one of the best layouts with single inlet and outlet is the Z configuration, where the outlet is on the opposite side of the stack relative to the inlet.

The overall flow network assumed in this thesis is shown in figure 4.6. Hydrogen is fed in parallel to the cell anodes, whereas the air network (possibly after burning some hydrogen for heating) is arranged in a Z configuration.

Bibliography

[1] Wei He. A simulation model for integrated molten carbonate fuel cell systems. *Journal of Power Sources*, 49:283–290, 1994.

[2] J. C. Amphlett, R. F. Mann, B. A. Peppley, P. R. Roberge, and A. Rodrigues. A model predicting transient responses of proton exchange membrane fuel cells. *Journal of Power Sources*, 61:183–188, 1996.

[3] Hubertus P. L. H. van Bussel, Frans G. H. Koene, and Ronald K. A. M. Mallant. Dynamic model of solid polymer fuel cell water management. *Journal of Power Sources*, 71: 218–222, 1998.

[4] Hua Meng and Chao-Yang Wang. Large scale simulation of polymer electrolyte fuel cells by parallel computing. *Chemical Engineering Science*, 59:3331–3343, 2004.

[5] Phong Thanh Nguyen, Torsten Berning, and Ned Djilali. Computational model of PEM fuel cells with serpentine gas flow channels. *Journal of Power Sources*, 130:149–157, 2004.

[6] Jiang Zou, Xiao-Feng Peng, and Wei-Mon Yan. Dynamic analysis of gas transport in cathode side of PEM fuel cell with interdigitated flow field. *Journal of Power Sources*, 159:514–523, 2006.

[7] Yun Wang and Chao-Yang Wang. Transient analysis of polymer electrolyte fuel cells. *Eletrochimica Acta*, 50:1307–1315, 2005.

[8] Yun Wang and Chao-Yang Wang. Dynamics of polymer electrolyte fuel cells undergoing load changes. *Electrochimica Acta*, 51:3924–3933, 2006.

[9] James Larminie and Andrew Dicks. *Fuel Cell Systems Explained*. Wiley, 1st edition, 1999.

[10] Jianlu Zhang, Zhong Xie, Jiujun Zhang, Yanghua Tang, Chaojie Song, Titichai Navessin, Zhiqing Shi, Datong Song, Haijiang Wang, David P. Wilkinson, Zhong-Sheng Liu, and Steven Holdcroft. High temperature PEM fuel cells. *Journal of Power Sources*, 160:872–891, 2006.

[11] Yuyao Shan and Song-Yul Choe. A high dynamic PEM fuel cell model with temperature effects. *Journal of Power Sources*, 145:30–39, 2005.

[12] Yuyao Shan and Song-Yul Choe. Modeling and simulation of a PEM fuel cell stack considering temperature effects. *Journal of Power Sources*, 158:274–286, 2006.

[13] Trung Van Nguyen and Mack W. Knobbe. A liquid water management strategy for PEM fuel cell stacks. *Journal of Power Sources*, 114:70–79, 2003.

[14] Lawrence M. Litz and Karl V. Kordesch. Technology of hydrogen-oxygen carbon electrode fuel cells. In George J. Young and Henry R. Linden, editors, *Fuel Cell Systems*, volume 47 of *Advances in chemistry*, pages 166–187. American Chemical Society, 1965.

[15] K. S. Dhathathreyan, P. Sridhar, G. Sasikumar, K. K. Ghosh, G. Velayutham, N. Rajalakshmi, C. K. Subramaniam, M. Raja, and K. Ramya. Development of polymer electrolyte membrane fuel cell stack. *International Journal of Hydrogen Energy*, 24:1107–1115, 1999.

[16] P. Corbo, F. E. Corcione, F. Migliardini, and O. Veneri. Experimental assessment of energy-management strategies in fuel-cell propulsion systems. *Journal of Power Sources*, 157:799–808, 2006.

[17] M. W. Knobbe, W. He, P.Y. Chong, and T.V. Nguyen. Active gas management for PEM fuel cell stacks. *Journal of Power Sources*, 138:94–100, 2004.

[18] G. Karimi, J. J. Baschuk, and X. Li. Performance analysis and optimization of PEM fuel cell stacks using flow network approach. *Journal of Power Sources*, 147:162–177, 2005.

Part II

Control of Fuel Cells

Chapter 5

Control Structure for Fuel Cells

To devise appropriate control algorithms for fuel cells, it is essential to understand the nature of the control problem first. Once the application environment of fuel cells has been clearly described, it is then necessary to identify the best control variables so that the system will behave as required.

This chapter will focus on a general control structure for fuel cells, using results from the previous chapters. Once the overall control framework is clear, the next chapters will consider the specific control algorithms in closer detail.

5.1 Literature Review

Some early interest in control of fuel cells arose in the late sixties, when the main issue being investigated was controlling the concentration of hydrazine or methanol in alkaline fuel cells [1, 2], then considered viable portable power sources for battlefield military applications. The issue was complicated by the difficulty of measuring the actual reactant concentration in the electrolyte, which was the main problem being debated at the time. Ang et al. [2] suggested, for example, to use a dedicated measuring cell. However, these papers did generally not contain much control theory (if any at all), and their focus on hydrazine- and methanol-fuelled alkaline fuel cells make them of little relevance for today's mostly hydrogen-fuelled PEM fuel cells.

Two similar US patents have been granted to Lorenz et al. [3] and Mufford and Strasky [4], both concerning methods to control the power output of a fuel cell. Both these methods use air inflow as the input variable. Whereas this variable can indeed be set by manipulating the air-compressor speed, there are various reasons why this choice of input variable is not the best option. First of all, only the fuel cell

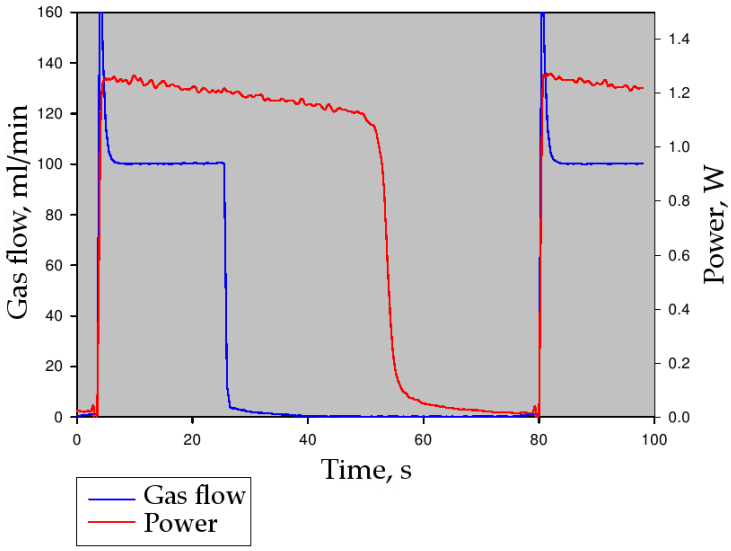

Figure 5.1: Experimental data showing the relationship between reactant feed rate to a fuel cell and the cell's power output (from Johansen [12]).

itself is considered: no information from the utility that will draw power from the cell is being used. Also, while it could seem intuitive that a fuel cell will produce more power the more oxidant it is fed, this neglects a series of phenomena such as the mass-transport limit, the strong nonlinear effects of oxygen partial pressure in cathode kinetics, diffusion of oxygen through the cathode and accumulation of oxygen in the cathode manifold; in short, a fuel cell cannot always output as much power as the reactant it is fed.

The PhD thesis by Pukrushpan [5] and an article by the same author and others [6] are among the first important contributions to control of PEM fuel cells. Most of the focus is on air-inflow control, with a significant section about control and modelling of natural-gas fuel processors. Notwithstanding the high quality of the work, Pukrushpan assumed, based on a presentation by Guzzella [7], that the time constants of electrochemical phenomena in fuel cells are in the order of magnitude of 10^{-9} seconds[1]. Pukrushpan did therefore not elaborate further on the electrochemical transient, whereas other authors have found that the time constants for the electrochemical transients are actually much higher [8, 9, 10, 11].

[1] In Pukrushpan's thesis it is in fact claimed to be 10^{-19} s, but this is probably due to a transcription error.

Rune Johansen[2], a student at the Department of Materials Technology at NTNU, investigated in his master's thesis [12] the possibility of using reactant feed rate as an input in a control loop. As shown in figure 5.1, when the feed rate[3] was shut down, the fuel cell continued to produce power at an almost undisturbed rate, but dropped later, after about one minute. On the other hand, as soon as the reactant feed was reopened, the power output immediately reattained the previous values. This indicates that there is a dead time in which reactants in the manifolds must be consumed before the effect of reduced partial pressure can be apparent; the actual extent of this delay will depend, among other things, on the sizing of the manifolds and on the rate of consumption of reactants. This effect, which is the same one encountered at the mass-transport limit when operating a fuel cell in normal conditions, is known to be nonlinear with reactant concentration, and its occurrence roughly corresponds with the depletion of one of the reactants at the reaction sites. It must also be remarked that these effects are often not known precisely, as the cell's behaviour depends on many variables such as temperature, humidification, wear, and others.

Johansen's findings indicate that the feed rate of reactants is a poor control input for power-output control. Whereas it can be possible to control a fuel cell in such a way, the large delays and strong nonlinearities associated with the input's effect on the system will severely limit the system's performance in reference tracking and disturbance rejection. Furthermore, such a system would be an energetically inefficient control through reactant starvation.

The first publication about fuel cells in the Journal of Process Control was by Shen et al. [13]. They modelled a molten-carbonate fuel cell using neural networks tuned with input-output data, and synthesised an adaptive fuzzy controller. The control problem they considered was to control the stack's temperature by manipulating the reactant flows. Another neural-network approach was considered by El-Sharkh et al. [14] to control the power output from a fuel-cell unit comprising a DC/AC inverter; in their layout, the fuel cell's output voltage is controlled by the inflow of reactants.

Golbert and Lewin [15] studied the application of model-predictive control to fuel cells. They claimed that a sign inversion in the static gain between power output and current barred the possibility of using a fixed-gain controller with integral action, since it could not have stabilised such a process. They proceeded therefore to

[2]Readers interested in contacting Johansen should be aware that he has since changed his surname into Hoggen.

[3]Johansen modified the hydrogen feed rate, but his conclusion is specular for oxygen on the cathodic side.

synthesise a model-predictive controller. Throughout the paper, Golbert and Lewin assume that current is a manipulable input, and use it to control the power output. However, Jay Benziger pointed out that it is not possible to use current (or voltage, which Golbert and Lewin's model also allows) as an input: he suggested the impedance of the external circuit as the variable one should rather use [16].

Caux et al. [17] considered a system comprising a fuel cell, a compressor, valves, and two DC/DC converters (a booster and a buck-boost converter). The analysis of the complete system is a step forward from the studies where the fuel cell had been seen as a separate entity from the rest of the process, but the fuel cell model itself is the same as from Amphlett et al. [18], and is therefore not considering transients in overvoltage; voltage variations will therefore be caused, directly, only by variations in temperature, current or oxygen concentration. A similar layout was investigated by Thounthong et al. [19, 20], with more focus on power electronics control and less on cell modeling, and some experimental results.

According to Gibson [21], controlling the fuel cell is simply a matter of "matching reagent flows to the required current generation, taking into account the fuel cell efficiency factor". However, the cell efficiency factor influences only voltage, as reactant consumption is proportional to reaction current. Furthermore, for most PEM fuel cells, high air-excess ratios are used [22].

Serra et al. [23] used linear-control analysis to synthesise controllers for a fuel cell at different linearisation points. They used Pukrushpan's model [5], and their objective was to control the voltage of a large stack by manipulating valve positions, reactant input and humidification. They concluded that few of these controllers had a wide operating range.

Bao et al. [24, 25] developed a dynamic model that considered anode-flow recirculation as well as cathode-flow and membrane modelling. They neglected transients in overvoltage and temperature of the fuel cell, and in the humidifier unit. Their stated control objective was to control the air stoichiometric ratio, gas pressures and power output by manipulating the air compressor and the output valves. They synthesised both a linear and a nonlinear adaptive controller, mostly geared towards flow control.

Benziger et al. [26] defined the *power-performance curve*, which is a plot of the power output of a fuel cell versus the external resistance applied to it. The work is innovative since it departs from previous assumptions on manipulable variables, but considers only resistive loads. It also claims that the maximum possible efficiency for fuel cells at their maximum power-output conditions is 50 %: this result is due to the way Benziger et al. modelled the fuel cell, that is like a Thevenin equivalent circuit. This is a well-known result from electrical science (known as *maximum*

power transfer theorem), but is applicable to fuel cells only for the simple model used by Benziger: in particular, mass-transport barriers may reduce the maximum power output to areas where efficiency is higher.

Varigonda and Kamat [27] published a review article in which they examined the current status for control of both automotive and stationary fuel-cell systems, and identified present challenges in start-up (especially from freeze conditions), flooding, dry-out and fundamental understanding of the dynamic behaviour; they encouraged an integrated design-and-control approach in addressing these challenges.

The approach of controlling power output by manipulating inlet flows has been experimentally investigated by Woo and Benziger [28]. In their layout, a PEM fuel cell was fed oxygen or air on the cathode side, and pure hydrogen for the anode; all outlet gas streams had to bubble through a water column. When reducing the hydrogen flow below the requirements, the reduction of hydrogen pressure caused water to enter the cell and cover parts of the anode, effectively producing a variable-area cell. The control action resulted in transients in the order of magnitude of 10 s.

Williams et al. [29] tested the dynamic performance of a fuel-cell stack connected to a DC/DC converter controlled with pulse-width modulation. They tested the system in a range of frequencies between 1 and 400 Hz, and claimed that the bandwidth of the fuel-cell system was quite high, about 50 Hz, when controlling it with a PI controller. Unfortunately, there is no clear indication of what type of converter they used (it would appear to be a boost converter, since at low values of duty cycle they experienced the highest currents), nor logs of the current density in the fuel cell through the tests. Brey et al. [30] also tested a stack connected to a boost converter, but focused more on reduction of the voltage ripple produced by the converter.

Choe et al. [31] should probably be credited with the first paper that considers more than one aspect of the dynamics of a fuel cell, namely both converter dynamics and reactant management, applied to a low-temperature PEM fuel cell. They however neglected the dynamics of the electrochemical reaction.

5.2 Dynamic Modes of Fuel Cells

Many of the different results and approaches taken in analysing the dynamics and control of fuel cells is due to the multidisciplinarity of the subject. Figure 5.2 tries to place in a graph the essential dynamic phenomena occurring in a generic fuel-cell system.

Proceeding from reactant input, the first layer of dynamics belongs to chemical engineering, and has been described in chapter 4:

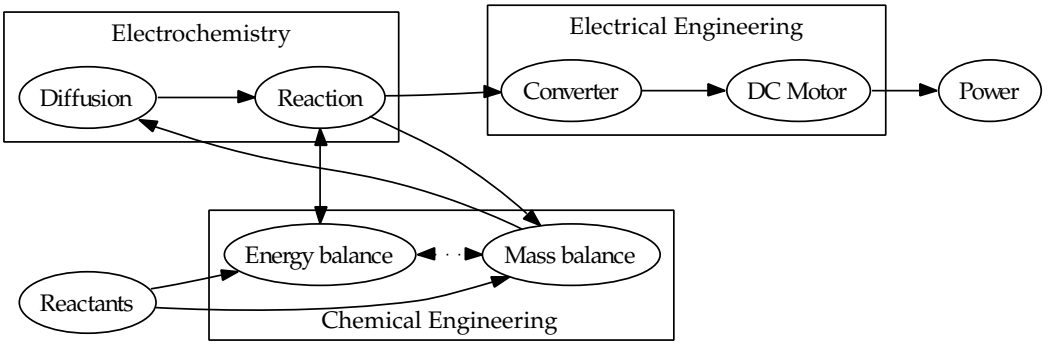

Figure 5.2: The various interacting dynamics that make up the complete dynamics of fuel cells, grouped by their subject of reference.

- The energy balance (4.12) depends on the temperature and compositions of entering flows, and is influenced by the heat produced by the reaction;
- Mass balances (4.10) also depend on the input flows, and on the reaction depleting or producing the various components.

The two types of balances interact to a certain extent, since the flow compositions determine the heat capacity of flows, and temperature is a factor in the time constant of equation 4.10.

The next block belongs to the domain of electrochemistry, described in chapter 3: the multicomponent diffusion through the gas-diffusion layer depends on the bulk partial pressure of components, and determines their partial pressure at the reaction sites: this, together with temperature (on which constant k strongly depends) determines the electrode's exchange current density (equation 3.20). The exchange current density is the most important factor in determining the reaction current density as a function of overvoltage in the Butler-Volmer equation (3.21).

Once electric power leaves the cell, it is generally not in the appropriate form for its intended user. It will then be necessary to convert it to the appropriate current-voltage ratio, or to transform it in AC power, which falls in the domain of electrical engineering.

5.3 Controlling the Reaction Rate

Fuel cells are essentially power-delivering devices. Their purpose is to deliver electric power to a diverse set of users, such as a car's electric motor, the electric grid,

a laptop computer, a mobile phone, or a rural-area local grid not connected to the main national grid. It is clear that one of the main variables of interest in controlling a fuel-cell stack is its power output.

The power output from a fuel cell is generally not in the current-to-voltage ratio required by the user: it is instead dictated by the polarisation curve, the number of cells in the stack, how these cells are electrically connected, the cells' area, temperature, reactant pressure, the presence of catalyst poison and other factors. Some of the physical conditions may vary in different cells of the stack, possibly with disrupting effects as those investigated by Nguyen and Knobbe [32], where a single flooded cell blocked the whole stack's current. For all practical purposes, the large number of variables influencing the voltage-to-current ratio of power output from a fuel-cell stack make it very difficult to set it reliably.

The reaction rate, expressed by the reaction current density i_r, is determined by the Butler-Volmer equation (3.21). Upon inspection, we see that its main terms available for manipulation are overvoltage, temperature and reactant concentration (through the exchange current density, expressed by equation 3.20). We can immediately exclude the possibility of manipulating temperature, since temperature transients are generally slow, and causing them would require a heat source, which would be detrimental to the energy efficiency of the system.

5.3.1 Manipulating the Reactant Feed

The option of using reactant concentration to control the reaction rate has been considered by a number of authors [3, 4, 28], generally by controlling the flows entering into the fuel cell. However, this approach has a series of practical drawbacks:

- Manipulating the flows allows only to increase the reactant concentration: it is not possible to withdraw hydrogen from the anodic side, for example. Only the reaction itself will reduce the concentrations, which means that control performance will be limited by the reaction rate.

- It is known that many fuel cells have a mass-transport limit, that is a reaction rate at which diffusion limitations reduce the reactant concentration at the reaction sites, causing a rapidly increasing loss in the cell's output voltage. The effects of reduced reactant concentration are in most cases negligible in other parts of the polarisation curve: this means that it is necessary to operate at the mass-transport limit for the reactant concentration to have a significant effect on the reaction rate. Control by flow manipulation is therefore control by reactant starvation, which implies unnecessarily low efficiencies.

- When operating on the mass-transport limit, a small change in concentration will have a relatively large effect on the cell's voltage loss. Large gains are usually beneficial for control, but they may become a problem when input uncertainty is present, as in this case. If the flow control system is unable to regulate the reactant concentration in the fuel cell to a very high degree of precision, large errors will result.

- Most fuel cells, when in practical applications, will be arranged in stacks. If reactant flows are arranged in series through the cells, it will be difficult to control the reactant concentrations in each cell separately, since the reactants that have to reach the last cell must first pass through all the other ones. If the flow is instead arranged in parallel, differences in construction details may result in different flows through the cells, again hindering precise control of the reactant concentration in each cell. Controlling each parallel flow through the cells, an approach similar to the one proposed by Nguyen and Knobbe [32] and Knobbe et al. [33], is a possible solution, but requires many control valves (see figure 4.5 for diagrams).

In short, controlling reaction rate with reactant inflow suffers from delays when reducing the rate, inherently low cell efficiency, large gains whose uncertainty will make the system difficult to control, and is difficult to apply in stacks. This control layout is in principle realisable, but its performance will be very limited: the uncertainties on its high gains and the actuator delays will require a slow feedback controller.

5.3.2 Manipulating the External Circuit

The last and most important variable influencing the reaction rate is the overvoltage. The overvoltage is determined by the accumulation of charge in the model's capacitance (see figure 3.5), which is the integration of the difference between the reaction current i_r and the electron flow $i + i_c$ (equation 3.24). The only one of these variables that is set from an entity other than the fuel cell is i, which is set by the intersection of the load's characteristic with the cell's. It seems natural, therefore, to control the rate of reaction by manipulating in some way the external circuit.

One simple strategy is using linear control, intended as placing a variable load, such as a rheostat or a MOSFET, in the circuit ("line") between the fuel cell and the load, as illustrated in figure 5.3. The resistance of this new component can then be manipulated to control some system variables, such as the voltage applied on the load or the circuit current. Whereas this layout is simple, it is also inherently

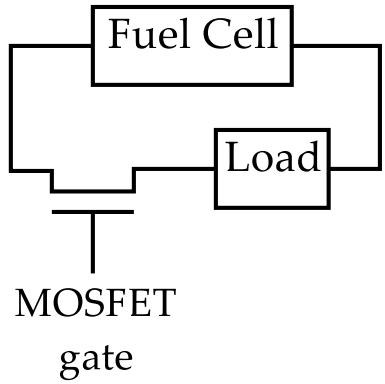

Figure 5.3: A linear control layout: the MOSFET increases its resistance to dissipate excess power that should not reach the load.

inefficient, as the manipulated load is effectively dissipating excess power, and it is also unable to provide the load with voltages beyond the fuel cell's.

A more efficient alternative is using power electronics, such as DC/DC converters. Converters have the advantage of being able to modify the voltage-to-current ratio of DC power without significant losses. Depending on the type of converter, it is also possible to increase the output voltage beyond the input's value. The converter's purpose is usually formulated as to set the output voltage, either to a constant set point in the case of connection to a DC bus, or to follow a variable reference. In the latter case, the converter's output voltage may be used as a manipulated variable in a cascade control structure. The main disturbances in this layout will be the input voltage from the fuel cell and the output current from the load, which we have left unspecified until this point. As it was shown in theorem 3.11.1, there is no inherent limitation to the power-output performance of fuel cells caused by the electrochemical transient, that can in theory be instantly set to any value between zero and maximum nominal power; the limitations to control performance on the electric side of the system will come from the DC/DC converter rather than from the fuel cell itself.

5.4 Controlling Reactant Concentrations

Having decided to use a DC/DC converter to control the rate of reaction, it is necessary to make sure that reactants are in place in the fuel cell's electrodes so the reaction may proceed at the required rate. It is natural to do this by manipulating

the reactant inflows, though one must keep in mind that it is the reactant concentration at the reaction sites that counts for the reaction rate: assuming one controls the bulk reactant concentration by manipulating the reactant inflow, one has also to set this concentration high enough so that reaction-site concentration does not approach zero by a reasonably safe margin.

Dead-end manifolds, such as those used for pure hydrogen, may be controlled by a simple feedback pressure controller. As pressure dynamics and measurements are usually fairly fast, tight control should not pose particular problems.

Open-end manifolds, such as those used for air and hydrogen from reforming, are more complex. Our objective is to maintain reactant concentration in the bulk over a threshold value that will sustain the current reaction rate, but also provide sufficient reactant in the bulk so that when the reaction rate is stepped, the input flow has the time to adjust to the new flow rate before the reactant runs out.

For the case of air and reformed hydrogen, the streams entering the cell stack will be at low (atmospheric) pressure, which means they will have to be forced through the stack. A sensible manipulated variable will therefore be the input flow, assuming certain dynamics for the blower or compressor.

5.5 Controlling Stack Temperature

The stack temperature is influenced essentially by the entering flows (upon which the exiting ones depend) and the reaction rate. The reaction rate is already set according to the requirements of the electric utility, so the only remaining way to influence the stack's temperature is using the entering flows.

The entering flows are already used to control reactant concentrations, but, since reactant concentrations higher than the minimum threshold value are not a problem, we can increase the entering flows to cool the stack and remove excess heat. This is going to be the standard operating mode, where we manipulate the entering flows to maintain stack temperature close to the reference.

As air is obtained essentially for free from the environment, we should use only the air flow for temperature control. The fuel gases on the anode manifold are much more valuable and should not be wasted more than strictly necessary to maintain a sufficient hydrogen partial pressure at the reaction sites.

When the stack temperature needs to be increased and the corresponding control action would be to reduce the entering flows below the minimum set by the concentration controller, we can either accept a reduced control action or manipulate other inputs. Another input may be to burn fuel on the cathode inlet, thereby increasing the entering enthalpy flow. This is a simple strategy to start up a cold

stack, where reaction alone produces no or too little power.

A problem with temperature control is actually deciding which temperature should be the reference for the controller. Higher temperatures reduce the catalytic losses, increase tolerance towards poisons such as CO, but also reduce the mechanical strength and arguably the durability of the membrane. Currently, no applicable mathematical model of these phenomena is available in the open literature. Whereas a control system for stack temperature may be built, the criteria for deciding its set point will be left unspecified.

5.6 Conclusions

The generic control structure devised in this chapter for a fuel-cell system is pictured in figure 5.4, and consists of four control loops:

- The hydrogen pressure in the anode's manifold will be controlled by a feedback loop based on a pressure measurement, since these are easy and fast. This choice assumes hydrogen is free of pollutants, otherwise a layout similar to the cathode manifold will have to be adopted.
- The oxygen partial pressure in the cathode manifold is adjusted according to measurements in the exiting oxygen concentration. This loop may be challenging because of the delay in measurement of oxygen concentration and the fact that composition measurements are slower than other types of measurements. The controller will determine which maximum conversion is allowable based on the power output (see figure 4.3), and regulate the air inflow blower or compressor accordingly.
- Temperature will be set by a controller operating on the blower. To resolve the conflict with the composition controller, a simple maximum selector will pick whichever of the two signals that requires the higher flow. When this selector prioritises the composition controller, the temperature controller may either wait or resort to use another manipulated variable, such as a hydrogen burner.
- The output voltage from a DC/DC converter connected to the stack is controlled by manipulating the converter's input. The output voltage is selected because, as will be shown in section 6.3, this is the most common input to a DC electric motor or a DC bus.

Most of the control loops associated to flow and temperature will benefit from some feedforward action, such as estimating the rate of consumption of reactants

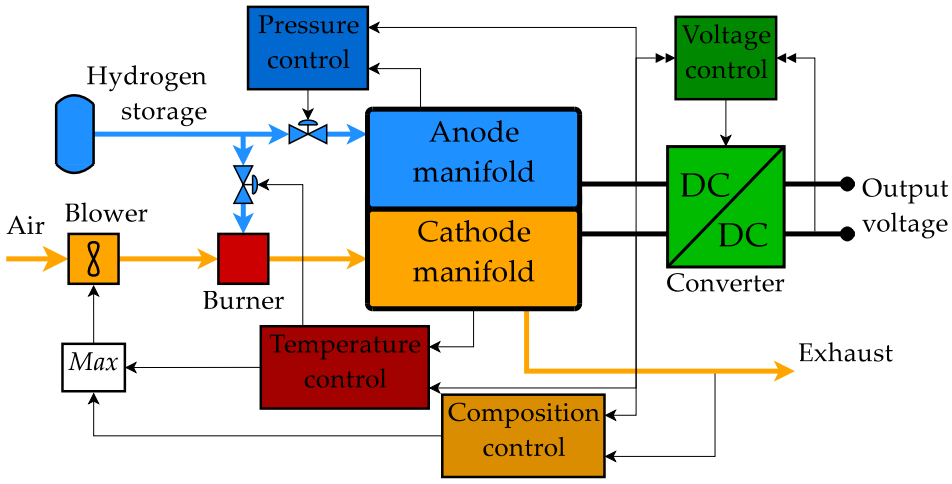

Figure 5.4: The proposed layout for a PBI-membrane fuel-cell stack, with its various subsystems.

by measuring the cell's output current, and the heat generation in the cell using the output power and the first-law efficiency. This is especially important for the cathode composition controller, as it relies on a slow measurement for its feedback loop, yet the dynamics of air composition in the cathode bulk may be very fast at high rates of reactant consumption.

Bibliography

[1] *22nd Annual Power Sources Conference*, May 1968.

[2] P.G. P. Ang, H. H. Ewe, E. W. Justi, and A. W. Kalberlah. A simple miniaturized methanol-feed control for fuel cells. *Energy Conversion*, 12:65–68, 1972.

[3] Helmut Lorenz, Karl-Ernst Noreikat, Thomas Klaiber, Wolfram Fleck, Josef Sonntag, Gerald Hornburg, and Andreas Gaulhofer. Method and device for vehicle fuel cell dynamic power control. US patent 5 646 852, July 1997. Assigned to Daimler-Benz Aktiengesellschaft.

[4] W. Edward Mufford and Douglas G. Strasky. Power control system for a fuel cell powered vehicle. US patent 5 771 476, June 1998. Assigned to DBB Fuel Cell Engines GmbH.

[5] Jay Tawee Pukrushpan. *Modeling and control of fuel cell systems and fuel processors*. PhD thesis, Department of Mechanical Engineering, University of Michigan, Ann Arbor, Michigan, USA, 2003.

[6] Jay Tawee Pukrushpan, Anna G. Stefanopoulou, and Huei Peng. Modeling and control for PEM fuel cell stack system. In *American Control Conference*, 2002. TP09-2.

[7] Lino Guzzella. Control oriented modelling of fuel-cell based vehicles. In *NSF workshop on the integration of modeling and control for automotive systems*, 1999.

[8] M. Ceraolo, C. Miulli, and A. Pozio. Modelling static and dynamic behaviour of proton exchange membrane fuel cells on the basis of electro-chemical description. *Journal of Power Sources*, 113:131–144, 2003.

[9] P. R. Pathapati, X. Xue, and J. Tang. A new dynamic model for predicting transient phenomena in a PEM fuel cell system. *Renewable energy*, 30:1–22, 2005.

[10] Helge Weydahl, Steffen Møller-Holst, and Georg Hagen. Transient response of a proton exchange membrane fuel cell. In *Joint International Meeting of The Electrochemical Society*, 2004.

[11] Federico Zenith, Frode Seland, Ole Edvard Kongstein, Børre Børresen, Reidar Tunold, and Sigurd Skogestad. Control-oriented modelling and experimental study of the transient response of a high-temperature polymer fuel cell. *Journal of Power Sources*, 162(1): 215–227, 2006.

[12] Rune L. Johansen. Fuel cells in vehicles. Master's thesis, Norwegian University of Science and Technology, 2003.

[13] Cheng Shen, Guang-Yi Cao, Xin-Jian Zhu, and Xing-Jin Sun. Nonlinear modeling and adaptive fuzzy control of MCFC stack. *Journal of Process Control*, 12:831–839, 2002.

[14] M. Y. El-Sharkh, A. Rahman, and M. S. Alam. Neural-network based control of active and reactive power of a stand-alone PEM fuel cell power plant. *Journal of Power Sources*, 135:88–94, 2004.

[15] Joshua Golbert and Daniel R. Lewin. Model-based control of fuel cells: (1) regulatory control. *Journal of Power Sources*, 135:135–151, 2004.

[16] Jay Benziger. oral comment at the annual meeting of the American Institute of Chemical Engineers in Austin, 2004.

[17] S. Caux, J. Lachaize, M. Fadel, P. Shott, and L. Nicod. Modelling and control of a fuel cell system and storage elements in transport applications. *Journal of Process Control*, 15:481–491, 2005.

[18] J. C. Amphlett, R. F. Mann, B. A. Peppley, P. R. Roberge, and A. Rodrigues. A model predicting transient responses of proton exchange membrane fuel cells. *Journal of Power Sources*, 61:183–188, 1996.

[19] Phatiphat Thounthong, Stéphane Raël, and Bernard Davat. Control strategy for fuel cell/supercapacitors hybrid power sources for electric vehicle. *Journal of Power Sources*, 158:806–814, 2005.

[20] Phatiphat Thounthong, Stéphane Raël, and Bernard Davat. Test of a PEM fuel cell with low voltage static converter. *Journal of Power Sources*, 153:145–150, 2006.

[21] A. C. Gibson. *Instrument Engineers' Handbook—Process Control and Optimization*, volume II, chapter 8.26, pages 1952–1965. CRC–Taylor & Francis, 4th edition, 2005.

[22] James Larminie and Andrew Dicks. *Fuel Cell Systems Explained*, chapter 4: Proton Exchange Membrane Fuel Cells, pages 71–77. Wiley, 1st edition, 1999.

[23] Maria Serra, Joaquín Aguado, Xavier Ansede, and Jordi Riera. Controllability analysis of decentralised linear controllers for polymeric fuel cells. *Journal of Power Sources*, 151: 93–102, 2005.

[24] Cheng Bao, Minggao Ouyang, and Baolian Yi. Modeling and control of air stream and hydrogen flow with recirculation in a pem fuel cell system–I. Control-oriented modeling. *International Journal of Hydrogen Energy*, 31:1879–1896, 2006.

[25] Cheng Bao, Minggao Ouyang, and Baolian Yi. Modeling and control of air stream and hydrogen flow with recirculation in a pem fuel cell system–II. Linear and adaptive nonlinear control. *International Journal of Hydrogen Energy*, 31:1897–1913, 2006.

[26] Jay B. Benziger, M. Barclay Satterfield, Warren H.J. Hogarth, James P. Nehlsen, and Ioannis G. Kevrekidis. The power performance curve for engineering analysis of fuel cells. *Journal of Power Sources*, 155:272–285, 2006.

[27] Subbarao Varigonda and Mithun Kamat. Control of stationary and transportation fuel cell systems: Progress and opportunities. *Computers and Chemical Engineering*, 30:1735–1748, 2006.

[28] Claire H. Woo and Jay B. Benziger. PEM fuel cell current regulation by fuel feed control. *Chemical Engineering Science*, 62:957–968, 2007.

[29] Keith A. Williams, Warren T. Keith, Michael J. Marcel, Timothy A. Haskew, W. Steve Shepard, and Beth A. Todd. Experimental investigation of fuel cell dynamic response and control. *Journal of Power Sources*, 163:971–985, 2007.

[30] J. J. Brey, C. R. Bordallo, J. M. Carrasco, E. Galván, A. Jimenez, and E. Moreno. Power conditioning of fuel cell systems in portable applications. *International Journal of Hydrogen Energy*, 2007. (In press).

[31] Song-Yul Choe, Jung-Gi Lee, Jong-Woo Ahn, and Soo-Hyun Baek. Integrated modeling and control of a PEM fuel cell power system with a PWM DC/DC converter. *Journal of Power Sources*, 164:614–623, 2007.

[32] Trung Van Nguyen and Mack W. Knobbe. A liquid water management strategy for PEM fuel cell stacks. *Journal of Power Sources*, 114:70–79, 2003.

[33] M. W. Knobbe, W. He, P.Y. Chong, and T.V. Nguyen. Active gas management for PEM fuel cell stacks. *Journal of Power Sources*, 138:94–100, 2004.

Chapter 6

Converter Control

As was concluded in chapter 5, the reaction rate in a fuel cell is determined by the external load. This chapter focuses on the control of buck-boost converters and the effect such control will have on fuel cells.

The most common techniques to control a converter are pulse-width modulation [1] and sliding-mode control [2]. Both techniques are based on the manipulation of a switch that changes the converter's structure: in sliding-mode control the switch is set to its ON or OFF state depending on a set of logic rules, which are recalculated at very short intervals. In pulse-width modulation, instead, introduces the concept of duty ratio(see figure 6.1): it represents the fraction of time the switch is in the ON position, and varies between 0 and 1. In mathematical terms, sliding-mode control uses the discrete set $\{0, 1\}$, whereas pulse-width modulation uses the continuous set $[0, 1]$.

In pulse-width modulation, it is common to operate with averaged units [3], as the complete modulation cycle T is usually (though not always) designed to be much faster than other transients in the converter.

This chapter will present a series of possible approaches to the control problem:

- Pulse-width modulation, applied with:
  - $\mathcal{H}_\infty$ control with local linearisation;
  - Feedforward control and half-delay filtering;
  - Input-output linearisation;
- Switching rules based on sliding-mode control.

Another possible technique is model-predictive control, as suggested by Geyer et al. [4]; since the time required for online optimisation largely exceeds the require-

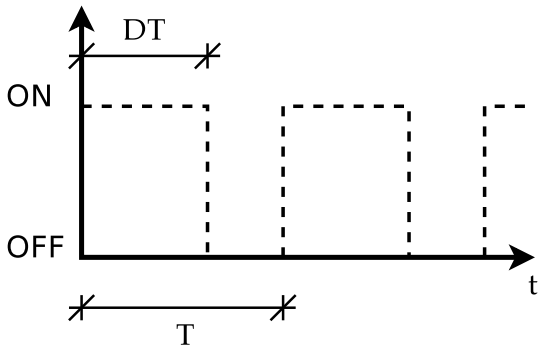

Figure 6.1: Definition of the duty ratio D as a fraction of the time the switch is left in the ON position. The total period T is usually very small, but there is a limit to how short it can be, set by the switching losses.

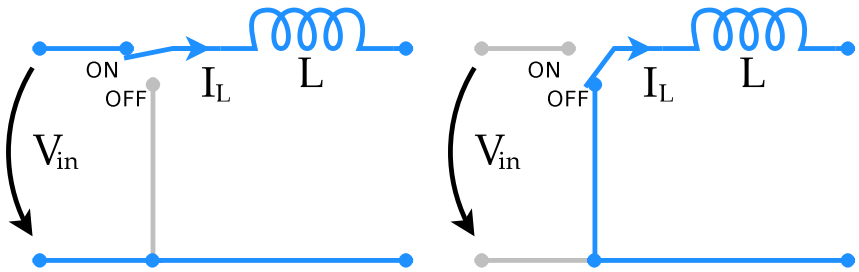

Figure 6.2: A basic representation of a buck converter, in its ON and OFF configurations.

ments, the authors suggested using a state-feedback piecewise affine controller [5]. Application of $\mathcal{H}_\infty$ controllers has also been studied by Naim et al. [6].

6.1 Choice of Converter Type

A DC/DC converter has the objective of transforming the power from a source (in our case a fuel cell) into an appropriate form. According to Luo and Ye [7], there are over 500 different topologies of converters. The most simple are the boost converter, that increases voltage from input to output, and the buck converter, that decreases it; other relatively simple types are the buck-boost and the Ćuk converters.

Buck converters, sketched in figure 6.2, are very simple and easy to build. The voltage source, in our case the fuel cell stack, is connected to a switch. When the

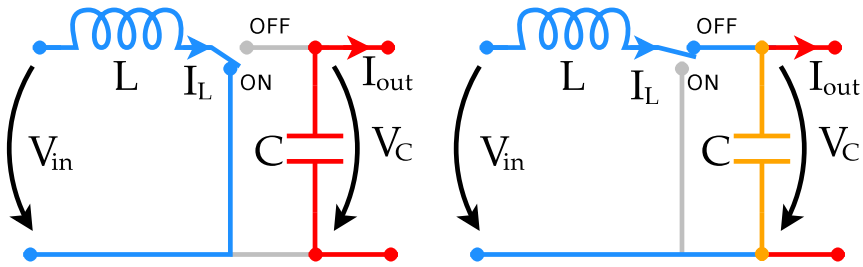

Figure 6.3: A basic representation of a boost converter, in its ON and OFF configurations.

switch in ON, the source is connected to the output through an inductance[1]. When the switch is OFF, the inductance maintains the current in the output, because the inductor current cannot change stepwise. The fraction of time the switch is on will determine the output voltage. The buck converter has the convenience of delivering an output voltage linear in the fraction of time the switch is in the ON position, but this means that it cannot deliver voltages higher than the stack's. As we usually desire increasing the stack voltage, this converter type is not viable.

On the other hand, the boost converter (pictured in figure 6.3) is able to deliver voltages higher than the stack's, but not lower ones; the former is however the range we are most interested in. When the switch is ON, the source will charge an inductor. When the switch is OFF, the inductor's current will be directed to the outer circuit, where a capacitor maintains a constant voltage. However, a serious issue arises by examining the converter's mode of operation in figure 6.3: current is always passing through the stack, even if the converter is not delivering any power to an external load. In particular, when the switch is left in the ON position (the condition corresponding to no power being transferred to the output), the stack will charge the inductor and increase its current until it reaches its mass-transport limit: the stack would consume the maximum amount of reactants when no power is actually required at all. This is clearly unacceptable for efficiency reasons, as most applications of fuel cells involve variable loads and will be left idle at some time.

At the price of increased complexity, we can have the advantages of both buck and boost converter types with the buck-boost converter, sketched in figure 6.4. The voltage source is connected in parallel, through a switch, to an inductor. When the switch is ON, the inductor accumulates power by storing energy in its magnetic field. When the switch is OFF, the current is forced into the capacitor (with which

[1]This inductance can in fact be part of the load connected to the converter, reducing the converter itself to a mere switch.

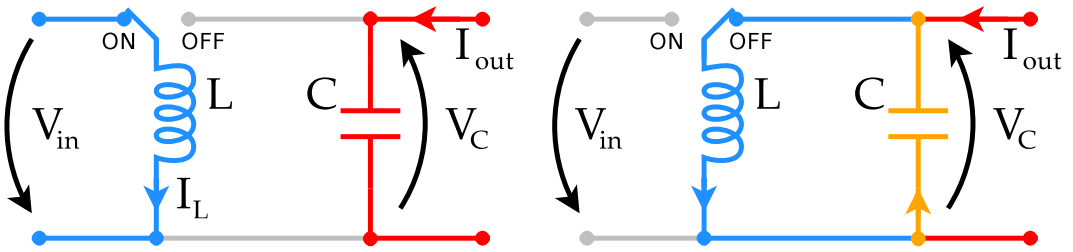

Figure 6.4: A basic representation of a buck-boost converter, in its ON and OFF configurations.

the inductor is now in parallel), moving the energy stored in the inductor's magnetic field into the capacitor's electric field. Independently from the switch's state, the capacitor is continuously exchanging power with an external load, as in the boost converter. Buck-boost converters can convert input voltages into any value of voltage (though only of opposite sign, and not when accounting for losses), and do not cause the stack to short circuit when the switch is left OFF. However, they present a more difficult control problem as neither the ON state nor the OFF state can move power from the input to the output by itself: it will be necessary to find an appropriate intermediate value of duty ratio.

Buck-boost converters have been chosen as the converter type to consider in this thesis. However, in a real-world application, a more complex layout may be preferred, to include the possibility of regenerative braking and reverse drive. For sake of simplicity, we will consider only the case of a simple converter, with values $L = 0.94\,\mathrm{mH}$ and $C = 3.2\,\mathrm{mF}$ [8]. When modelling internal losses, we will assume an internal resistance $R = 3\,\mathrm{m\Omega}$.

6.2 Effects of Discontinuous Currents in the Input

In buck and buck-boost converters a discontinuous current passes through the input, in our case a fuel-cell stack: this causes a particular type of loss in the fuel cell.

If i is the current density passing through the fuel cell, the cell's overvoltage will be approximately constant at $\eta \approx \eta(i\,D)$, that is, it will be a function of the current averaged over a modulation period T[2]. However, the loss due to internal resistance will change instantaneously, as the $r\,i$ term does not involve an integral over time as

[2]For ease of notation we are neglecting the crossover current density. However, including it would have no consequence on the conclusions.

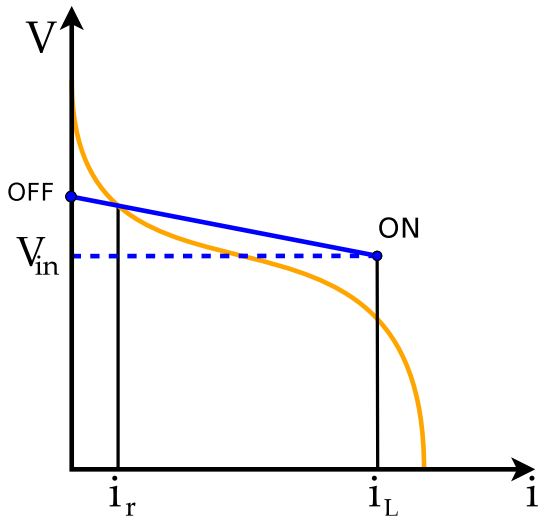

Figure 6.5: Diagram of a fuel cell's operating points when connected directly to a buck or buck-boost DC/DC converter.

η does. The voltage obtained by the fuel cell when current is passing will therefore be:

$$V_{in} = E - \eta(i\,D) - r\,i \tag{6.1}$$

The current passing through the fuel cells is a series of pulses whose average is $i\,D$, but the ohmic voltage loss is due to the whole value of i. Figure 6.5 illustrates the problem: reaction current $i_r = i\,D$ determines the position of the instantaneous characteristic, but, when the switch is in the ON position, the operating point will result in a voltage V_{in} lower than the steady-state cell voltage corresponding to current i_r.

The additional voltage loss is quantified as $r\,i(1-D)$, or equivalently $r\,i_r\frac{1-D}{D}$. When quantitative values from table 3.2 are inserted, it turns out that this loss may be significant, in particular at low values of D. This has been confirmed by simulations in which cells dimensioned for a certain maximum power could deliver only a fraction of that.

The fundamental cause of this additional loss is that current passes in short pulses instead of continuously: the same amount of charge is transferred in only a fraction of the available time. It is however possible to work around this problem by letting the fuel cell operate in parallel with a capacitance, which will in turn be

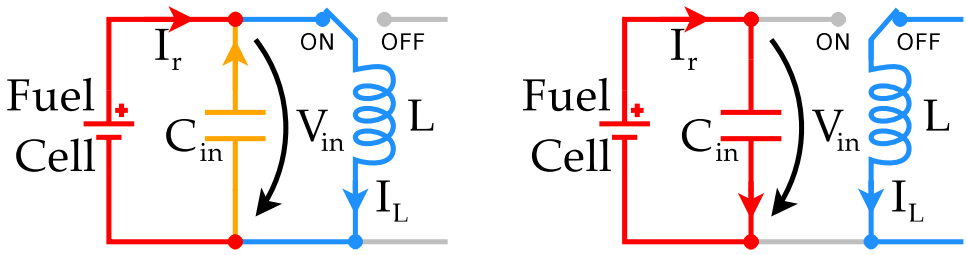

Figure 6.6: Effect of the insertion of a capacitance between a fuel cell and a buck-boost converter (only inductor shown). The current through the cell and the converter's input voltage are maintained roughly constant through the modulation cycle.

connected to the converter, as shown in figure 6.6.

In the layout presented in figure 6.6, capacitance C_{in} will maintain an approximately constant voltage in parallel with the fuel cell and the converter, while its current will switch back and forth as it is charged by the fuel cell and discharged by the converter's inductor.

Capacitance C_{in} may be designed to be of any value, as long as it is large enough to maintain an approximately constant value through the modulation cycle. A large capacitance will reduce the ripple effects induced by the converter's switching and allow a smoother operation of the cell stack, and may also serve as a buffer between the energy requirements of the converter and the fuel cell, possibly allowing more time for the system that controls reactant inflow to react and provide a higher concentration of reactant when the power requirement is stepped up.

This capacitance may be roughly dimensioned as follows: since the capacitor's voltage depends on the simple differential equation $C\dot{V} = i$, we may approximate this as $C\frac{\Delta V}{\Delta t} = i$. Using a modulation period $\Delta t = 10^{-5}\,s$, a worst-case value for current of about 1 kA, and a requirement on V not to oscillate more than 1 V, we can approximate:

$$C_{in} \approx \frac{i\,\Delta t}{\Delta V} \approx \frac{10^3\,A\,10^{-5}\,s}{1\,V} \approx 0.1\,F \tag{6.2}$$

6.3 Identifying a Controlled Variable: DC Motors

Since the DC converter will be connected to an utility on its output, it is of interest to shortly examine how such an utility operates. We will consider a DC electric motor.

DC motors have for a long time been the only type of electric motor that could

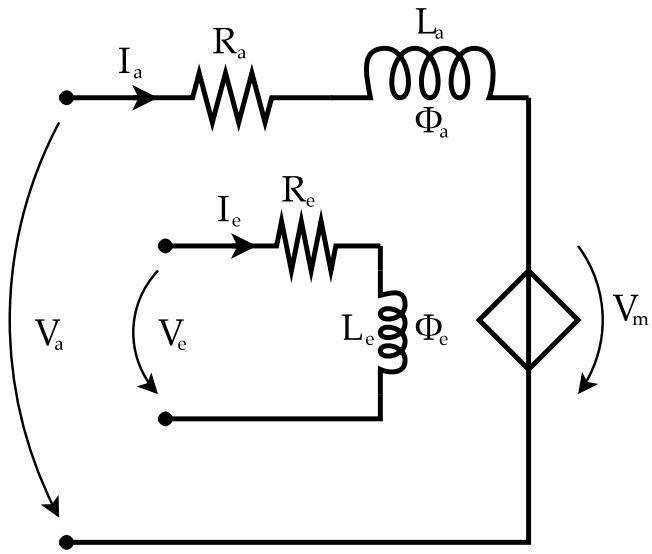

Figure 6.7: A typical model of a DC motor [10]. The inner loop is the field winding, and the outer one is the armature winding.

be easily controlled. The reason of this preference is due to the simplicity of controlling the main variable of interest in DC motors, the input current, as opposed to the difficulty of controlling frequency in AC motors. Whereas microelectronics has made it practical to control AC motors too, all electric motors can be modelled as DC motors [9].

Generally speaking, there are two state variables influencing the power output in a DC motor's mathematical model (figure 6.7): the armature current and the field-winding current. The armature current, I_a, is directly proportional to the torque exerted by the motor, divided by the magnetic field Φ_e. The voltage generator V_m in figure 6.7 represents the counter-electromotive force induced by the rotation of the shaft. Its value is directly proportional to the angular velocity multiplied by the magnetic flux Φ_e.

The field-winding current, which usually absorbs just a small fraction of the total power consumption, generates the magnetic field in which the armature current passes; by weakening the field, it is possible to increase velocity at the expense of torque, by modifying the proportionality ratio between armature current and torque [10].

Such a simplified model can be described by the following equations, where

$c \in \mathbb{R}$ is a constant of the system:

$$V_a = R_a I_a + L_a \frac{d I_a}{d t} + V_m \tag{6.3}$$

$$V_m = c \omega \Phi_e \tag{6.4}$$

$$I_a = \frac{1}{c} \frac{T}{\Phi_e} \tag{6.5}$$

Rearranging equation 6.3, we can more easily see that I_a is a state of the motor.

$$L_a \frac{d I_a}{d t} = V_a - R_a I_a - V_m \tag{6.6}$$

Transposing into the Laplace domain:

$$I_a = \frac{1}{L_a s + R_a} (V_a - V_m) \tag{6.7}$$

Typical values of 20 mH for L_a and 20 mΩ for R_a can be used. For more data, refer to Larminie and Lowry [11], Leonhard [10], or Ong [12]. From a control engineer's point of view, this dynamic system is a simple lag, with I_a as the output and $V_a - V_m$ as the input. The problem of controlling an electric motor usually involves the control the armature current [13], and we therefore assume I_a to be our controlled variable.

The counter-electromotive force V_m is a consequence of shaft rotation, which is often determined by external conditions (such as the speed at which a vehicle is travelling). V_m will therefore be interpreted as a disturbance on the process input, as far as control of the armature current is concerned. It is possible to compensate for this disturbance by manipulating the input voltage V_a. The control problem is therefore to control I_a by manipulating V_a, in spite of disturbance V_m.

We can set voltage V_a by connecting the motor input to a buck-boost converter's output. The converter is in this case acting as an actuator. This is an example of cascade control: control of I_a is obtained by controlling V_a, which is in turn obtained by switching between the buck-boost converter's ON and OFF modes, as illustrated in diagram 6.8.

This brief discussion of the control problem for DC motors indicates therefore that, when controlling a DC/DC converter, our objective should be to control its output voltage, which we will later use to control armature current and thereby motor torque. The case of a fixed-voltage DC bus is a subset of this problem, in which we have a constant set point instead of a variable reference.

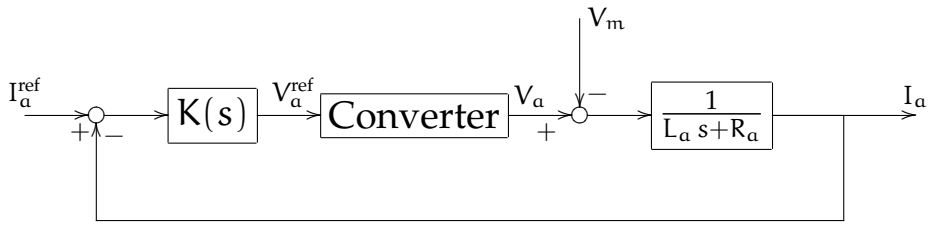

Figure 6.8: A cascade control layout in which the DC/DC converter is used as the actuator to control the armature current in a DC motor.

6.4 Pulse-Width Modulation

Having defined $D \in [0, 1]$ to be the duty ratio, or the fraction of time the switch is in the ON position, it is possible to describe the buck-boost converter of figure 6.4 with the following set of equations (neglecting resistive losses):

$$\begin{cases} L\,\dfrac{d\,I_L}{d\,t} = -V_C(1-D) + V_{in}\,D \\ C\,\dfrac{d\,V_C}{d\,t} = I_L(1-D) - I_{out} \end{cases} \tag{6.8}$$

Where V_C is the capacitor (output) voltage, V_{in} the input voltage, I_L the inductor (input) current and I_{out} the output current.

In this equation system, we assumed that the switching cycle T (as illustrated in figure 6.1) is sufficiently fast that I_L and V_C do not change significantly over it. This system is clearly nonlinear because of its terms $V_C\,D$ and $I_L\,D$.

Assuming that D is kept constant at some value between 0 and 1, and that external disturbances V_{in} and I_{out} remain constant, the trajectory of system 6.8 in the I_L-V_C phase plane has the shape of an ellipse. In a real system, the elliptical trajectory will slowly decay to steady state because of losses not modelled in system 6.8. The system is illustrated in figure 6.9: the steady states are aligned on a line with slope $\frac{V_{in}}{I_{out}}$, departing from $I_L = I_{in}$ and $V_C = 0$. The elliptical trajectories are centered on a point corresponding to the current value of D; when $D = 0$ the steady-state point is the one on the I_L axis, when $D \to 1$ it tends to infinity.

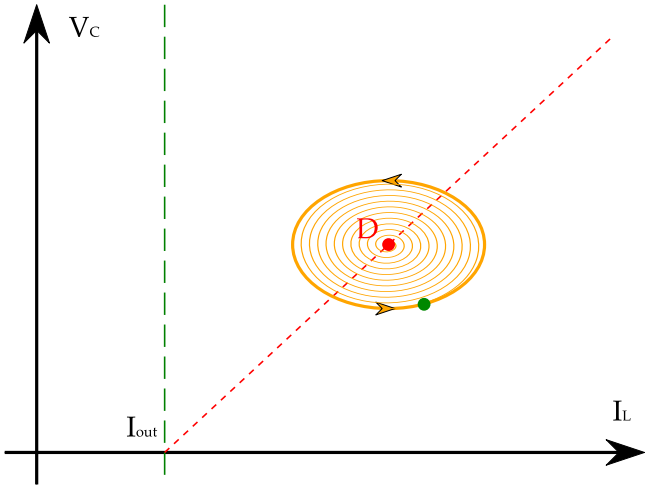

Figure 6.9: The trajectory in the I_L-V_C plane of the equations described in system 6.8 when maintaining a constant D. In a real system, ellipses will slowly decay to the steady-state point, and the steady states will not be on a straight line, because V_{in} decreases with increasing reaction rate in the fuel cell.

6.4.1 Oscillation Frequency

Assuming constant D and neglecting disturbances V_{in} and I_{out}, system 6.8 is essentially in the form:

$$\begin{cases} \dot{x} = a\,y \\ \dot{y} = -b\,x \end{cases} \qquad a, b \in \mathbb{R}^+ \tag{6.9}$$

In such a system, a point at coordinates (x, y), at distance $\|\mathbf{r}\| = \sqrt{x^2 + y^2}$ from the origin, moves along an elliptical trajectory described by:

$$\frac{a}{2}y^2 + \frac{b}{2}x^2 = c \qquad c \in \mathbb{R}_0^+ \tag{6.10}$$

Vector $\mathbf{t} = \frac{1}{\|\mathbf{r}\|}\begin{bmatrix} y & -x \end{bmatrix}$ is the unitary vector normal to $\mathbf{r}$. The area swept by the vector connecting the origin (the steady-state point) to a point on the trajectory, also known as areal velocity, is:

$$\mathbf{v} \cdot \mathbf{t} \cdot \frac{\|\mathbf{r}\|}{2} = \frac{a}{2}y^2 + \frac{b}{2}x^2 = c \tag{6.11}$$

This means that the areal velocity of a trajectory is constant and proportional to

its constant c. As the two semiaxes of an elliptical trajectory are $\sqrt{\frac{2c}{a}}$ and $\sqrt{\frac{2c}{b}}$, the area enclosed by a trajectory is:

$$A = \pi \frac{2c}{\sqrt{a\,b}} \tag{6.12}$$

Since both areal velocity and area are proportional to constant c, it follows that frequency is independent of it:

$$f = \frac{c}{A} = \frac{\sqrt{a\,b}}{2\pi} \tag{6.13}$$

Using the values for a and b of system 6.8, where $a = \frac{1-D}{C}$ and $b = \frac{1-D}{L}$, we then find that the system has a frequency, measured in rad/s, equal to:

$$\omega = \frac{1-D}{\sqrt{L\,C}} \tag{6.14}$$

We can therefore notice that a converter controlled with pulse-width modulation will exhibit lower oscillation frequencies at higher values of D. The oscillation frequency does not depend on any other variables.

6.5 Pulse-Width Modulation: $\mathcal{H}_\infty$ Linear Control

A first possible approach is linearising the set of dynamic equations 6.8 and synthesise a $\mathcal{H}_\infty$ controller for various linearisation points. As the properties of this nonlinear system change substantially, it is unlikely that a linear controller will function satisfactorily across a wide range of conditions, but use of gain scheduling may be applied.

$\mathcal{H}_\infty$ synthesis is a technique to synthesise a linear controller by solving an optimality problem in which the maximum magnitude of a certain transfer function, usually obtained by applying appropriate performance weights, is minimised. Details are available in textbooks such as the one of Skogestad and Postlethwaite [14].

Gain scheduling is a simple form of adaptive control [15] that modifies the currently used controller as a function of the value of some measured parameters. Its name notwithstanding, it can be used to change other controller properties than just its gain. It allows to join linear controllers designed for different conditions, but also implies the risk of cycles induced by the change of controller properties in some situations, and lacks rigorous mathematical tools to evaluate its performance.

6.5.1 Plant Linearisation and Controllability Analysis

We first add a small resistance R to system 6.8 to model the natural damping of oscillations, and the system becomes:

$$\begin{cases} L\,\dfrac{d\,I_L}{d\,t} = -V_C + (V_C + V_{in})\,D - R\,I_L \\ C\,\dfrac{d\,V_C}{d\,t} = I_L - I_{out} - I_L\,D \end{cases} \tag{6.15}$$

This system can be linearised around a steady-state point (D, I_L, V_{in})[3], using lowercase variables $(d, i_L, v_C, v_{in}, i_{out})$ for deviations from steady-state values, to obtain:

$$\begin{cases} L\,\dfrac{d\,i_L}{d\,t} = -v_C + D\,(v_C + v_{in}) + (V_C + V_{in})\,d - R\,i_L \\ C\,\dfrac{d\,v_C}{d\,t} = i_L - i_{out} - D\,i_L - I_L\,d \end{cases} \tag{6.16}$$

Transposing into the Laplace domain and eliminating state variable i_L, the following expression for the other state variable $v_C(s)$ can be obtained:

$$v_C = \frac{(1-D)\,D\,v_{in} + (L\,s + R)\,i_{out} + (-L\,I_L\,s + V_{in})\,d}{L\,C\,s^2 + C\,R\,s + (1-D)^2} \tag{6.17}$$

Some early remarks can be made about expression 6.17:

- All plant inputs (v_{in}, i_{out} and d) will be subject to two complex conjugate poles, with a variable time constant $\tau_p \approx \frac{1.73\,ms}{1-D}$ and damping $\zeta \approx \frac{0.011}{1-D}$; the positive value of R, however small, ensures that these poles are stable. When $D = 0$, the system is oscillatory with maximum natural frequency and minimum damping. Frequency reduces and damping increases with increasing D, until the system becomes an integrating one at $D = 1$.

- The gain of the transfer function between v_{in} and v_C has a different dependence on D than the other ones, being proportional to $\frac{D}{1-D}$ instead of $\frac{1}{(1-D)^2}$. At both extremes, $D = 0$ and $D = 1$, v_{in} has no effect on the output.

- Signal i_{out} has to pass through a left-hand-plane zero that, because of the relatively small value of R, can be close to derivative action (with our parameters,

[3]Only three variables need to be specified, as the other two are given by the steady-state form of system 6.15.

$z_{LHP} = -\frac{R}{L} \approx -3.19\,\text{s}$): rapid variations in i_{out} may therefore cause large oscillations in v_C. As both L and R are unchanging plant parameters, the location of this zero will not change during operation.

- Manipulated variable d has to pass through a right-half-plane zero ($z_{RHP} = \frac{V_{in}}{L\,I_L}$), which will limit the achievable performance. It is important that the position of d's positive zero and its gain are the only parts of expression 6.17 influenced by I_L and V_{in}, with all other dynamic properties being influenced by D alone. This RHP zero is highly variable during operation, and represents the main challenge for control.

Having obtained a linear representation of the plant at a generic linearisation point, it is possible to synthesise $\mathcal{H}_\infty$ controllers for different values of linearisation parameters (D, I_L, V_{in}), and look for patterns in how the optimal design changes with them.

We can notice this problem seems to be quite difficult: according to Skogestad and Postlethwaite [14], real RHP zeroes limit the achievable bandwidth to about half their value: with typical values $I_L = 200\,\text{A}$ and $V_{in} = 50\,\text{V}$, bandwidth will be limited to a maximum of about 130 rad/s. Yet, this value is much smaller than the natural undamped frequency of the system, which is 289 rad/s for $D = 0.5$, and reaches a maximum of 578 rad/s at $D = 0$: it will therefore be difficult to counteract the system's oscillations and reject the effect of disturbances for most of the range of D.

Controllability will improve with higher values of D, because of the slower oscillations and the larger damping. It will also improve with higher V_{in} or smaller I_L, since these will increase the value of z_{RHP} and, with it, of the maximum obtainable bandwidth.

6.5.2 Problem Formulation

$\mathcal{H}_\infty$ controller synthesis requires an appropriate formulation of the optimisation problem. We consider a mixed-sensitivity problem, in which performance weights are applied on the signals of the tracking error and of the manipulated variable.

Performance Weights

The weight $W_e(s)$ on the error signal e is used to set its control bandwidth. Its inverse $\frac{1}{|W_e|}$ will represent a limit to the magnitude of e at various frequencies. The bandwidth is set at the limit caused by the presence of the RHP zero in the manipulated variable's channel, $0.5\,z_{RHP}$:

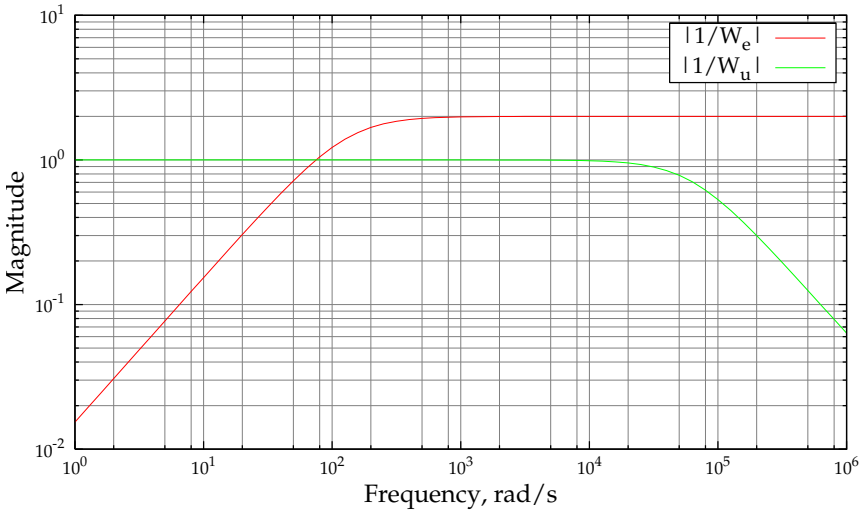

Figure 6.10: The absolute values of the inverses of the weights chosen for tracking error e and input usage u in $\mathcal{H}_\infty$ synthesis.

$$W_e(s) = \frac{0.5\,s + 0.5\,z_{RHP}}{s + 10^{-4} \times 0.5\,z_{RHP}} \tag{6.18}$$

The weight $W_u(s)$ on the input signal has to limit input usage to realistic values: in particular, the bandwidth cannot exceed the modulation frequency (the inverse of period T in figure 6.1). For our calculations we will assume $T \approx 0.1\,\text{ms}$, resulting in a usable bandwidth of up to $2\pi \times 10^4\,\text{rad/s}$.

$$W_u(s) = \frac{s + 2\pi \times 10^4}{0.01\,s + 2\pi \times 10^4} \tag{6.19}$$

The two weights, inverted, are pictured in the magnitude plot of figure 6.10: these lines are the "roofs" under which $\mathcal{H}_\infty$ synthesis will try to keep signals e and u of the plant (the assembly of converter and controller).

Plant Definition

Some variables require scaling. v_C is scaled to a nominal maximum of 200 V, v_{in} to 50 V[4], and i_{out} to 200 A. As d is always included in the range $[0, 1]$, it does not require scaling.

[4]We are assuming a stack of about 60 cells.

The $\mathcal{H}_\infty$ controller will take three inputs: the tracking error $e = v^{\text{ref}} - v_C$, representing the controller's feedback part, and two measurable plant disturbances, v_{in} and i_{out}, which represent the controller's feedforward parts. The controller's output will of course be the plant's only manipulated variable, d.

In actual operation D is known, since it is the manipulated variable and is set by the controller itself, so the controller will use $(1-D)\,D\,v_{in}$ as an input instead of just v_{in}, to filter out some dependency on D.

With the specified weights and scaling, the plant has now the following form:

$$P = \begin{bmatrix} -W_e\,G_v & -W_e\,G_i & W_e & -W_e\,G_d \\ 0 & 0 & 0 & W_u \\ -G_v & -G_i & 1 & -G_d \\ (1-D)\,D & 0 & 0 & 0 \\ 0 & 1 & 0 & 0 \end{bmatrix} \tag{6.20}$$

Where G_v, G_i and G_d are the scaled transfer functions to v_C from v_{in}, i_{out} and d respectively. The inputs of plant P are:

$$\begin{bmatrix} w & u \end{bmatrix}^T = \begin{bmatrix} v_{in} & i_{out} & r & d \end{bmatrix}^T \tag{6.21}$$

Its outputs are:

$$\begin{bmatrix} z & y \end{bmatrix}^T = \begin{bmatrix} W_e\,e & W_u\,d & e & (1-D)\,D\,v_{in} & i_{out} \end{bmatrix}^T \tag{6.22}$$

The first two components, the weighed signals, are the objective of minimisation, whereas the last three are the controller's inputs.

Controller Synthesis

Four series of syntheses have been carried out, starting from the linearisation point $D = 0.5$, $I_L = 200\,A$, $V_{in} = 50\,V$. In the first three, each parameter was varied independently; in the last one, I_L and V_{in} were changed together so that their ratio would remain unchanged, thereby affecting only the gain and not the position of the RHP zero.

The Bode plots for the $\mathcal{H}_\infty$ controller synthesised in the case of varying D is presented in figure 6.11. The other plots are collected in appendix B. From those plots, it is possible to notice some regular patterns:

- The optimisation algorithm tries to invert the two complex poles in the process with two complex zeroes in the feedback loop, that is in the transfer function between e and d. As D changes, these two zeroes will move correspondingly.

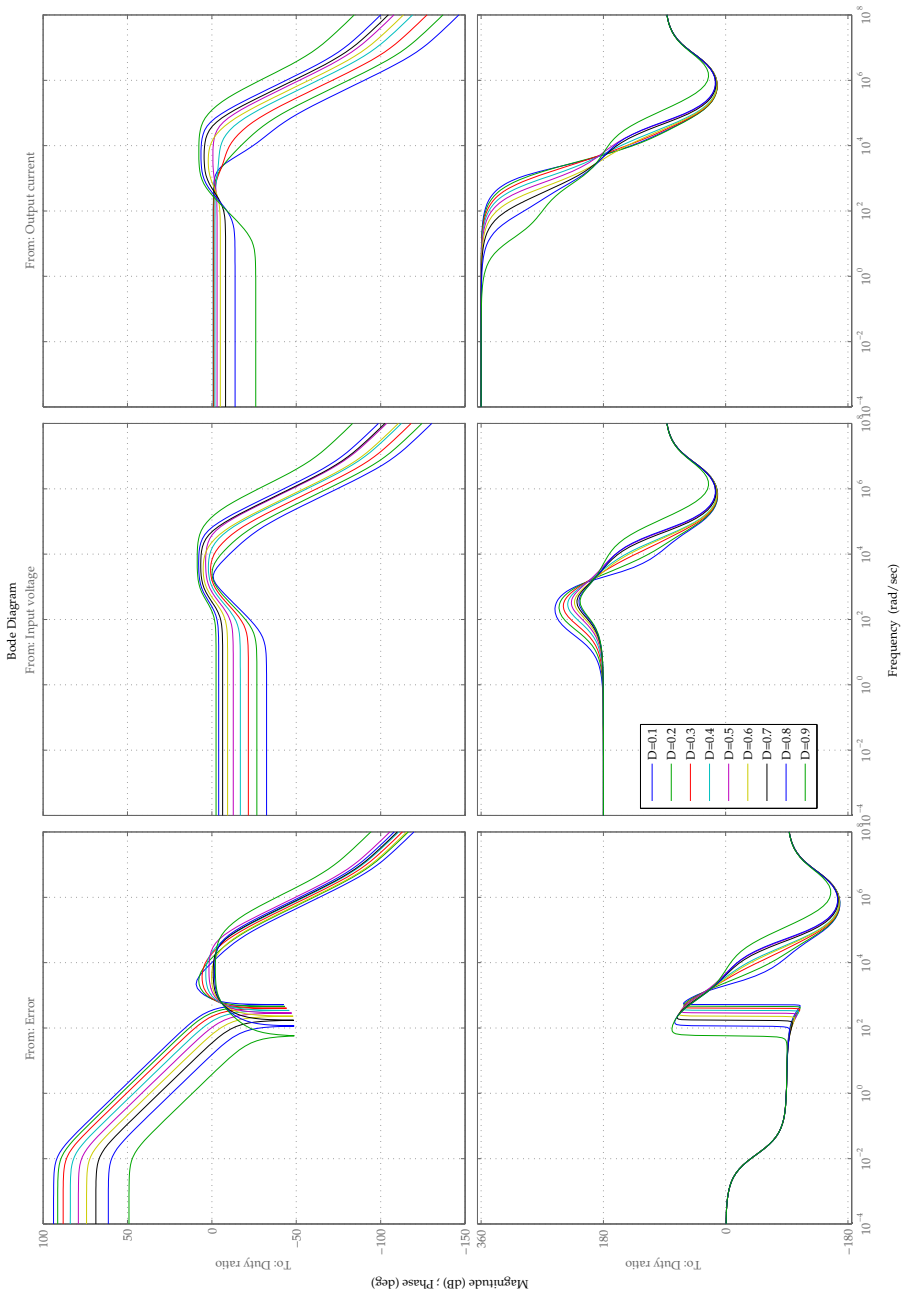

Figure 6.11: Bode plots for the $\mathcal{H}_\infty$ controller at various values of D, fixing I_L at 200 A and V_{in} at 50 V.

The optimisation algorithm's reason for this is to dampen the system's natural frequency in the feedback loop.

- At high frequencies, all transfer functions are subject to two left-hand-plane poles, whose locations on the frequency axis seems to be roughly coincident and constant at high frequencies, with some dependence on D and the $\frac{I_L}{V_{in}}$ ratio.
- Input voltage signal v_{in} is subject to a left-hand-plane zero occurring at frequencies lower than the two poles. Its position is influenced mainly by the $\frac{I_L}{V_{in}}$ ratio.
- Interestingly, the optimisation algorithm places a RHP zero on the output current's signal, which will cause an inverse response to appear in the controller. Its location on the frequency axis seems to be influenced chiefly by D and $\frac{I_L}{V_{in}}$.
- The gain for the error signal seems not to be influenced by I_L. At low frequencies, the large steady-state gain may indicate the opportunity of adding an integrator instead of a pole (an $\mathcal{H}_\infty$ synthesis algorithm cannot add an integrator by itself, as its $\mathcal{H}_\infty$ norm is infinite).
- The steady-state gain for channel v_{in} increases with D and decreases with I_L.
- The steady-state gain for i_{out}, instead, decreases with both D and V_{in}.

The step responses of v_C and d for various values of I_L and V_{in}, at constant D and location of z_{RHP}, are presented in figure 6.12. Other step responses for other conditions are presented in appendix B. From these plots, the following observations can be made:

- Low values of D tend to induce oscillations in the responses, especially the response to steps in reference.
- Steps in reference have very similar responses in v_C when the plant's RHP zero and D are constant (figure 6.12), confirming the RHP zero's importance in setting the control performance's limits. Furthermore, all plots indicate that there is an inverse response to a step in reference, however small; this is because feedback cannot eliminate RHP zeroes.

In conclusion, whereas some patterns have been identified in how optimal $\mathcal{H}_\infty$ controllers vary as a function of the chosen linearisation point, too many controller parameters change as a function of this point, and they do not suggest a simple and

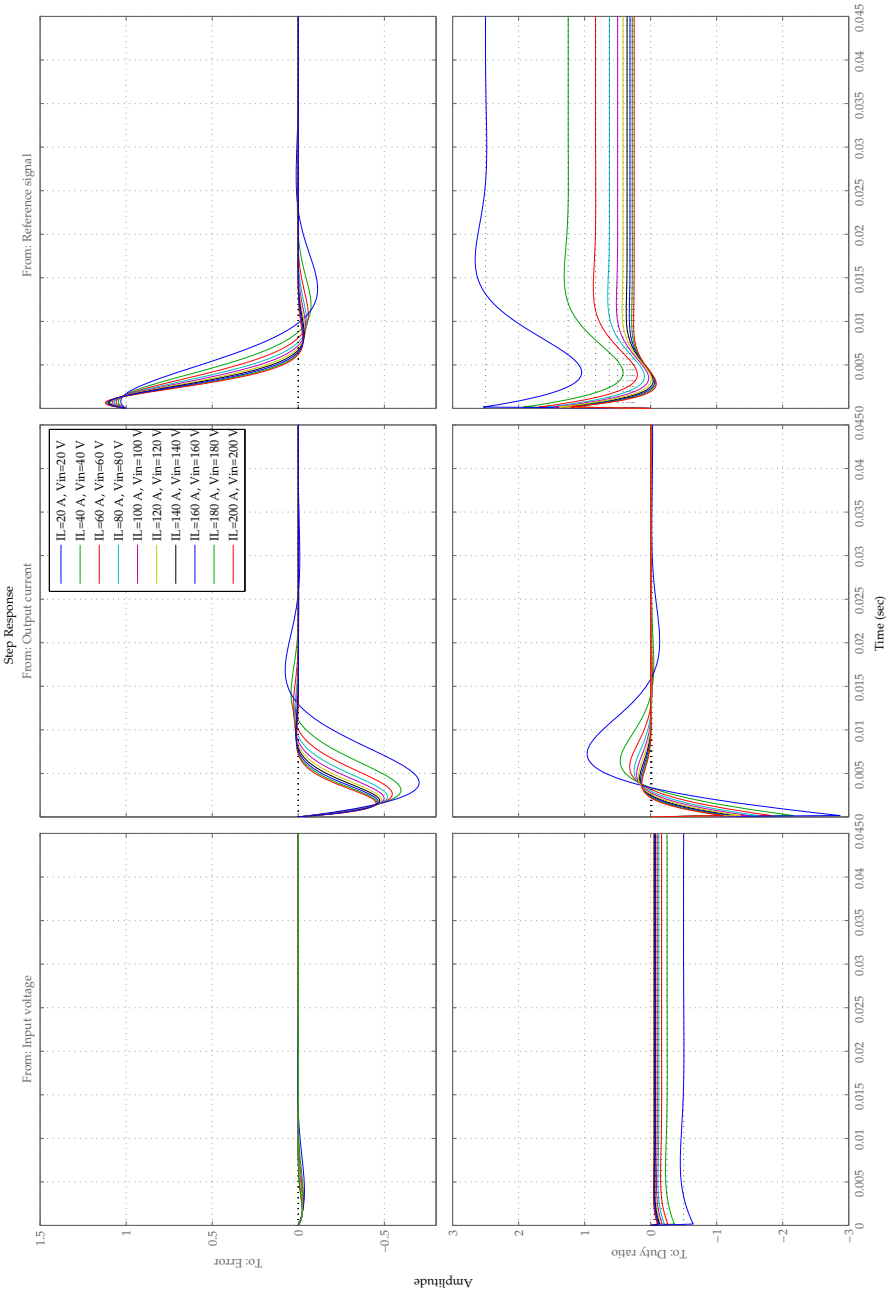

Figure 6.12: Step responses for the closed $\mathcal{H}_\infty$-controlled system at various values of I_L and V_{in}, fixing D at 0.5 and the ratio $\frac{I_L}{V_{in}}$ at 1 A/V.

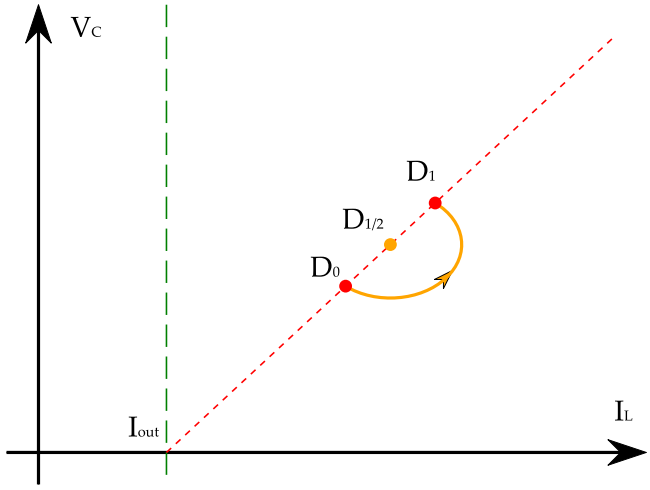

Figure 6.13: Feedforward control by filtering of input D.

obvious strategy to find a "good", almost $\mathcal{H}_\infty$-optimal controller when a linearisation point is given. A gain-scheduling approach would then have to implement a (possibly cumbersome) set of pre-calculated $\mathcal{H}_\infty$ controllers for all expected areas of operation.

6.6 Pulse-Width Modulation: Feedforward Control

If the converter is going to be used as an actuator in a larger feedback control loop, a simple control strategy for the inner loop is not to have any feedback control, and let the external feedback loop take care of disturbance rejection and precise reference tracking.

The simplest strategy to set the output voltage is to measure V_{in} and set D according to the steady-state equation:

$$D = \frac{V_C^{ref}}{V_C^{ref} + V_{in}} \tag{6.23}$$

However, the system's oscillations will take some time to decay. One alternative is adding a lag element, but this will reduce the converter's dynamic performance[5].

[5]Strictly speaking, left-hand plane poles do not pose fundamental limitations to control performance, but in this case the manipulable variable has a range of values limited to $[0, 1]$.

6.6.1 Half-Delay Filtering

We will consider the possibility of reducing oscillations by filtering the manipulated variable's signal in such a way as to minimise the oscillations induced by it. The idea is to split the signal of manipulated variable D in two parts, so that the second part counteracts the oscillations caused by the first.

Referring to figure 6.13, we consider a system at steady state with $D = D_0$. When a step from D_0 to D_1 is required by the reference signal, D is set to a "halfway" value $D_{1/2}$ for a time $\frac{\pi\sqrt{L\,C}}{1-D_{1/2}}$, exactly half the oscillation period, after which it is set to its final value D_1.

This input filter can be implemented with a partial delay: a fraction of the signal is delayed by a variable time (half the period of oscillations at $D = D_{1/2}$), while the other part is immediately sent to the output. The value of $D_{1/2}$ can be approximated by $(D_0 + D_1)/2$, but this will cause some residual oscillations when the distance between D_0 and D_1 is large. To obtain a more precise value, we first notice from figure 6.13 that the inductor current associated to duty ratio $D_{1/2}$ has to be halfway between $I_L(D_0)$ and $I_L(D_1)$. Therefore:

$$I_L(D_{1/2}) = I_{out}\frac{1}{1-D_{1/2}} = \frac{I_L(D_0)+I_L(D_1)}{2} = \frac{I_{out}}{2}\left(\frac{1}{1-D_0}+\frac{1}{1-D_1}\right) \tag{6.24}$$

It follows than $D_{1/2}$ can be calculated from D_0 and D_1 with the relationship:

$$\frac{1}{1-D_{1/2}} = \frac{1}{2}\left(\frac{1}{1-D_0}+\frac{1}{1-D_1}\right) \tag{6.25}$$

The resulting input filter is shown in figure 6.14. Given a reference V_C^{ref}, the value of $(1-D_1)^{-1}$ is calculated. The signal is then split in two parts, one going directly to the output and one passing through a delay. After addition, the resulting signal is converted from $(1-D)^{-1}$ into D. The time delay varies depending on the current value of the output.

A series of steps in the reference signal for output voltage has been simulated in figure 6.15. Input filtering significantly reduces the oscillations associated with the steps in reference. However, since the steady-state points are not located on a straight line (as simplified in figure 6.9 and 6.13), some oscillations remain. It has been found that adding a low-pass filter with time constant $\tau = \sqrt{L\,C}$ reduces these remaining oscillations, at the price of an only slight reduction in rise time (see line "Half delay, low pass" in figure 6.15).

The main drawbacks of this half-delay strategy are its sensitivity to variations in external current and the loss in phase caused by the delay. Since the half-delay

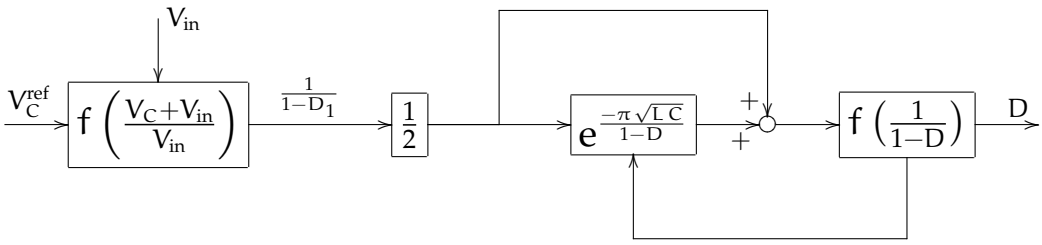

Figure 6.14: The half-delay input filter. The $f()$ elements represent nonlinearities.

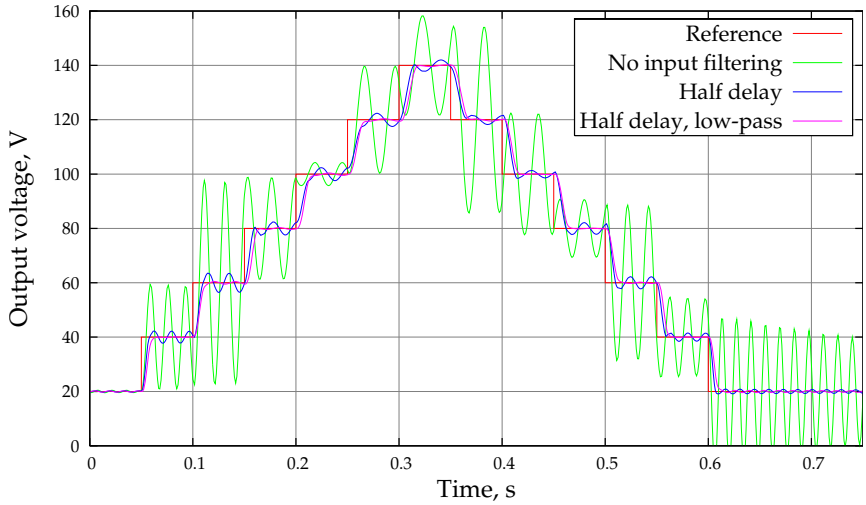

Figure 6.15: Simulation of a series of steps with feedforward control. No modelling error or disturbances are considered, and the external current is assumed constant at 20 A.

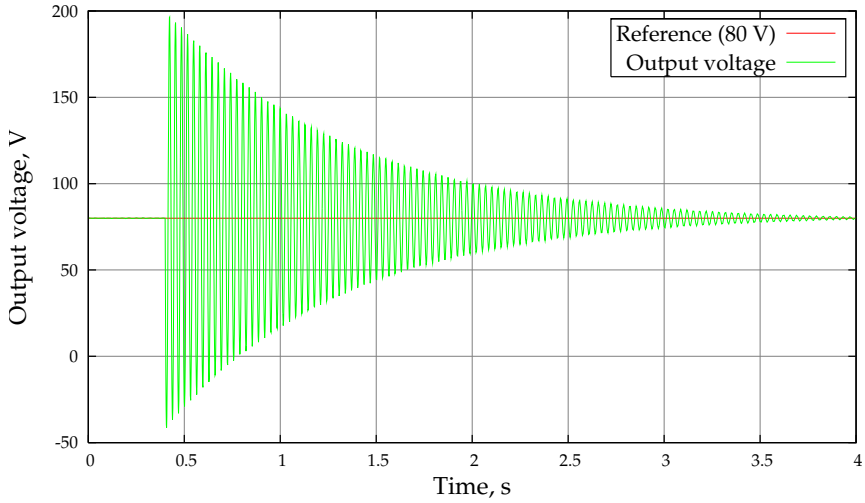

Figure 6.16: The oscillations induced by a step in external current, from 20 to 80 A, on a converter controlled by feedforward half-delay input filtering, with a set point of 80 V.

filter neither measures the external current nor has any internal form of feedback, variations in external current will induce oscillations that will be dampened only by the internal losses, as pictured in figure 6.16. The loss in phase caused by the presence of a delay in the filter may reduce the achievable performance when an external controller is designed using the converter as an actuator.

6.7 Pulse-Width Modulation: Input-Output Linearisation

In order to translate the nonlinear dynamics of buck-boost converters into a more manageable form, we will try to apply input-output linearisation to this problem. Input-output linearisation is a technique in which a system's variables are changed so that the system becomes linear in the transformed variables, and the problem becomes treatable by means of linear analysis and synthesis. The general theory is presented in most books about nonlinear control, such as Slotine and Li [16].

The nonlinear model of a buck-boost converter controlled by pulse-width modulation (6.8) is in the particular form $\dot{\mathbf{x}} = \mathbf{f}(\mathbf{x}) + \mathbf{g}(\mathbf{x})\,\mathrm{D}$, known as the *companion form*. This particular form allows the use of some common methods for input-output linearisation.

6.7.1 Change of Variables

We will adopt the following notation for the linearised system:

- μ is the linearised system's controlled variable;
- ν is the manipulated variable;
- ψ represents the internal (hidden) dynamics, independent from the manipulated variable ν and upon which μ does not depend.

Since we are interested in controlling V_C, it is trivial to set:

$$\mu = V_C \tag{6.26}$$

ν can then be chosen as:

$$\nu = \frac{I_L\,(1-D) - I_{out}}{C} \tag{6.27}$$

The rest of the model will be translated into the choice of variable ψ. In order to enforce the hypothesis that ψ does not depend on the manipulated variable, the Lie derivative of ψ along the direction identified by $\mathbf{g}(\mathbf{x})$ must be zero[6]. This amounts to:

$$\nabla\psi \cdot \mathbf{g}(\mathbf{x}) = \begin{bmatrix} \frac{\partial\psi}{\partial I_L} \\ \frac{\partial\psi}{\partial V_C} \end{bmatrix} \cdot \begin{bmatrix} \frac{V_C+V_{in}}{L} & \frac{-I_L}{C} \end{bmatrix} = 0 \tag{6.28}$$

This problem accepts the following solution:

$$\psi = \frac{1}{2}\,L\,I_L^2 + \frac{1}{2}\,C\,(V_C + V_{in})^2 \tag{6.29}$$

However, with this choice we lose information on the sign of I_L, which may change in some transients. For conversion purposes, we set $\xi = \mathrm{sgn}(I_L)$. The points identified by a certain value of ψ in the V_C-I_L plane are illustrated in figure 6.17. The inverse transformation of equations 6.26 and 6.29 is:

$$\begin{cases} V_C = \mu \\ I_L = \xi\sqrt{\dfrac{2\,\psi - C\,(\mu + V_{in})^2}{L}} \end{cases} \tag{6.30}$$

Since $\nabla\psi \cdot \mathbf{g}(\mathbf{x}) = 0$ by construction, the differential equation for ψ can be found by the relation:

[6] In other words, ψ must be such that ν cannot bring the system towards different values of ψ.

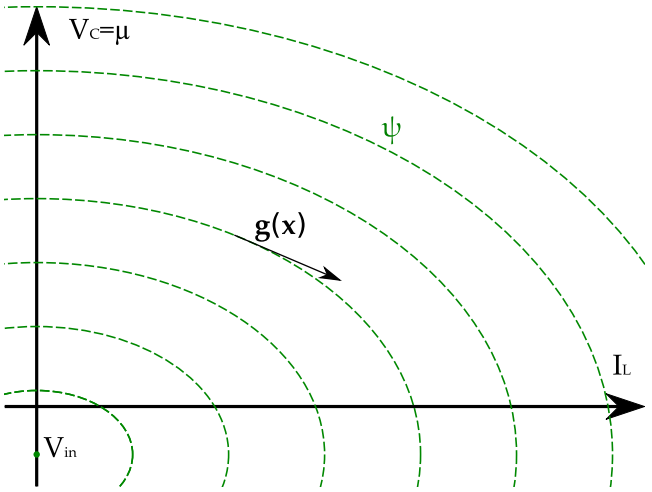

Figure 6.17: The ellipses describing the values of ψ in the V_C-I_L plane. Function $\mathbf{g}(\mathbf{x})$ is always tangent to the ellipses, and varying ν will not cause the operating point to move to a different value of ψ.

$$\begin{aligned}\dot{\psi} &= \nabla\psi \cdot \dot{\mathbf{x}} \triangleq \nabla\psi \cdot \mathbf{f}(\mathbf{x}) \\ &= -V_C\, I_L + (V_C + V_{in})\,(I_L - I_a) \\ &= V_{in}\, I_L - (\mu + V_{in})\, I_a\end{aligned} \tag{6.31}$$

The resulting system of differential equations expressed in the linearised variables is therefore:

$$\begin{cases} \dot{\psi} = V_{in}\,\xi\sqrt{\dfrac{2\,\psi - C\,(\mu + V_{in})^2}{L}} - (\mu + V_{in})\, I_{out} \\ \dot{\mu} = \nu \end{cases} \tag{6.32}$$

Only the second equation is actually linear, but it is also the only one that is of interest: ψ has no direct influence on the evolution of μ[7], which we can control by setting ν. However, before we decide to ignore ψ, we must check whether it is stable.

[7]This is not entirely true, since D is limited between 0 and 1: this means that ν will also be limited between $-I_{out}/C$ and $(I_L - I_{out})/C$, the latter bound ultimately depending on ψ.

6.7.2 Internal Dynamics

Unfortunately, the internal dynamics of the linearised system 6.32 is not stable. Naming $\dot{\psi} = w(\mu, \psi)$, we have:

$$\frac{\partial w(\psi, \mu)}{\partial \psi} = \frac{V_{in}\,\xi}{L\sqrt{\frac{2\psi - C\,(\mu + V_{in})^2}{L}}} = \frac{V_{in}}{L\,I_L} > 0 \qquad \text{for } I_L > 0 \tag{6.33}$$

The cause of this instability is the fact that, when ψ is increased at constant μ, the transient that is begun will bring the operating point to higher values of ψ. In the original system, a step in the input would have caused a spiral-shaped transient that would have eventually settled into the steady-state point; in the linearised system, since we use ν instead of D as a manipulated variable, we can easily control μ, but ψ is left to itself. Since ν depends on I_L, another possible interpretation is that we have introduced a destabilising feedback loop.

We can illustrate this problem and what it implies in the case of fuel cells by applying a simple proportional feedback controller in the form $\nu = K_c\,(V_C^{ref} - \mu)$ to a converter connected to a fuel-cell stack. Assuming that measurements on I_L and I_{out} are free of noise, bias or delay, μ will be stabilised around V_C^{ref} for every $K_c > 0$. However, according to equation 6.33, ψ will become unstable. When connected to a fuel cell, two scenarios are possible:

1. ψ falls to lower values, and stops only when I_L reaches the value of I_{out}. At this point, because of how ν was defined (6.27), $\dot{\mu} = \nu > 0$ would imply $D < 0$, which is beyond input saturation; D is left to zero as long as $V_C^{ref} > \mu$.

2. ψ rises to higher values, and stops only when I_L reaches the fuel cell's mass-transport limit and the stack produces almost no voltage. The converter will be able to deliver the required power, but the stack will be operating in a highly inefficient regime because of the high losses associated with operation at the mass-transport limit. Because of the low stack voltage, D will be very close to 1 in order to provide a much higher voltage to the converter output.

These two kinds of failure are illustrated in figure 6.18 and 6.19, using $K_c = 100\,\text{Hz}$ for the proportional controller. In this figure, two identical, consecutive series of steps in reference from 0 to 200 V and back are simulated. In the first cycle, ψ's instability makes it fall to lower values, and eventually results in D being set to zero (some residual oscillations can be observed from that point). The current through the fuel cell falls to zero and stack voltage tends to its open-circuit value.

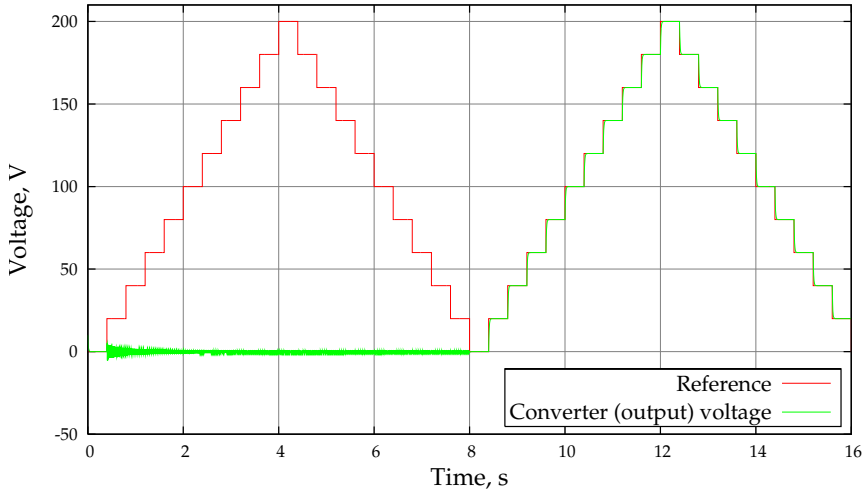

Figure 6.18: Illustration of failure with input-output linearisation. This plot shows a converter trying to follow a load without internal-dynamics stabilisation and with an external current of 30 A.

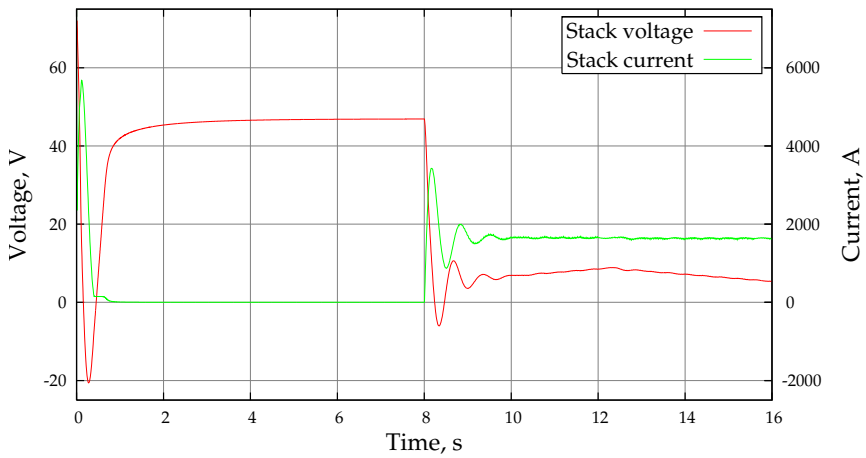

Figure 6.19: This plot shows the condition of the fuel-cell stack connected to the converter of figure 6.18. The stack's parameters are as in table 3.2, assuming a cell area of 0.5 m^2 and 60 cells.

When the reference returns to zero, D is "unlocked" as ψ falls, this time, on the side of higher values. Tracking proves to be excellent[8], yet, as figure 6.19 shows, the stack's voltage and current indicate that the stack is operating at the mass-transport limit: at times when higher power is required by the converter, the stack voltage goes up to match the power demand: we would expect it to go down because of increased reactant consumption.

Whereas a fuel-cell stack may deliver power through a converter in these conditions, it is hardly an efficient way: in particular, this layout features maximum consumption at zero power delivery, all power being used to overcome the diffusion-induced overvoltage.

It should be remarked that there is an important role of numerical noise in determining whether ψ will go to the side of high or low values. Figures 6.18 and 6.19 could therefore not be exactly reproduced when simulated with slightly different parameters or even just on different operating systems.

In fact, this approach could in principle not have worked as originally intended, as controlling an integrator process with proportional feedback allows perfect control when the proportionality constant of the controller tends to infinity, but perfect control is theoretically impossible in non-minimum-phase systems. This example clearly indicates the need to stabilise the internal dynamics of the linearised system in order to properly control the reaction rate in the fuel cell.

6.7.3 Stabilisation of the Internal Dynamics

Stabilising the internal dynamics of non-minimum-phase nonlinear systems is an active field of current research, and there are no general methods to guarantee certain performance requirements on feedback control. In general, however, stabilising the internal dynamics means to constrain μ to be a function of ψ so that the total derivative of $w(\psi, \mu)$ is kept negative:

$$\frac{\mathrm{d}\, w(\psi,\mu)}{\mathrm{d}\,\psi} = \frac{\partial w(\psi,\mu)}{\partial \psi} + \frac{\partial w(\psi,\mu)}{\partial \mu}\frac{\mathrm{d}\,\mu}{\mathrm{d}\,\psi} < 0 \tag{6.34}$$

Enforcing this condition will reduce oscillations in the V_C-I_L phase plane, as trajectories close to the steady-state value of ψ will be attracted by it. If the control algorithm $\nu(\mu, \psi)$ can be chosen so that $\frac{\mathrm{d}\,\nu}{\mathrm{d}\,\mu} < 0$ as well, oscillations will be eliminated as both state variables will converge to the steady state.

Since the second partial-derivative term in equation 6.34 is:

[8] To be fair, we did not model any error in calculations or measurement, so perfect control could be obtained just by applying an infinite gain.

$$\frac{\partial w(\psi,\mu)}{\partial \mu} = -\frac{C\,(\mu + V_{in})\,V_{in}\,\xi}{L\sqrt{\frac{2\,\psi - C\,(\mu+V_{in})^2}{L}}} - I_{out} = -\frac{C\,(\mu + V_{in})\,V_{in}}{L\,I_L} - I_{out} \tag{6.35}$$

We can reformulate condition 6.34 as:

$$\frac{V_{in}}{L\,I_L} - \left(\frac{C(\mu + V_{in})\,V_{in}}{L\,I_L} + I_{out}\right)\frac{d\,\mu}{d\,\psi} < 0 \tag{6.36}$$

Manipulating this expression, the condition on the dependence of μ from ψ becomes:

$$\frac{d\,\mu}{d\,\psi} > \frac{V_{in}}{C\,(\mu + V_{in})\,V_{in} + L\,I_L\,I_{out}} \tag{6.37}$$

However, μ is determined by ν in the linearised system 6.32. As ν is our manipulated variable, it makes sense to translate this condition in terms of ν:

$$\nu = \dot{\mu} = \frac{d\,\mu}{d\,\psi}\,\dot{\psi} \tag{6.38}$$

$$\nu\,\mathrm{sgn}(\dot{\psi}) > \frac{V_{in}\,|\dot{\psi}|}{C\,(\mu + V_{in})\,V_{in} + L\,I_L\,I_{out}} \tag{6.39}$$

We have therefore translated the stabilisation of ψ into a requirement on the values that ν can have. At steady state there is no requirement, as $\dot{\psi} = 0$ by definition of steady state. During transients, ν must have the same sign as $\dot{\psi}$ and must be larger, in absolute value, than a certain lower limit.

6.7.4 Feedback with Input Bounds

Having obtained a bound on ν as a function of measurable quantities (the input and output currents and voltages), it seems natural to devise a simple feedback control law for μ (possibly a high-gain proportional controller) and filter the input ν through bound 6.39, to avoid instability. However, this approach runs rapidly into problems.

When a simulation is started from a non-steady-state point, the bound on ν forces the operating point to $\mu = 0$, $I_L = I_{out}$; oscillations are induced by the saturation constraint $D \in [0, 1]$, which the required bound on ν tries to violate. Transients end invariably with the controller requiring $D < 0$, with the fuel cell being cut off from the converter.

The reason for this failure can ultimately be traced to the fact that this system cannot completely eliminate oscillations, as observed by means of linear controllability analysis in section 6.5.1: if condition 6.39 could be enforced strictly, we would have achieved what it was already demonstrated to be impossible.

6.7.5 Feedforward with Internal Oscillation Dampening

As feedback proved problematic with this non-minimum-phase nonlinear system, another approach was attempted: on one hand, an unfiltered value D_0 is calculated from reference V_C^{ref} and the measurement V_{in}, as in equation 6.23. This is used to compute a corresponding ν_0 with equation 6.27. Then, this value is added to a ν_ψ, obtained from bound 6.39, that has the function of dampening the oscillations:

$$\nu_\psi = \frac{V_{\text{in}}\,\dot{\psi}}{C\,(\mu + V_{\text{in}})\,V_{\text{in}} + L\,I_L\,I_{\text{out}}} \tag{6.40}$$

The final D passed to the converter is then obtained inverting equation 6.27 for $\nu = \nu_D + \nu_\psi$. Since the conversion function is linear in ν, it is possible to separate the two terms:

$$D = 1 - \frac{I_{\text{out}} + C\,(\nu_0 + \nu_\psi)}{I_L} = D_0 - C\,\frac{\nu_\psi}{I_L} \tag{6.41}$$

This approach allows for a certain amount of oscillations, since the final ν is not strictly bounded by equation 6.39, which acts here as a dampening element. Performance is not very good with very low values of I_{out}, where dynamics are slower. Operation at low values of I_{out} is however inherently difficult with any approach, as I_{out} is the only term that can reduce the value of V_C in its differential equation.

A series of steps in reference is shown in figure 6.20, where it can be seen that transients at the highest voltages are somewhat slower, as should be expected from equation 6.14, which expresses that a converter's natural oscillation frequency is lower for high values of D; overall performance is however satisfactory, and the fuel-cell stack does not operate at the mass-transport barrier, but at lower currents, yielding higher efficiency. As this is a feedforward technique, there is some steady-state offset caused by losses in the converter, which may be evened out by an external feedback loop that could use the converter as an actuator. Oscillation dampening is excellent, as shown in figure 6.21: compared to figure 6.16, the transient is shortened by two orders of magnitude.

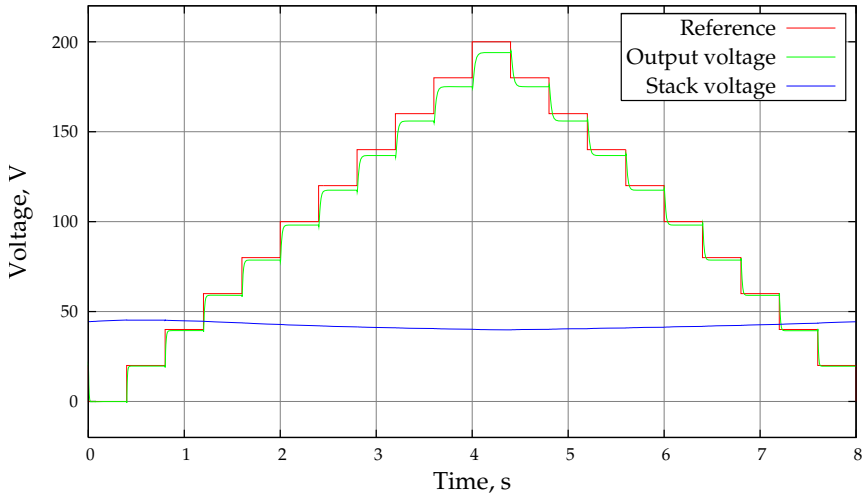

Figure 6.20: Input-output linearisation using feedforward: a series of steps in reference performed on a converter connected to a fuel-cell stack, as done before in figure 6.18, with internal oscillation dampening. The reference pattern and stack parameters are the same.

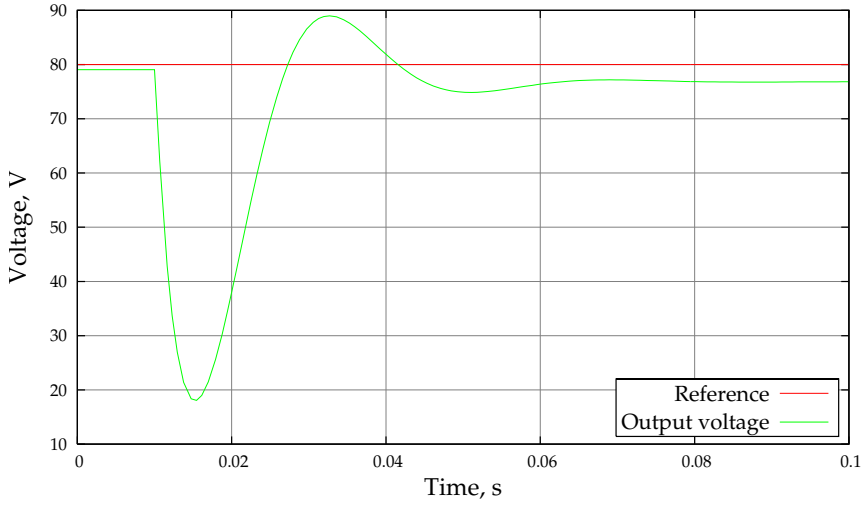

Figure 6.21: Reaction to a step in external current from 20 to 80 A with a constant reference of 80 V for a converter connected to a fuel-cell stack with internal oscillation dampening, as in figure 6.16 (note the different time scale).

6.8 Switching Rules

We will now attempt a different approach to the problem of controlling a buck-boost converter. We will try to devise a set of logical rules to determine when the switch should be in the ON or OFF position, instead of using the duty ratio as a continuous input variable.

This section will try an approach similar to sliding-mode control by defining some *switching rules*. Instead of the usual constant sliding surfaces as described by Spiazzi and Mattavelli [2], a series of variable surfaces were devised to take advantage of the shape of trajectories of the system in the V_C-I_L plane. This is helpful, as their shape can change considerably depending on external disturbances (such as I_{out} and V_{in}), which represent the effect of having a variable voltage source and an unknown load. This is strictly speaking not sliding-mode control, as in fact no one of the defined surfaces will actually be a sliding mode. The rules, however, do make sure that the desired output is attained.

The equations describing our system are, when the fuel-cell stack is connected to the inductor (the ON position in figure 6.4):

$$\begin{cases} L \dfrac{d\, I_L}{d\, t} = V_{in} \\ C \dfrac{d\, V_C}{d\, t} = -I_{out} \end{cases} \tag{6.42}$$

V_{in} and I_{out} are considered to be external entities with respect to the converter, and are assumed to maintain a positive sign. The trajectories described by these equations are straight lines, since I_{out} and V_{in} are assumed not to depend directly on I_L or V_C.

When the switch is positioned so that the inductor is connected to the capacitor (the OFF position in figure 6.4), the equations are instead:

$$\begin{cases} L \dfrac{d\, I_L}{d\, t} = -V_C \\ C \dfrac{d\, V_C}{d\, t} = I_L - I_{out} \end{cases} \tag{6.43}$$

The trajectories described by these equations are a series of ellipses, centered at the point $(0,\ I_{out})$, whose parametric equation can be given as:

$$\frac{1}{2} L\, (I_L - I_{out})^2 + \frac{1}{2} C\, V_C^2 = c \qquad c \in \mathbb{R}_0^+ \tag{6.44}$$

Obviously, if I_{out} were to change during the transient, the centre of the ellipses would move and the actual trajectory of a point could not resemble an ellipse at all.

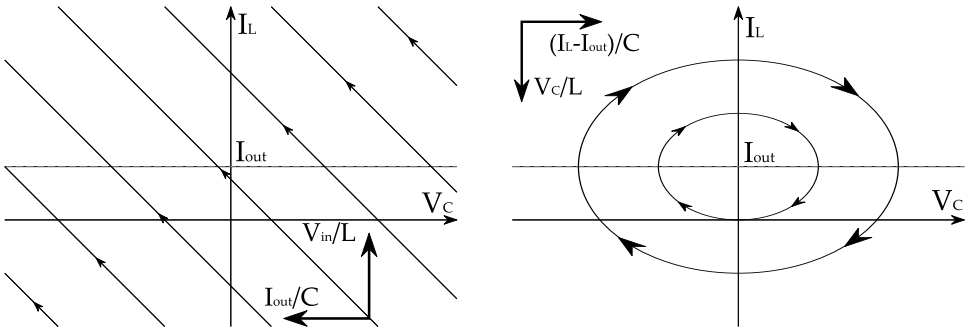

Figure 6.22: The trajectories of the state variables in a buck-boost converter in the V_C-I_L plane for given values of external disturbances V_{in}, I_{out}.

It would be tempting to define these curves as representatives of the amount of energy physically stored in the converter, but the first term in equation 6.44 is not the energy stored in the inductor's magnetic field. The value of c, however, can indeed be mathematically interpreted as representative of the system's energy, if not physically.

The trajectories corresponding to these equations are shown in figure 6.22. The ON mode is represented on the left-hand side, where energy is collected from the input by the inductor. On the right-hand side (the OFF mode), no energy is drawn from the source, and the energy stored in the inductor is exchanged with the capacitor. The capacitor exchanges power with the output in both configurations. In a real system, the trajectories on the right-hand side would be spirals, because of losses in the switches.

6.8.1 Control Rules

The objective of the switching rules is to maintain a certain value of the converter's output voltage by switching the system between its two substructures, as shown in figures 6.4 and 6.22, accounting for the changes in output current, caused by the load, and in input voltage, caused by the fuel-cell stack. The rules will have to be calculated at each iteration, using new measurements for V_{in}, I_L, V_C and I_{out}, and are formulated as follows:

Energy level If the value of c in equation 6.44 is not sufficiently high, the elliptical trajectories of the OFF mode will not be able to reach V_C^{ref}. Therefore, the only possibility left is to switch to the linear trajectories of the ON mode until a sufficiently high energy level is reached. It will then be possible to switch to

the OFF mode and reach V_C^{ref}.

The "sufficiently high" energy level is however not the one corresponding to an ellipse of the OFF mode that has its extreme point in V_C^{ref}. If it were so, it would not be possible to maintain the operating point at that value by switching back to the ON mode: the ON mode, which in general has a non-zero component along the V_C axis, would cause the system to fall to a lower energy level, at which it should maintain the ON state until reaching again a high enough energy level. An hysteresis cycle would then result, which would yield an unsatisfactory performance.

The correct energy level is therefore the one corresponding to the ellipse that, at the reference voltage V_C^{ref}, is *tangent* to the lines of the ON mode. The unavoidable imprecision in parameter estimation and measurement will cause some oscillation, however.

The mathematical formulation of the rule is:

$$\frac{1}{2} C V_C^2 + \frac{1}{2} L (I_L - I_{out})^2 < \frac{1}{2} C V_C^{ref2} + \frac{1}{2} L \left(\frac{V_C^{ref} I_{out}}{V_{in}} \right)^2 \Rightarrow \mathsf{ON} \qquad (6.45)$$

High-voltage switch At voltages higher that V_C^{ref}, the surface at which one moves from one substructure to the other is given by the tangent line departing from the ellipse described above at voltage V_C^{ref}. Since this line is by construction parallel to the lines of the ON mode, once the operating point crosses this line arriving from an elliptical trajectory of the OFF mode, it is not possible for it to return back. This is important because there is no guarantee that the component of the ON-mode derivatives along a given line are larger than the OFF-mode's, because the former are disturbances that we do not directly control.

The mathematical formulation of the rule is:

$$V_C > V_C^{ref} \quad \wedge \quad I_L - I_{out} < \frac{V_C^{ref} I_{out}}{V_{in}} - \frac{C}{L} \frac{V_{in}}{I_{out}} \left(V_C - V_C^{ref} \right) \Rightarrow \mathsf{ON} \qquad (6.46)$$

Low-voltage switch It is not unlikely that, during transients, voltage V_C will reach negative values. In fact, it is quite a common phenomenon in transients, even if it lasts only for a short time. A reasonable control objective is to minimise the inverse response during such a transient. Therefore, if during a transient V_C is less than zero, and the energy level is sufficient as defined above, the

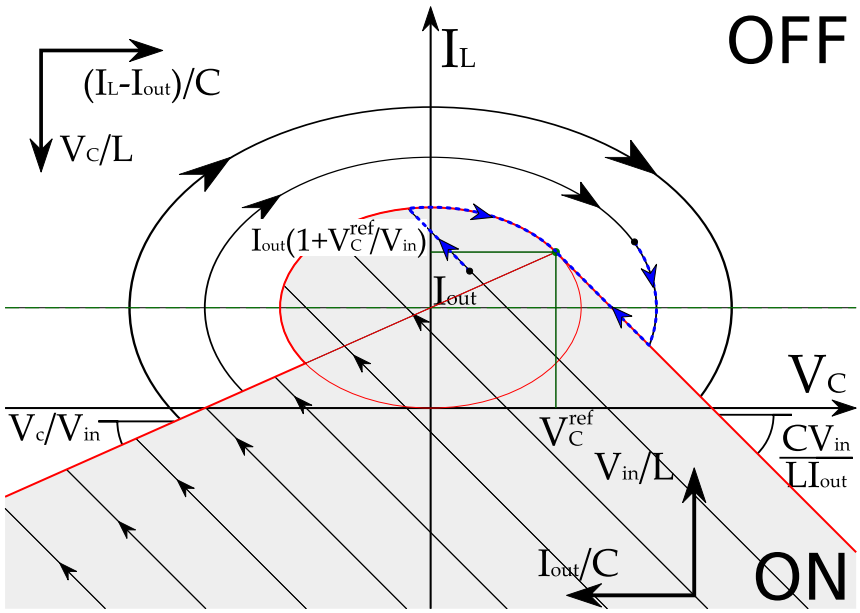

Figure 6.23: Graphical representation of the switching rules to control a buck-boost converter. Two possible trajectories, from higher and lower values of V_C to reach V_C^{ref}, are sketched in blue.

switch from ON mode to OFF mode should be at the point where the ON lines are tangent to an ellipse, which is the lowest-energy point they will reach.

The mathematical formulation of the rule is:

$$V_C < 0 \quad \wedge \quad I_L - I_{out} < \frac{V_C\, I_{out}}{V_{in}} \Rightarrow \text{ON} \tag{6.47}$$

Combining the rules The three rules are graphically plotted in figure 6.23: notice that the inclination of the ON lines (in the greyed-out area), the inclination of the switching surface (in red) at high and low voltage, and the size and vertical positioning of the central elliptical part, all these depend on the values of the reference voltage and the disturbances. If no rule should match, the default state of the switch will be OFF; the Simulink implementation of the rules is shown in figure 6.24.

6.8.2 Performance of the Switching Rules

Some useful facts can be observed just by looking carefully at figure 6.23.

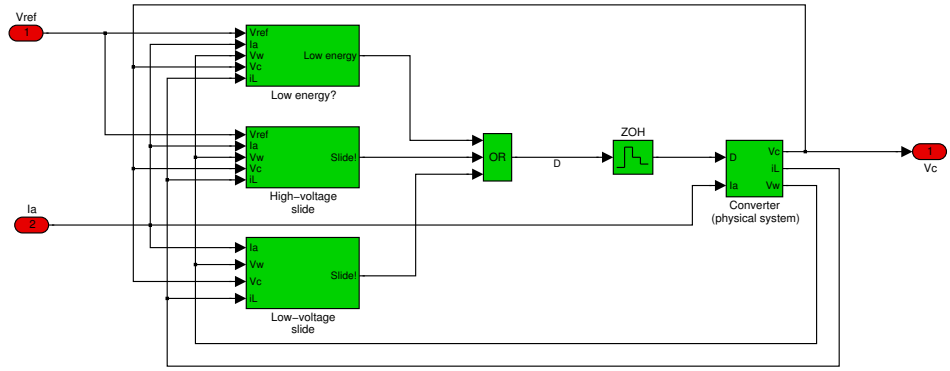

Figure 6.24: The Simulink implementation of the switching rules. The rules' result is passed through a zero-order hold element (ZOH), whose time parameter sets the switching frequency. The zero-order hold's output is then passed to a block modelling the converter.

- Steps in V_C^{ref} will in general exhibit an inverse response. When V_C^{ref} has to increase, the operating point has to accumulate enough energy along the ON-mode lines, which will cause an initial reduction of V_C. When V_C^{ref} has to decrease, the operating point first follows the OFF-mode elliptical trajectories until it reaches either their maximum value of voltage, or the switching surface described by rule 6.46, before decreasing again.

- Steps in I_{out} will have a similar effect, but this is intuitive: more current at the output, at the same output voltage, means more power delivered, and the converter will have to gradually adapt to this new regime.

- The set of rules does not permit to specify a negative V_C^{ref}. This is intentional, because, with a positive I_{out}, power would be drawn from the outer circuit to the fuel cell, causing reverse electrolysis, and likely damaging the fuel cell's catalyst.

A simulated transient is shown in figure 6.25. It can be noticed how the inverse response is much more significant at high values of I_{out}. The transients have fast settling times, about 5 ms: this is faster than the 0.2 s required for vehicles (according to Soroush and Elabd [17]), and can make this control strategy useful also for microelectronic applications such as laptops and mobile phones. It can also be noticed how the output becomes more noisy at high values of I_{out}.

A problem may arise when the converter is required to produce exactly 0 volts, even if I_{out} is larger than 0. The converter's switching rules degenerate in a special

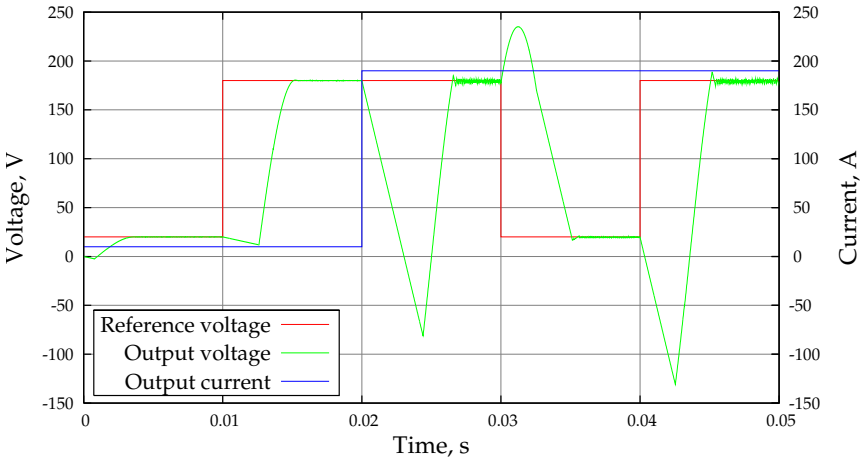

Figure 6.25: Simulated transient of a buck-boost converter, controlled with switching rules. The switching frequency has been set to 10 µs.

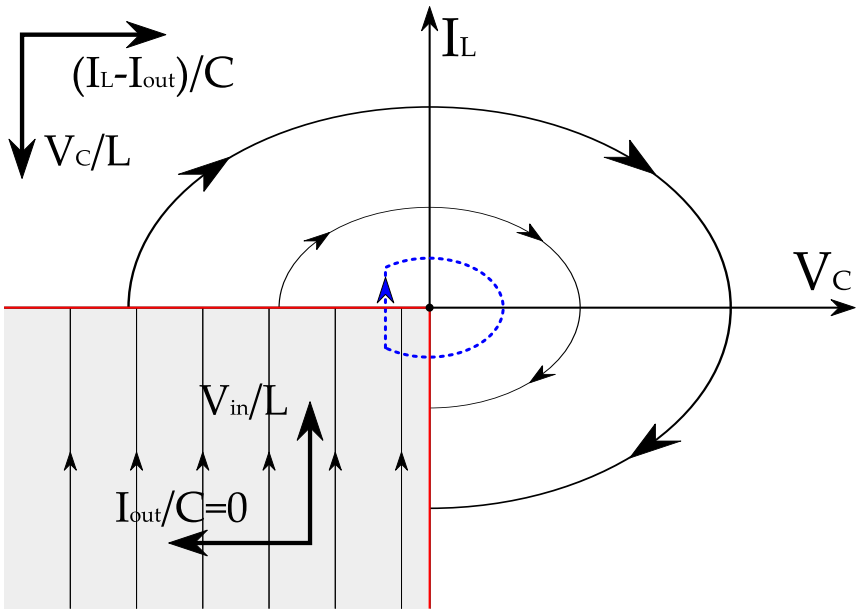

Figure 6.26: The approximate trajectory of the operating point when $V_C^{ref} = 0$ and $I_{out} = 0$. Higher switching frequencies will shrink the trajectory towards the origin.

case: output voltage oscillates around the origin in an asymmetrical fashion, as sketched in figure 6.26, resulting in a net average positive value of V_C and possibly wind-up issues in the outer control loop. While the amplitude of such oscillations can be reduced with a higher switching frequency, their average value will always be positive.

To address this issue, a new simple rule for the converter can be added:

$$V_C^{\text{ref}} \leqslant 0 \Rightarrow \mathsf{OFF} \tag{6.48}$$

It is important to notice that rule 6.48 takes precedence on all others, since it might be contradicting them. The meaning of this rule is that the fuel-cell stack must be disconnected whenever there is an unachievably low objective. In an actual application, the voltage will then gradually decrease to zero because of dissipation in external load and in the converter switches.

6.8.3 Computational Performance

The simulation times of this controller are relatively long; the transient in figure 6.25 requires about 50 seconds to calculate on a 2-GHz, 32-bit desktop computer running Simulink. This makes simulation over longer time spans unpractical. The fuel cell's overvoltage, when starting the simulation, needs some time to reach a steady-state value from zero, and this initialisation transient may interfere with the transients we are interested in measuring. In practice, using this method to study how the fuel cell reacts to control is not computationally convenient.

The main reason for such an unsatisfactory computational efficiency is that the rules are evaluated every 10 µs (in the case of figure 6.25), and a transient has to be calculated every time the algorithm requires a switch. When the transients settle[9], the manipulated variable does not attain a constant value, but is continuously switched between ON and OFF. Integration algorithms for stiff systems do not provide any sensible improvement.

Implementing this control algorithm would likely imply building a dedicated circuit to simulate the switching rules, which only require basic arithmetic and logical operations: indeed, the actual determination of whether the switch should be ON or OFF is a small part of the computational cost. However, the numerical simulation of the converter's transients with this control strategy is computationally very expensive, as every switching cycle implies a sudden change in the model's equations.

[9] In reality, only *macroscopic* transients settle, because the control algorithm is in fact based on rapidly switching between two transients compensating each other.

Using the model based on pulse-width modulation, which uses a continuous manipulated variable, improves the simulation performance, even though the control performance is inferior because of the additional level of abstraction.

6.9 Conclusions

Some insight about control of fuel-cell power output can be obtained from the various approaches analysed in this chapter. The main control issue are the nonlinear, non-minimum-phase dynamics of the buck-boost converter.

Controlling DC motors, a likely appliance for fuel-cell power generation, is usually done by manipulating the input voltage to the motor. Therefore, the control problem for the converter was defined as to deliver a certain output voltage in spite of external disturbances, such as input voltage (changing because of variations in the stack voltage) and output current (changing because of variations in motor conditions, such as angular velocity).

First, a model based on pulse-width modulation was presented. A local linearisation around a generic steady state was performed to attempt an $\mathcal{H}_\infty$ controller synthesis. The manipulated input (the duty ratio) was proven to be subject to a RHP zero, which is strongly dependent on the linearisation point: this poses inherent limitations to control performance. Disturbance rejection is influenced by the position of the RHP zero, but also by the duty ratio at the linearisation point.

A simple feedforward control strategy has then been attempted, resulting in good tracking qualities. However, this approach resulted in high sensitivity to disturbances because of the low power dissipation in the converter. Input-output linearisation was then attempted, proving that the model of the system with pulse-width modulation is non-minimum-phase in the nonlinear sense as well, and requires some sort of stabilisation of the internal dynamics. A feedforward approach coupled with an oscillation-dampening component (in itself a form of feedback) gave satisfactory results in both tracking and oscillation dampening.

Finally, a method based on the evaluation of switching rules has been proposed, and has yielded very good results, with settling times of about 5 ms. This method may in practice be realised with relatively simple hardware, as it does not imply more than a few arithmetic and logical operations. However, it is more difficult to rigorously evaluate the robustness of this method to uncertain or lagging measurements. This method also unsuitable for computer simulations beyond the scale of a few seconds: this means it is difficult to simulate a fuel cell's operation under this type of control.

Bibliography

[1] Michael Giesselmann, Hossein Salehfar, Hamid A. Toliyat, and Tahmid Ur Rahman. *The Power Electronics Handbook*, chapter 7 - Modulation Strategies. Industrial electronics. CRC press, 2001.

[2] Giorgio Spiazzi and Paolo Mattavelli. *The Power Electronics Handbook*, chapter 8 - Sliding-Mode Control of Switched-Mode Power Supplies. Industrial electronics. CRC press, 2001.

[3] Jai P. Agrawal. *Power Electronic Systems — Theory and Design*. Prentice Hall, 2001.

[4] T. Geyer, G. Papafotiou, and M. Morari. On the optimal control of switch-mode DC-DC converters. *Hybrid Systems: Computation and Control*, 2993:342–356, March 2004. URL `http://control.ee.ethz.ch/index.cgi?page=publications;action=details;id=31`.

[5] Manfred Morari. Beyond process control. In *Proceedings of the 13th Nordic Process Control Workshop, Lyngby, Denmark*, 2006.

[6] Rami Naim, George Weiss, and Shmuel Ben-Yaakov. H^∞ control applied to boost power converters. *Transactions on Power Electronics*, 12(4):677–683, July 1997.

[7] Fang Lin Luo and Hong Ye. *Advanced DC/DC Converters*. CRC press, Boca Raton, Florida, USA, 2004.

[8] S. Caux, J. Lachaize, M. Fadel, P. Shott, and L. Nicod. Modelling and control of a fuel cell system and storage elements in transport applications. *Journal of Process Control*, 15:481–491, 2005.

[9] Sébastien E. Gay and Mehrdad Ehsani. Impact of electric motor field-weakening on drive train oscillations. In *Electric Machines and Drives Conference*, volume 2, pages 641–646, June 2003.

[10] Werner Leonhard. *Control of Electrical Drives*. Springer, 2nd edition, 2001.

[11] James Larminie and John Lowry. *Electric Vehicle Technology Explained*. Wiley, 2003.

[12] Chee-Mun Ong. *Dynamic Simulation of Electric Machinery*. Prentice Hall, 1998.

[13] C. L. Chu, M. C. Tsai, and H. Y. Chen. Torque control of brushless DC motors applied to electric vehicles. In *Electric Machines and Drives Conference*, pages 82–87, 2001.

[14] Sigurd Skogestad and Ian Postlethwaite. *Multivariable feedback control*. Wiley, 2nd edition, 2005.

[15] Karl Johan Åström and Björn Wittenmark. *Adaptive Control*. Addison Wesley, 1989.

[16] Jean-Jacques E. Slotine and Weiping Li. *Applied Nonlinear Control*. Prentice-Hall, 1991.

[17] Masoud Soroush and Yossef A. Elabd. Process systems engineering challenges in fuel cell technology for automobiles. In *AIChE Annual Meeting*, 2004.

Chapter 7

Composition and Temperature Control

Having considered the control of the reaction rate in chapter 6, we turn our attention to the control of the conditions that allow the reaction to proceed, namely reactant concentration and stack temperature.

As outlined in chapter 5, we consider a stack of PBI-membrane PEM fuel cells, fed on pure hydrogen on the anodic side and air (possibly after combustion of some hydrogen to heat up the cell) on the cathodic side (such as in figure 5.4 on page 78).

As we are considering a stack of cells whose flows are connected in parallel through manifolds, all cells will receive flows at stack-entrance conditions: it is therefore possible to consider only one cell as representative of the conditions of all the cells in the whole stack. The three main control issues are then:

1. Control of hydrogen pressure in the anode;
2. Control of oxygen bulk concentration in the cathode;
3. Control of temperature in the cell (anode and cathode are assumed to have the same temperature).

However, for these three tasks we assume that we only have two manipulated variables, which are the entering flows of hydrogen on the anode side and air on the cathode side. Thus, the control strategy proposed in this chapter presents the novelty of not having a dedicated cooling system to control temperature: temperature will be controlled by means of the air flow.

This will however cause a certain degree of interference between the control of oxygen concentration and that of stack temperature, which both use air flow as their

manipulated variable. However, the set point for oxygen concentration is just a minimum requirement: more oxygen is obviously not going to degrade performance. In ordinary operation air flow will be used for temperature control most of the time, as this task usually requires more air than maintaining oxygen concentration: this can be inferred by the fact that all fuel-cell stacks presented in the open literature require some form of cooling, even if they are fed enough oxygen. Oxygen-concentration control will however be allowed to override temperature control. This strategy presents the additional benefit of higher oxygen concentrations in the cathode than for the case of a dedicated cooling system.

7.1 Power Load on the Stack

In order to evaluate the performance of control algorithms, it is useful to have a standard usage pattern to test them. Since fuel cells are often associated with automotive applications, a good usage pattern may be extracted from the New European Driving Cycle (NEDC), a standard velocity-to-time map used in the European Union to test car engines for pollutant emissions [1, 2]. The NEDC is representative of both urban and extra-urban driving in Europe, but many other countries and authorities have defined their own set of driving cycles, such as the United States' FTP-75 and Japan's JP 10–15.

Having obtained the $v(t)$ relationship from the definition of NEDC, it is possible to obtain the corresponding motor power output by making some assumptions on the characteristics of the vehicle. It is then possible, through the power characteristic of the fuel cell, to find a corresponding plot for $i(t)$[1] and $V(t)$, thereby finding the main disturbance terms in all flow and heat differential equations (4.1, 4.10, and 4.12).

The velocity specified by the NEDC standard is plotted in figure 7.1, with the corresponding power required by the vehicle to maintain the specified velocity. The power the motor has to output to make the vehicle maintain the cycle's specified velocity can be calculated as follows [3]:

$$P = \overbrace{m\,g\,C_{rf}\,|v|}^{\text{Rolling resistance}} + \overbrace{\frac{1}{2}\,\rho\,|v|^3\,C_d\,A}^{\text{Air resistance}} + \overbrace{m\,v\,\frac{dv}{dt}}^{\text{Acceleration}} \tag{7.1}$$

The parameters used in this equations are presented in table 7.1.

Having an expression for the required power output, it is now possible to estimate how i will vary. The fuel cell's polarisation curve depends strongly on oxygen

[1] Since the crossover current i_c is small, throughout this chapter we will approximate $i \approx i_r$.

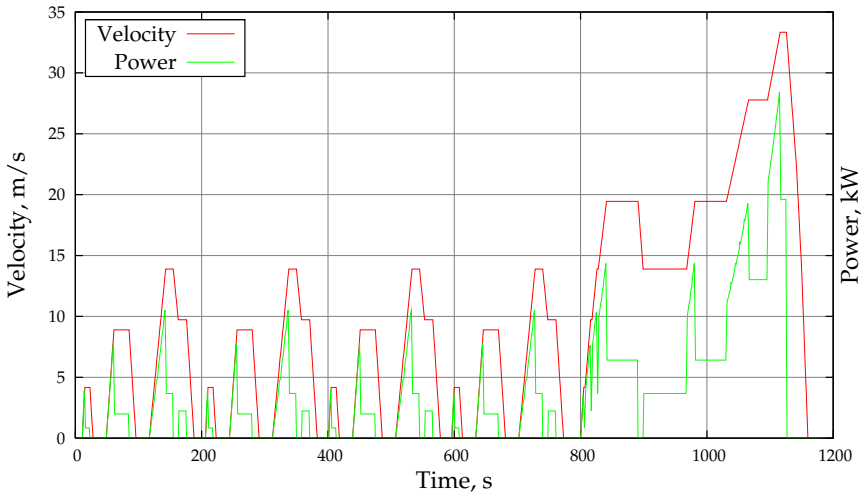

Figure 7.1: The New European Driving Cycle. Negative values of power have been discarded, as we are not considering the possibility of inverting the fuel cells and using them as electrolysers.

Symbol	Unit	Value
m	Mass	1000 kg
g	Gravitational acceleration	9.81 m/s^2
ρ	Air density	1.177 kg/m^3
C_{rf}	Rolling friction coefficient	0.02
C_d	Drag coefficient	0.4
A	Vehicle front area	1.5 m^2

Table 7.1: The parameters used to find the power requirements of a vehicle following the NEDC cycle.

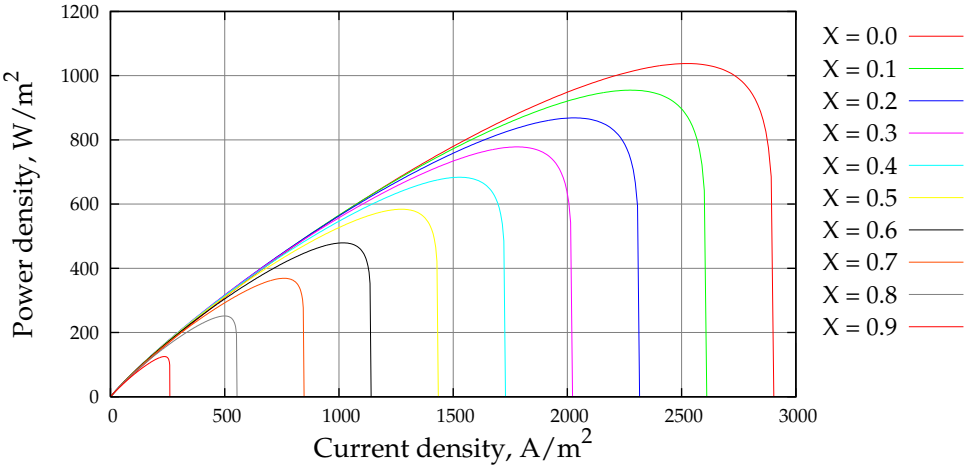

Figure 7.2: Effect of conversion on a cell's power output. The image uses the same data of figure 4.2.

conversion X in the cathode, as shown in figure 4.2. To invert the relationship $P(i, X)$ it is therefore first necessary to assume a value for conversion. Figure 4.3 indicates that conversion must be low for the highest power outputs to be attainable. Furthermore, as shown in figure 7.2, the power output curves do not depend significantly on X until the mass-transport barrier is actually reached for each curve: each curve separates from a common envelope when approaching its mass-transport limit. We will therefore consider this envelope ($X = 0$) a representative estimate to invert $P(i, X)$, because we assume that control will be able to keep the stack away from the mass-transport limit.

We can now find the rate of oxygen consumption, $\frac{i_r(t)\,A}{4\,F}$, and heat generation, $\left[\frac{\Delta h_r}{2\,F} - V(t)\right] i_r(t)$. In all simulations in the remainder of the chapter, we will assume that the fuel cell stack has a total area of $30\,m^2$, resulting in a theoretical maximum power output of 31.13 kW, or 9.5 % more than the maximum required power by NEDC, which is 28.42 kW. Oxygen consumption and heat generation are plotted in figure 7.3, where we can see that they quite closely match the shape of power requirement in figure 7.1.

7.2 Pressure Control of Dead-End Flows (Anode)

In the case of dead-end flows, where there is only one reactant and no products are taken up by the stream, maintaining reactant concentration is equivalent to con-

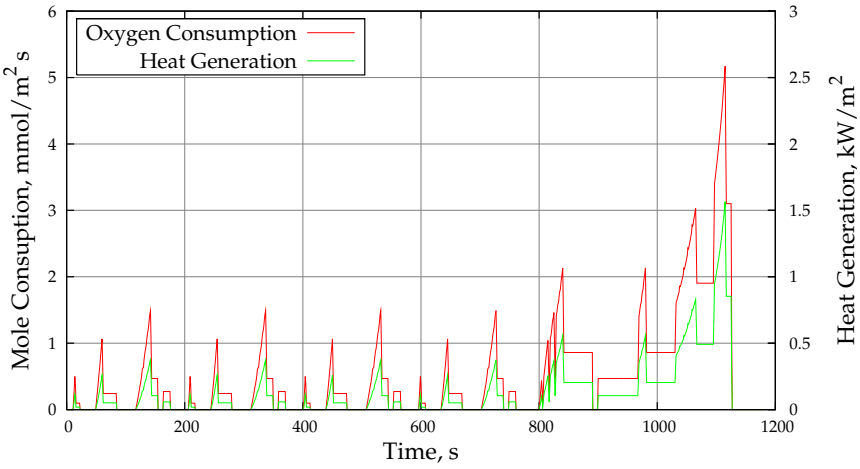

Figure 7.3: The approximate plot of reactant consumption and heat generation along the entire NEDC cycle, assuming $X = 0$. As in practice X will be different from 0, real values may be slightly higher because of the increased overvoltage.

trolling the gas pressure, assuming negligible temperature variations. In general, but especially in the case of hydrogen coming from a pressurised tank, we want to avoid excessive pressure difference across the membrane, to reduce mechanical stress and avoid membrane rupture. As dead-end flows periodically require purging of inert gases, it would be convenient to maintain a pressure slightly higher than atmospheric: this will have the added benefit of leaking hydrogen out instead of letting air in, were a leak to occur.

The differential equation we consider is equation 4.3, from which we remove, for simplicity, the term accounting for temperature variation:

$$\frac{d\,p_{H_2}}{d\,t} = \frac{R\,T}{\mathcal{V}}\,\dot{n}_{H_2} - \frac{R\,T}{\mathcal{V}}\,\frac{i_r\,A}{2\,F} \tag{7.2}$$

Since the system's state p_{H_2} does not appear in the right-hand term, this is an integrating process. As integrating processes are not stable, feedback is mandatory: if there were no pressure measurement, and we only relied on a current measurement to set the flow to compensate consumption, any error would accumulate over time, and we would eventually either run out of hydrogen or rupture the membrane.

Fortunately, pressure measurements are known to be quick and simple to obtain: Huang and Cheng [4] claim that simple and cheap pressure sensors have response times below 0.5 s. We will model the sensor and actuator lag with a simple delay, $\theta_{p_m} = 0.5\,s$. For this case, Skogestad [5] suggests the following design for a PI

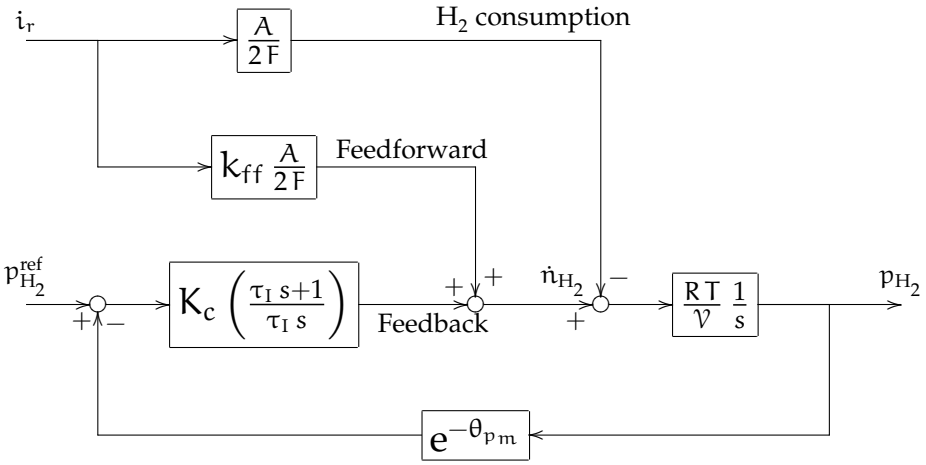

Figure 7.4: Control diagram for pure hydrogen pressure in a dead-end manifold.

feedback controller:

$$\begin{aligned} K_c &= \frac{\mathcal{V}}{RT}\frac{1}{\tau_c + \theta_{p_m}} \\ \tau_I &= 4\,(\tau_c + \theta_{p_m}) \end{aligned} \tag{7.3}$$

Where the desired response time τ_c is the tuning parameter, and having defined the PI control law as:

$$u_{\text{feedback}} = \overbrace{K_c\left(\frac{\tau_I s + 1}{\tau_I s}\right)}^{K(s)}(r - y) \tag{7.4}$$

We can also add some feedforward action, since the only significant disturbance in the process, i_r, can be easily and rapidly measured:

$$u_{\text{feedforward}} = k_{ff}\,\frac{i_r A}{2F} \tag{7.5}$$

Parameter k_{ff} is the feedforward implementation error.

We are still missing a value for gas volume $\mathcal{V}$. This is the volume downstream from the control valve that we manipulate to set the molar inflow $\dot{n}_{H_2}$. As an estimate, we assume $\mathcal{V} = 30\,\text{m}^2 \times 1\,\text{mm} = 30\,\text{dm}^3$, where the area is the same we assumed above and 1 mm is the thickness of a gas channel, as reported in Shan and

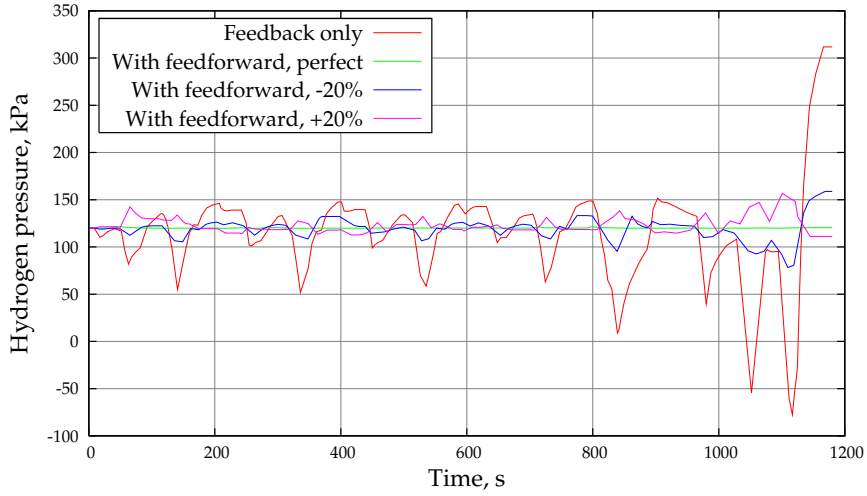

Figure 7.5: The partial pressure of hydrogen as it is controlled by a PI feedback controller, with and without assistance from a feedforward controller (two different values for implementation error are shown), with a set point of 120 kPa, when the fuel cell stack is subject to the NEDC cycle.

Choe [6]. As this estimate neglects the manifold volume, it is expected to be very conservative. The total gas volume may in fact be increased when designing the stack, to improve control properties by making the dynamics slower and easier to deal with.

To test the performance of this control strategy, we can simulate the effect of disturbance $i_r(t)$ as calculated previously for an NEDC cycle. We assume a constant temperature of 150 °C and a set point of $p^0_{H_2} = 120\,\text{kPa}$, plus the overall loop delay $\theta_{p_m} = 0.5\,\text{s}$.

The control system is shown in the control diagram of figure 7.4, with both feedforward and feedback control loops, and the simulation results for the NEDC cycle are plotted in figure 7.5. The simulation for the case of feedback-only control indicates unsatisfactory performance: in order to cope with integrator wind-up in the PI controller[2], τ_c was set to a relatively large level, $\tau_c = 15\,\text{s}$: larger values would cause too sluggish control action, whereas lower would result in significant wind-up. To improve performance, it was necessary to add feedforward action, also plotted in figure 7.5. Even in the case of large implementation errors (±20 %), feedforward makes control performance acceptable. It is however not possible to discard the

[2]It is possible to set $\dot{n}_{H_2}$ only to values larger than zero, so, if the controller were to require less than zero values for the manipulated variable, an integrator wind-up may result.

feedback loop, as system 7.2 is unstable and requires feedback for stabilisation.

7.3 Composition Control of Open-End Flows (Cathode)

Ensuring that oxygen partial pressure in the cathode's bulk be sufficient is in many ways more challenging than controlling hydrogen pressure. Oxygen's partial pressure is much more critical to the performance of the fuel cell than hydrogen's, because of the much higher overvoltage on the cathodic side. At the same time, composition measurements are slower than pressure measurements, resulting in less available bandwidth for feedback control.

The differential equation for the mole fraction of oxygen in a cell's cathode is a particular case of equation 4.10:

$$\frac{p\,\mathcal{V}}{R\,T}\frac{d\,x_{O_2}}{d\,t} = \dot{n}_{air}\left(x_{O_2}^{in} - x_{O_2}\right) - \frac{i_r\,A}{4\,F}\left(1 + x_{O_2}\right) \tag{7.6}$$

This equation presents the additional challenge of being nonlinear, but it has the advantage, compared to equation 7.2, of being stable: in the right-hand term, the coefficient of state variable x_{O_2} is strictly negative. This means that feedback is not strictly necessary, and a pure feedforward approach is possible.

7.3.1 Measurement Dynamics

Measurement of oxygen concentration in gases is frequently reported to be very fast, with bandwidths in the range of 10 Hz [7], but these are usually papers relating to measurement of oxygen concentration in off-gases from stacks or car exhausts: these assume temperatures in much higher ranges than the ones we are considering, generally beyond 700 °C: Park et al. [8] published a paper on an oxygen sensor for "low" temperatures down to 500 °C. Results more relevant for our temperature range (100 to 200 °C) were obtained by Yamamoto et al. [9], who reported that oxygen sensors operating at 100 °C reached steady state after about three minutes, under various values of composition; their plots indicate that the measurement dynamics operated roughly as a lag with a time constant of two minutes. These lags may be reduced by purpose-built equipment, such as sensors that heat up samples of the stack's off-gases to high temperatures to make a faster measurement possible.

7.3.2 Time Constants of Composition Dynamics

We can notice that the time constants[3] of equation 7.6 are quite fast and do not depend on x_{O_2} itself:

$$\tau_{O_2} = \left[-\frac{\partial}{\partial x_{O_2}} \left(\frac{d\, x_{O_2}}{d\, t} \right) \right]^{-1} = \frac{p\, \mathcal{V}}{R\, T} \frac{1}{\dot{n}_{air} + \frac{i_r\, A}{4\, F}} \approx 9\,s \tag{7.7}$$

Here we assumed atmospheric pressure, $i_r \approx 200\,A/m^2$ (roughly the average value through the NEDC with our parameters), $\dot{n}_{air} \approx 5 \times \frac{i_r\, A}{4\, F}$ (since air molar flow has to be five times the oxygen flow because of its composition), and all other conditions as for the hydrogen manifold's case. This indicates that, once a certain input and disturbance are fixed, the system will converge to a steady state: this is especially beneficial for feedforward control, since feedforward techniques cannot stabilise a system by themselves.

It should be remarked that volume $\mathcal{V}$ is, in this case, only the volume inside the gas channels, whereas in the case of hydrogen it was supposed to be all the volume after the control valve, including manifold and piping: that made $\mathcal{V} = 30\,dm^3$ a very low estimate. The hydrogen manifold and piping after the control valve could be included because pressure is transmitted almost instantaneously across that whole volume, whereas diffusion occurs only in the gas channels, not in the whole air manifold. Therefore, in this case, we do not have the option of increasing the time constants by adding some gas buffer that would increase $\mathcal{V}$, which we may have desired to do in order to slow down the plant and reduce the impact of slow measurements, making conditions easier for feedback control.

7.3.3 Feedforward Control

Since the system has satisfyingly fast time constants and is stable, we will consider pure feedforward control. In this case, feedforward control presents many advantages:

- It does not introduce instabilities (if the controller itself is stable);
- It does not rely on measurements of the system's state, which in this particular case are much slower than the system's own dynamics;
- It relies on a measurement of the system's only disturbance, i_r, which we can obtain inexpensively, with high precision and large bandwidth;

[3] Being the system nonlinear, the time "constants" are in fact quite variable; the denomination is however usually kept in the literature.

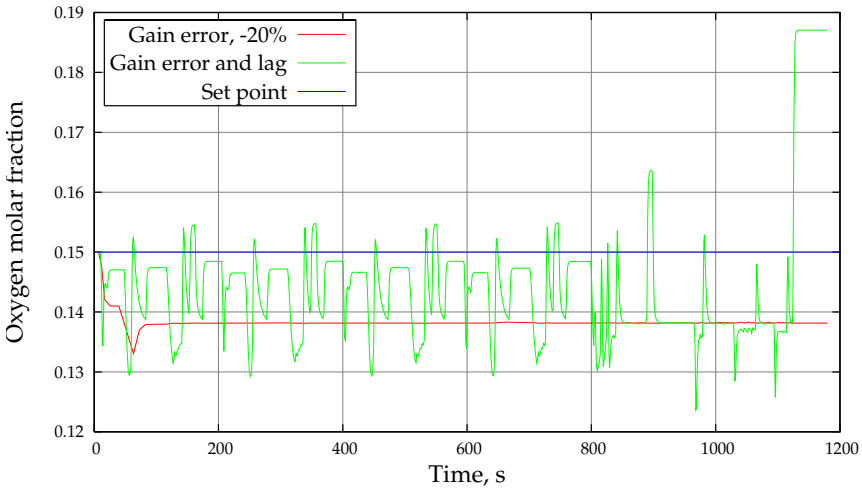

Figure 7.6: Performance of feedforward control in maintaining oxygen molar fraction at 15 % in a fuel cell's cathode through an NEDC cycle. The gain error is −20 % and the actuator lag 1 s.

- In the overall layout sketched in figure 5.4, temperature control competes with this algorithm for the usage of air inflow as a manipulated variable. In these conditions, a PI controller for air composition may exhibit integral wind-up problems.

Even if a feedforward controller cannot reach zero error at steady state as a PI feedback controller could (since feedforward has, by definition, no measurement of the error), we are not concerned about precise tracking, but rather with maintaining an acceptable value of x_{O_2} to guarantee the stack's capability to produce the desired power output.

We may therefore consider setting $\dot{n}_{air}$ so that it compensates for the effects of i_r in equation 7.6, ideally making its right-hand term zero. A feedforward control law is:

$$\dot{n}_{air} = \frac{i_r A}{4F} \frac{1 + x_{O_2}^{ref}}{x_{O_2}^{in} - x_{O_2}^{ref}} \tag{7.8}$$

This control strategy is guaranteed not to introduce instabilities, but will suffer (as any feedforward strategy) from gain error and actuator dynamics, in this case of the air blower or compressor.

The control strategy's performance through an NEDC cycle is plotted in figure 7.6. Law 7.8 takes full advantage of the relatively fast dynamics of x_{O_2}, and main-

tains an acceptable approximation of the set point even with a large actuator bias, $-20\,\%$[4]. When adding a significant actuator lag (1 s), some oscillations do appear, yet operation is not significantly disturbed.

One of the reasons why feedforward works so well is that it relies on the system's stability: the system's time constants (7.7) are much faster for high values of i_r, resulting in much faster dynamics right when the disturbance is at its strongest.

7.3.4 Dimensioning Criterion Based on Actuator Power Consumption

To apply the proposed feedforward control strategy, it is necessary to provide a value for $x_{O_2}^{ref}$. Ideally we would want this to be as high as possible in order to maximise the maximum allowable current, but we cannot simply set $x_{O_2}^{ref} = x_{O_2}^{in}$: it would make input usage infinite (7.8). Indeed, too high a setting will reduce the system's overall efficiency because of the power losses in the actuator.

We can establish a simple criterion for an acceptable value of $x_{O_2}^{ref}$: it should be the value at which the marginal increase in maximum power output from the fuel cell equals the marginal increase in power lost to the blower. The actual value of this set point will however depend on the particular characteristics of the actuator and of the resistance to flow of the stack, and cannot be established in general.

This criterion for oxygen concentration can be translated to a dimensioning criterion for the stack: the maximum available power from the stack will be the one obtained from the power density curve in figure 4.3 for $x_{O_2}^{ref}$. We can therefore calculate the total area that we need to produce a given power. This maximum power density will always be less than that obtained for $x_{O_2}^{in}$, which is the one usually measured under laboratory conditions and reported in the literature.

7.4 Temperature Control

The objective of temperature control is to keep the stack at a given temperature by manipulating the air flow. Having assumed that temperature is uniform in a stack, the equation determining its dynamics is 4.12. However, in that form the equation is somewhat cumbersome:

- Calculating the entering enthalpy requires making assumptions on the control algorithm for the anode flow (not for the cathode flow, which is our manipulated variable);

[4]We did not consider the case of a positive gain error, as we are concerned only with having too little oxygen: excess oxygen will not cause problems, even if the overall efficiency of the system may suffer because of increased input usage.

- Calculating the exiting enthalpy requires tracking a cumbersome set of differential equations for all involved species.

For control purposes, we will further simplify the model so that flow dynamics do not interfere with temperature dynamics. We will assume that:

- The anode (hydrogen) flow is under perfect control, so that $\dot{n}_{H_2} \equiv \frac{i_r A}{2F}$;
- There is no composition transient in the cathode (air) flow.

In practice we are assuming a condition of pseudo-steady state, discarding all dynamic modes but the temperature's. The energy balance can now be translated into a more manageable form, splitting the enthalpy difference in two parts, one for sensible heat and one for reaction heat:

$$\begin{aligned} A\,\hat{c}_p \frac{dT}{dt} &= \dot{H}^{in}(T_0) - \dot{H}^{out}(T) - i_r\,V\,A \\ &= \overbrace{\left(\dot{H}^{in}(T) - \dot{H}^{out}(T)\right)}^{\text{Reaction heat}} - \overbrace{\left(\dot{H}^{in}(T) - \dot{H}^{in}(T_0)\right)}^{\text{Sensible heat}} - i_r\,V\,A \\ &\approx \overbrace{-\Delta h_r(T)}^{\approx 243\,kJ/mol} \left(\frac{i_r A}{2F} + n^c_{H_2}\right) - \sum_i c_{p,i}\,\dot{n}^{in}_i\,(T - T_0) - i_r\,V\,A \end{aligned} \tag{7.9}$$

In the last line of the equation we assumed that constant-pressure specific heat for all the species is approximately constant: this is not very accurate, as can be seen from figure 7.7, but for control-oriented modelling we are more interested in a good approximation than in an accurate model. We also implicitly assumed that hydrogen is the limiting species, something that should hold true with the previously discussed algorithm for composition control.

We can now express the temperature dynamics in the following approximate form, which lends itself well to a control analysis:

$$\begin{aligned} A\,\hat{c}_p \frac{dT}{dt} \approx -c_{p,air}\,(T - T_0)\,\dot{n}_{air} - \left(\Delta h_r(T) + c_{p,H_2}\,(T - T_0)\right)\,\dot{n}^c_{H_2} + \\ - \left(\frac{\Delta h_r(T) + c_{p,H_2}\,(T - T_0)}{2F} + V\right) A\,i_r \end{aligned} \tag{7.10}$$

The equation may be simplified further, noting that the $c_{p,H_2}\,(T - T_0)$ terms are much smaller than the enthalpy of reaction:

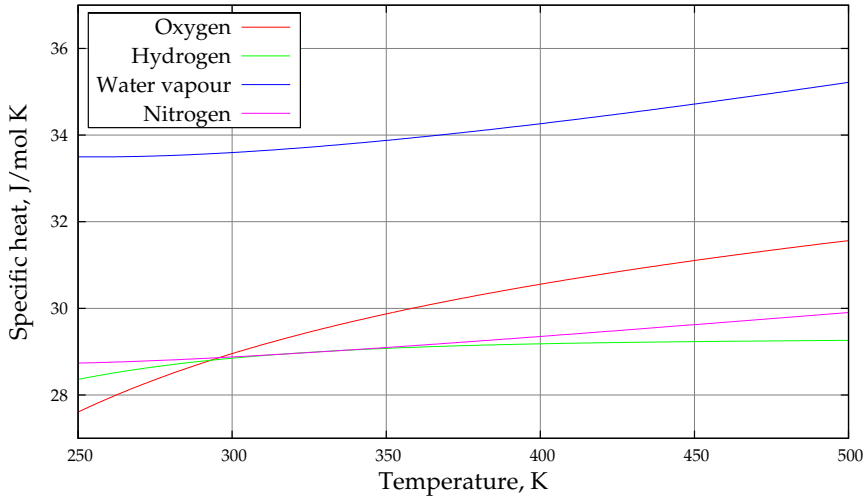

Figure 7.7: The specific heats of the main chemical species in a fuel cell in the temperature range of interest.

$$A\,\hat{c}_p\,\frac{dT}{dt} \approx -c_{p,air}\,(T - T_0)\,\dot{n}_{air} \overbrace{-\Delta h_r(T)}^{\approx 243\,kJ/mol}\,\dot{n}^c_{H_2} + \left(\overbrace{-\frac{\Delta h_r(T)}{2F}}^{\approx 1.26\,V} - V \right) A\,i_r \qquad (7.11)$$

Our system is unfortunately nonlinear in our main manipulated variable, $\dot{n}_{air}$. On the other hand, the system is stable (as long as $T > T_0$): as in the case of cathodic composition, we could rely on feedforward control only. However, as this model contains many more approximations, the effects of disturbance i_r will deviate more markedly from the ones predicted by this equation, or will require a more difficult calculation to be estimated. We have also discarded any effect of heat loss to the environment, meaning that the performance of a pure feedforward approach will be less predictable.

7.4.1 Optimal Reference Value for Temperature Control

Unfortunately, it is not yet clear how to decide the temperature at which a PBI fuel-cell stack should operate at a particular time. On one hand, high temperatures improve catalysis and tolerance to poisons such as CO, but they also reduce the membrane's mechanical strength and may sensibly accelerate the decay of its properties.

Until precise models of the overall effects of temperature on PBI fuel cells appear in the open literature, it will not be possible to synthesise a sound criterion to determine the best temperature at which the stack should be kept.

Therefore, in this analysis, we will simply assume that a reference has somehow been decided, and we will concentrate on the controller instead.

7.4.2 Hydrogen in the Cathodic Flow as an Input Variable

When using $\dot{n}^{c}_{H_2}$ as a manipulated variable to raise the temperature of the entering cathodic flow, there is a danger of raising the temperature so much that the membrane or other components in the fuel-cell stack may be damaged. It is therefore necessary to define a maximum input level beyond which control action will be ignored. A reasonable criterion may be to limit entering temperatures to $T_{max} = 200\,°C$: in that case, the energy balance yields:

$$\left(c_{p,air}\,\dot{n}_{air} + c_{p,H_2}\,\dot{n}_{H_2}\right)\,(T_{max} - T_0) \approx -\Delta h_r\,\dot{n}_{H_2} \tag{7.12}$$

We have again approximated using constant specific heats. The resulting saturation condition is:

$$\dot{n}_{H_2} < \frac{c_{p,air}\,(T_{max} - T_0)}{-\Delta h_r - c_{p,H_2}\,(T_{max} - T_0)}\,\dot{n}_{air} \approx \frac{c_{p,air}\,(T_{max} - T_0)}{-\Delta h_r}\,\dot{n}_{air} \tag{7.13}$$

In the last term in the previous equation we neglected the heating of hydrogen, as it is negligible compared to the reaction heat: the resulting simplified condition is both conservative and linear in T_{max}. An approximate value for the limit of the hydrogen flow burnt to pre-heat the entering cathode gases is about $2\,\%_{mol}$ of the air flow.

7.4.3 Measurement Dynamics

According to Cimerman et al. [10], temperature-measurement dynamics shows a certain dependence on pressure and gas velocity, with the dominant time constants being in the range of 10 to 100 s. Whereas pressure at the outlet of the cell stack will be fairly constant at atmospheric value, gas velocity may change significantly depending on the current gas inflow, and to some degree on the reaction rate. Furthermore, if the temperature measurement is placed at the stack's outlet, a delay in measurement will occur because of the time outlet gases use to pass through the exit manifold. We will assume a worst-case condition with a lag $\tau_{T_m} = 100\,s$ and a delay $\theta_{T_m} = 10\,s$.

7.4.4 Time Constants of Temperature Dynamics

As for the case of composition control, it is useful to estimate the system's time constants. As $\Delta h_r(T)$ does not change significantly with temperature, terms related to it (i_r and $\dot{n}^c_{H_2}$) will be ignored. The time constants are derived from equation 7.9:

$$\tau_T = \left[-\frac{\partial}{\partial T} \left(\frac{dT}{dt} \right) \right]^{-1} = \frac{A \hat{c}_p}{\sum_i c_{p,i} \dot{n}_i} \approx 19\,000\,\text{s} \tag{7.14}$$

In this expression, we assumed for approximation that the gases' specific heats are all 29 J/mol K, that hydrogen flow is stoichiometric and that air flow is perfectly controlled to maintain an oxygen fraction of 0.15 in the cathode gases. Since the average current density through the NEDC cycle is 200 A/m^2, this results in an average value $\sum_i \dot{n}_i = \left(1 + \frac{1+0.15}{0.2-0.15}\right) \frac{i_r A}{4F} \approx 373\,\text{mmol/s}$. This time constant corresponds to over five hours, but can be made significantly smaller by increasing the air flow, and with it the stoichiometric ratio.

Indeed, if we set $\dot{n}_{air}$ such as to balance out the approximate differential equation 7.11, knowing that the average power density output through the NEDC cycle is $V i_r \approx 120\,\text{W/m}^2$, and assuming a temperature difference $T - T_0 \approx 150\,\text{K}$, we obtain a much larger flow:

$$\dot{n}_{air} = \frac{\frac{-\Delta h_r}{2F} A i_r - V i_r A}{c_{p,air} (T - T_0)} \approx 910\,\text{mmol/s} \tag{7.15}$$

This will result in specularly smaller time constants (in this specific example, about two hours).

7.4.5 Controller Synthesis and Simulation

We have seen that, fortunately, the time constants of temperature dynamics are much slower than temperature measurements, with a gap of about two orders of magnitude. To devise an appropriate controller, we use again Skogestad's tuning rules [5]; to avoid a too aggressive controller that may saturate the input variable (we cannot have $\dot{n}_{air} < 0$), we set a large desired response time, $\tau_c \approx 100\,\text{s}$.

As previously remarked, the system in equation 7.11 is stable but nonlinear. In order to apply linear control theory, we first have to change the control variables so that the system becomes linear. It is straightforward to define the input variable as:

$$u = -c_{p,air} (T - T_0) \dot{n}_{air} - \Delta h_r(T) \dot{n}^c_{H_2} \tag{7.16}$$

It would be then possible to control the system using u, calculating back the value of $\dot{n}_{air}$ (or if necessary $\dot{n}^c_{H_2}$) to apply when setting the actuator. However, this

transformation has made the system unstable[5]: it is now an integrating process, and will require feedback to be stabilised. The ultimate cause of the induced instability is the form of actuator function $\dot{n}_{air} = f(u)$, that depends on a temperature measurement: to remove this internal feedback and make the system stable again, we use the reference T^{ref} directly, instead of temperature measurement T_m.

We proceed then to synthesise a feedback controller. Since control variable $\dot{n}_{air}$ is set to be the maximum of the signals coming from the control loops of composition and the temperature, using a temperature controller containing an integrator may cause wind-up issues. Therefore, we will use a simple proportional controller. The feedback control law is then:

$$\dot{n}_{air,\,feedback} = -\frac{A\,\hat{c}_p}{c_{p,air}\,(T^{ref} - T_0)}\,\frac{1}{\tau_c + \theta_{T_m}}\,(T - T_m) \tag{7.17}$$

We also add a feedforward term to improve the dynamic properties of the controller:

$$\dot{n}_{air,\,feedforward} = \frac{\left(-\frac{\Delta h_r}{2F} - V\right)\,i_r\,A}{c_{p,air}\,(T^{ref} - T_0)} \tag{7.18}$$

The proposed control structure is then simulated against the original thermal model 4.12, which also includes the transients in composition of all cathodic species. The competing feedforward controller for air composition developed in the previous section is assumed to be perfectly implemented and set to $x_{O_2}^{ref} = 0.15$. Ambient temperature T_0 is assumed to be 300 K, the stack's initial temperature 400 K, and reference T^{ref} is given constant at 450 K. The results, for the cases of feedback-only and feedback with feedforward, are plotted in figure 7.8 for a series of 10 NEDC cycles.

Even with the many simplifications introduced in controller design, the resulting feedback controller is able to maintain the stack within 10 K of its set point, with peaks corresponding to the stack's maximum power outputs in the NEDC cycles. The addition of a feedforward component, even with a large $\pm 20\,\%$ gain error, manages to keep the oscillations in a narrow band of just 5 K. However, the slow dynamics of stack temperature still require about four NEDC cycles (about one hour and fifteen minutes) to reach 450 K from the starting temperature of 400 K: during this time, the temperature controller tries to keep the lowest possible air feed rate, and is superseded by the air composition controller. Using a higher setting for $x_{O_2}^{ref}$

[5] In fact, the system is still stable: the heat loss $\dot{H}^{loss}$, which we neglected, will most likely increase with temperature. We also neglected the sensible heat necessary to heat hydrogen up to cell temperature, which will also have a stabilising effect on temperature. However, these contributions are going to be so small they will have little effect on dynamics.

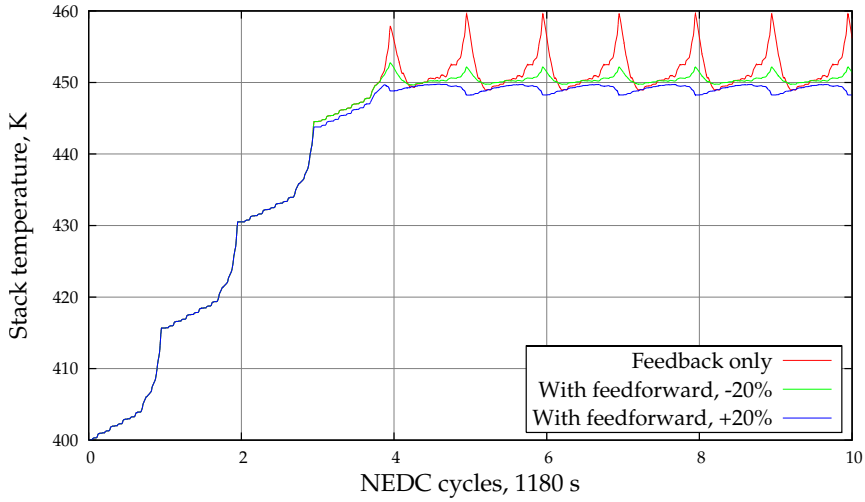

Figure 7.8: Performance of the proposed feedback and feedforward algorithms for temperature control. All transients are the same for about the first four NEDC cycles because temperature control is overridden by composition control until then.

will result in a higher minimum air flow, and therefore longer transient time when stepping up the temperature reference.

The effect of an increasing set point for oxygen molar fraction are pictured in figure 7.9. The feedback-feedforward approach of figure 7.8 (this time with no feedforward gain error) has been put in competition with feedforward composition controllers with increasing set points. As the air composition requirement increases beyond 15 %, temperature dynamics rapidly deteriorate. At some setting of $x_{O_2}^{ref}$, increasing or maintaining temperature will eventually become impossible, because of the excessive requirements of composition control: this will have consequences for the stack dimensioning criterion of section 7.3.4, as it places an upper boundary on the value of $x_{O_2}^{ref}$ beyond which temperature control is infeasible.

The composition set point, however, influences the performance of temperature control only for the case of increasing stack temperature, when composition control requires higher minimum thresholds to maintain a certain composition: since composition control does not set a *maximum* threshold, the temperature control loop will not be limited by it when the objective is to decrease the stack temperature, and it will be able to set an air flow as high as feasible for the actuator.

The air flow required for our test case, assuming no gain error for the feedforward controller component, is plotted in figure 7.10. The most important observation from this figure is that the air flow required to control the stack's temperature

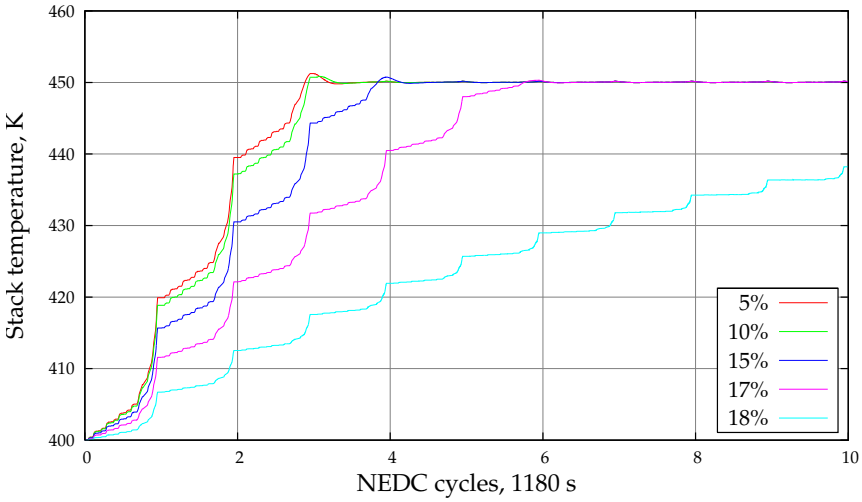

Figure 7.9: The influence of the set point for composition control on the performance of temperature control. All feedforward controllers, both for composition and temperature control, are modelled without gain error.

is not impractically higher than the one required to maintain the reaction, and is indeed not higher at all for the case of feedback control only: the first two peaks in air flow are caused by the air composition controller, which is at that time setting the lower bound of air flow (as shown in figure 7.8), whereas the later ones are caused by the feedforward component of temperature control.

The peaks in the air flow required by composition control must actually be strictly followed, because otherwise the fast composition dynamics at high currents would rapidly deplete the oxygen supply, and thereby halt the stack's operation. Instead, the slower dynamics of temperature allows a significant relaxation of the peaks requested by feedforward temperature control, possibly by using a low-pass filter on the feedforward component or by discarding it entirely: the stack temperature may temporarily increase, as it does under feedback control, but this will not disrupt operation of the stack, whereas oxygen depletion would immediately halt the reaction current. The heat is then dispersed by maintaining a lower peak air flow over a longer time.

7.4.6 Temperature Control with Hydrogen Combustion

Burning H_2 in the cathode inlet to increase the inflow air temperature is a last resort to raise the stack's temperature when the stack itself cannot generate heat, typically

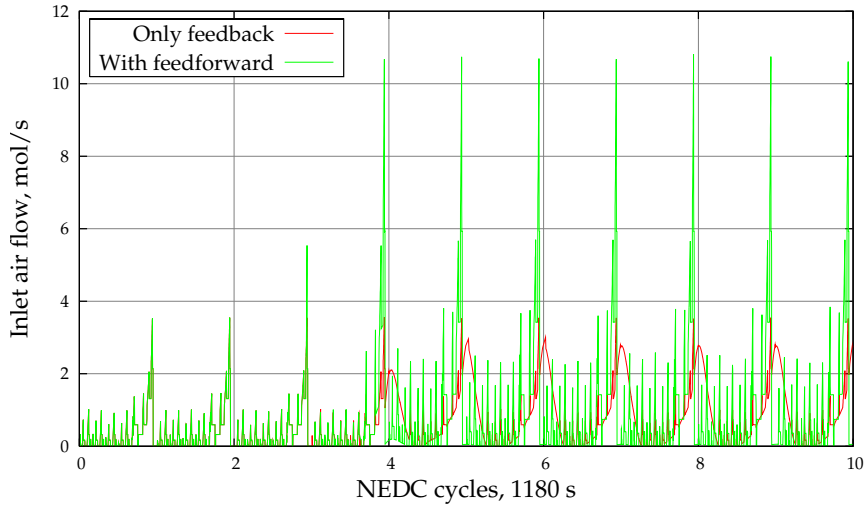

Figure 7.10: The air flow required by the joint composition-temperature control systems of figure 5.4, connected by a maximum selector. No gain errors in either composition or temperature control are modelled.

because it is at too low a temperature for the electrochemical reaction to proceed and generate enough heat by itself. In that case, we also want to limit the inlet temperature so that the cells will not be damaged by excessive temperatures: as seen in section 7.4.2, this may be achieved by limiting the hydrogen flow into the cathode inlet's burner to 2 $\%_{mol}$ of the air flow.

However, it is also necessary to change the control strategy. The previously illustrated feedback and feedforward controllers were designed to increase temperature in the stack by maintaining a minimum air flow, which was set according to the requirements of the composition controller. When burning hydrogen in the cathode inlet, the entering air flow will actually have a temperature higher than the stack, so increasing flow will increase the stack's temperature, not reduce it as in the normal case.

As a possible start-up approach, we will consider a very simple strategy. When the stack temperature is measured to be lower than a preset minimum, in our example 400 K, cathodic stack inflow will be set to maximum, in our example 5 mol/s (slightly above what strictly required by composition control in figure 7.10) and hydrogen burnt in the entering cathode flow will be exactly 2 % of that. The temperature at which the previously defined feedback and feedforward controllers take over should be below any operational value for temperature, to avoid hysteresis between the two modes. However, this temperature should also be high enough for

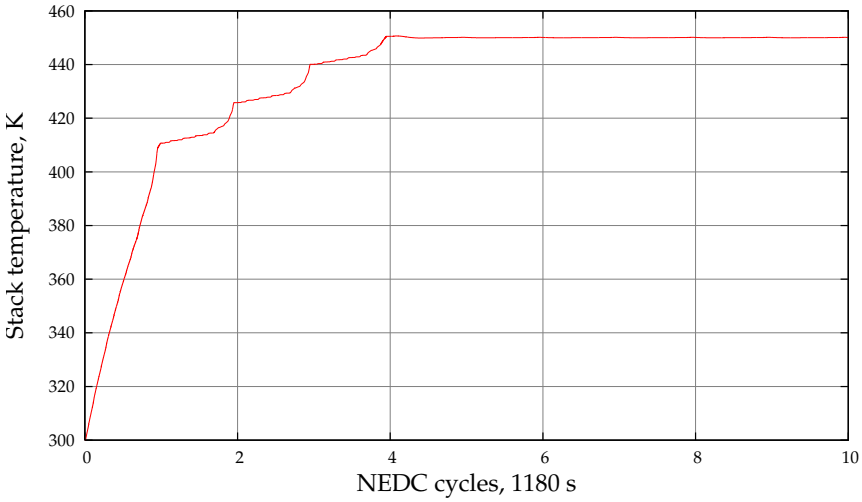

Figure 7.11: The start-up from ambient temperature of a fuel-cell stack. The burner is active until the stack is measured to reach 400 K (note the measurement lag).

the cell to be able to function and generate heat by itself.

Temperature as a function of time is plotted in figure 7.11, where hydrogen is fed to the cathode inlet burner for 1160 s[6]. With the assumed maximum flow, it will take about the duration of an entire NEDC cycle to heat up the stack to the minimum functioning temperature. This rise time may be reduced by increasing the maximum flow during the start-up sequence, which may require modifications to the stack and its ancillary units. As the ratio of hydrogen and air is fixed, the specific enthalpy of the entering flow is constant with respect to the air flow[7]: this means that the rise time to the minimum operating temperature will be roughly inversely proportional to the maximum air flow the blower or compressor can produce. The design start-up time will therefore set a requirement on the actuator dimensioning.

As burning hydrogen on the cathode inlet is a particularly wasteful usage of the available exergy of hydrogen, we should seek to reduce it as much as possible. It may be found advantageous to add a recuperating heat exchanger to pass heat from the cathode's outlet to the inlet to the burner. In this case, the hydrogen flow will also have to be carefully adjusted so that the temperature of entering air does not exceed the specified limits. Such a recuperating heat exchanger may also be useful when raising stack temperature, or when trying to maintain temperature

[6]Hydrogen burning continues for some time after reaching 400 K because of the lag and delay in temperature measurement, which determines burner usage.

[7]Assuming no significant contribution from the blower or compressor.

at high flow rates (possibly caused by a high set point for $x_{O_2}^{ref}$). This exchanger will however be bypassed during normal operation, as it would only hinder the dissipation of reaction heat.

7.5 Conclusions

This chapter has proposed some simple control algorithms for the fuel-cell dynamics associated to chemical engineering. Assuming some typical parameters for a vehicle, profiles for $i_r(t)$ and $P(t)$ based on the New European Driving Cycle were generated, and they were used to test all controllers.

As the hydrogen manifold is assumed to be dead-ended, it was decided to use anode pressure as a controlled variable for the hydrogen material balance. As the system is unstable, feedback is necessary, and a feedback-feedforward controller was synthesised.

Control of air composition was implemented with a feedforward-only approach, as the slow measurement made feedback unpractical.

Temperature in fuel cells is normally controlled with a separate cooling system. We presented a new strategy in which air flow is used to control both air composition and temperature. Since there are two controlled variables but only one manipulated variable, a maximum selector is used, as shown in figure 5.4. The maximum selector effectively avoids that oxygen is depleted in the cathode, insuring a minimum air flow, and returns control to the temperature controller when it requires a higher air flow.

Analysis of temperature dynamics required more simplifications than for the other systems to be put into an acceptable form for control. For this reason, even though the resulting system is stable, it was chosen to have both a feedback and a feedforward component. The feedback component had only a proportional part, to avoid wind-up issues that an integrator may have caused when air flow had been set to the minimum required by air composition control for a long period of time, as in figure 7.8. The performance of the temperature controller was acceptable, but also influenced by the set point assigned to composition control for the case of increasing temperature.

Finally, a simple control strategy for cold start was devised, in which the stack is heated with the combustion products of air and a small quantity of hydrogen. The performance of this strategy depends directly on the maximum cathode throughput that the actuator can deliver.

7.5.1 Dimensioning Criteria

Some control-related dimensioning criteria were identified during the analyses:

- A larger anodic gas-manifold volume will slow down hydrogen-pressure dynamics, making it possible to obtain better control performance by increasing manifold volume, which acts as a buffer. The controller design was carried out with the very conservative case of no manifold volume.
- A stack dimensioning criterion based on power density was obtained observing that it is not possible to maintain maximum oxygen partial pressure under operation. Depending on the energy consumption of the air blower or compressor, a stack will need to be oversized in terms of the maximum power it can deliver, which is roughly linear with the actual oxygen partial pressure in the cathodic gas bulk.
- The set point for air composition control must be chosen so it does not override temperature control so often as to make it impossible to maintain a given temperature. In practice this means an upper limit, such as $x_{O_2}^{ref} \leqslant 18\,\%$.
- The air blower or compressor will have to be able to deliver at least the maximum flow required by air composition control, as the maintenance of this variable is critical to operation of the stack. Further capacity may improve temperature control and will be used by its feedforward component. The blower or compressor's maximum throughput will directly influence the dynamics of cold start, which may be specified as a design parameter.

Bibliography

[1] European Economic Community. Council directive 91/441/EEC of 26 june 1991 amending directive 70/220/EEC on the approximation of the laws of the Member States relating to measures to be taken against air pollution by emissions from motor vehicles, June 1991. URL `http://eur-lex.europa.eu/LexUriServ/LexUriServ.do?uri=CELEX:31991L0441:EN:HTML`.

[2] European Community. Commission directive 93/116/EC of 17 december 1993 adapting to technical progress council directive 80/1268/EEC relating to the fuel consumption of motor vehicles, December 1993. URL `http://eur-lex.europa.eu/LexUriServ/LexUriServ.do?uri=CELEX:31993L0116:EN:HTML`.

[3] Rune L. Johansen. Fuel cells in vehicles. Master's thesis, Norwegian University of Science and Technology, 2003.

[4] Jung-Tang Huang and Shao-Chang Cheng. Study of injection molding pressure sensor with low cost and small probe. *Sensors and Actuators A: physical*, 101:269–274, 2002.

[5] Sigurd Skogestad. Simple analytic rules for model reduction and PID controller tuning. *Journal of Process Control*, 13:291–309, 2003.

[6] Yuyao Shan and Song-Yul Choe. A high dynamic PEM fuel cell model with temperature effects. *Journal of Power Sources*, 145:30–39, 2005.

[7] Kathy Sahner, Ralf Moos, Noriya Izu, Woosuck Shin, and Norimitsu Murayama. Response kinetics of temperature-independent resistive oxygen sensor formulations: a comparative study. *Sensors and Actuators B: chemical*, 113:112–119, 2006.

[8] J. S. Park, C. O. Park, H. J. Kim, and N. Miura. Low temperature oxygen sensor using YSZ | β–β″ alumina bielectrolyte. *Solid State Ionics*, 176:1371–1375, 2005.

[9] Kousuke Yamamoto, Toshihiro Kasuga, and Masayuki Nogami. An oxygen sensor based on copper(I)-conducting $CuTi_2(PO_4)_3$ glass ceramics. *Applied Physics Letters*, 73 (22):3297–3299, 1998.

[10] Franc Cimerman, Bogdan Blagojević, and Ivan Bajsić. Identification of the dynamic properties of temperature-sensors in natural and petroleum gas. *Sensors and Actuators A: physical*, 96:1–13, 2002.

Chapter 8

Conclusions

This thesis has tried to present a complete view of the dynamics of a particular type of high-temperature PEM fuel cell, and the control systems that would be needed to permit its operation.

It was important to realise that fuel cells have many dynamic modes, as illustrated by figure 5.2 on page 72. These influence each other, but operate in different time scales, as summarised in figure 8.1. These time scales are not the only factors to be considered, as the actual shape of the transients is also important: transients in overvoltage have been shown to guarantee the theoretical possibility of perfect tracking in power output, whereas the dynamics of buck-boost converters, the fastest among the ones studied, were nonetheless the most difficult because of the variable RHP zero they presented.

Even if some dynamic modes are very slow, such as temperature's, this is not necessarily a relevant factor in determining control performance. In fact, this depends very much on how we define performance.

If we were to define the control performance in terms of the temperature transient, we may come to the conclusion that fuel cells are very slow systems; if we considered only oxygen concentration, we would conclude that application of feedback control is impractical due to the large delays in measurement.

However, most users would define the performance of a fuel cell system by its dynamics in its intended task, namely to deliver electric power. This has been shown not to be limited by the overvoltage transient, but only by the converter dynamics. Once these are controlled, they define the performance of the system, as far as a user is concerned.

Other dynamic modes, however, cannot simply be ignored. The main objective for the three control loops related to chemical engineering (stack temperature,

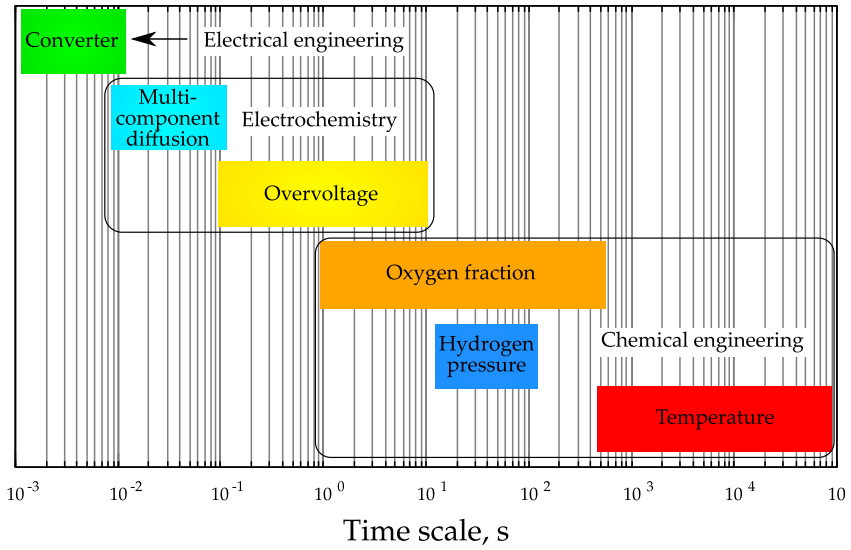

Figure 8.1: Summary of the time scales of the various dynamic modes of fuel cells, as investigated in this thesis.

cathodic oxygen fraction, anodic hydrogen pressure) is to maintain acceptable conditions for the reaction to be possible. However, their dynamic requirements are not as stringent as for power production.

8.1 Suggested Control Strategy

The results presented in the previous chapters are summarised in figure 8.2. The complete control system is made out of four separate loops:

- A proportional-integral feedback controller, coupled with feedforward based on current measurements, to control the hydrogen pressure in the anode;
- A feedforward-only controller to set the minimum air flow that guarantees a certain oxygen molar fraction;
- A proportional feedback controller, optionally complemented by feedforward, manipulating the air flow to control the stack temperature;
- The temperature controller also implements the start-up sequence, with maximum flow and hydrogen combustion in the burner at the cathode manifold's inlet;

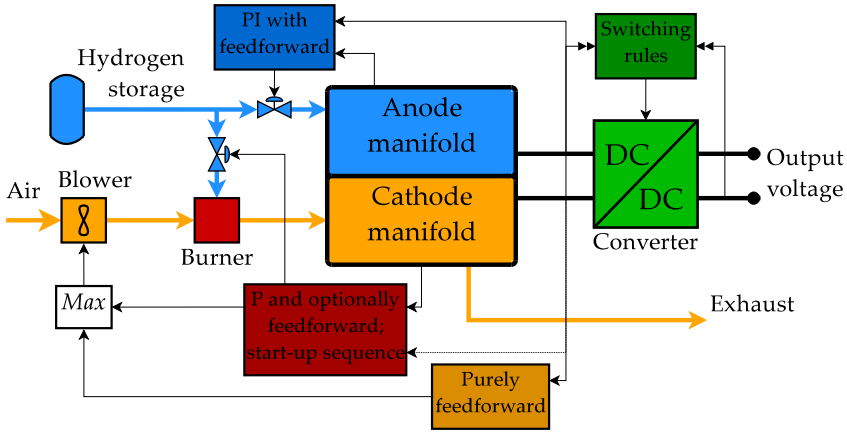

Figure 8.2: The suggested layout for control of a PBI fuel cell stack, with four independent control loops.

- A converter controller based on switching rules, determining the setting of the buck-boost converter's switch depending on measurements of voltage and current on both sides of the converter.

8.2 Further Work

This thesis considered a small subset of fuel cells. It would be useful to develop control strategies for Nafion-membrane PEM fuel cells, where water management must be taken into account, or solid-oxide fuel cells, which have radically different structure, reactions and purpose.

Even for the polybenzimidazole membranes considered in this thesis, data is lacking. It would be of particular interest to implement data regarding anodic resistance to CO poisoning and membrane degradation to obtain a reasonable set point for temperature.

The dynamics of hydrogen storage and supply have not been considered in this thesis, but will be of great importance in the actual performance of a fuel-cell system. It would be useful to model the dynamics of various types of hydrogen storage, such as gas tanks, cryogenic storage, or metal hydrides.

PBI fuel cells are particularly apt to utilise hydrogen produced by steam reforming, due to their tolerance for CO. The presented model could be extended for the case of an open-end anodic manifold, which is necessary to avoid accumulation of

poisoning species.

A strategy should be developed for the situations when a buck-boost converter tries to extract more than the maximum power output deliverable by the fuel-cell stack, since this situation may bring the fuel cell to the mass-transport limit and cause inefficient operation. An appropriate exit strategy from this condition must be devised.

The C++ library presented in this thesis may also be extended for those processes closer to chemical engineering (which have been studied with Simulink in this thesis), and to simulate other types of fuel cells.

Appendix A

Model Code

A C++ implementation of the dynamic model presented in chapter 3 has been included in this thesis as a `tar.gz` attachment to the PDF file. It was chosen not to include the code in print, because over 4000 lines of code would have significantly increased the number of pages without making it any easier to import the files themselves into other projects.

In addition, Simulink models and Matlab scripts used for simulation and control of converters, pressure, composition and temperature dynamics are included in the attached archive. The source code of some dynamically linked Octave functions, used as access functions to the library, is also included.

These files are distributed according to the terms of the GNU General Public License: this means that the code is freely available to anyone, with the condition that redistribution of this software or derivative works shall follow the same terms[1]. The C++ code depends on the GNU Scientific Library (GSL) and on Octave; both the GSL and Octave are also licenced according to the GNU General Public License, and can be downloaded at no cost.

Note that some versions of popular programs (such as Acrobat Reader 7) have a bug that does not allow them to save some types of attachments. In that case, attachments can be extracted from the PDF file using the freely available tool `pdftk`[2] by issuing the command:

```
$ pdftk thesis.pdf unpack_files output /path/to/folder
```

The C++ code can be compiled on UNIX-compatible systems with the customary procedure for GNU programs:

[1] See `http://www.gnu.org/copyleft/gpl.html` for the complete text.
[2] Available from `http://www.accesspdf.com/pdftk/`.

```
$ tar -xzvf FC++-1.0.tar.gz
$ cd FC++-1.0
$ ./configure --prefix=/usr
$ make
# make install
```

The last step will install the fuel-cell model as a shared library in the system. Dynamically linked functions, Simulink models and Matlab scripts will not be installed. Dynamically linked functions, stored in the `src/` folder, can be compiled after installing the library with Octave's build tool for them, `mkoctfile`:

```
$ mkoctfile function.cpp -lgsl -lgslcblas -lfuelcell
```

The code is reasonably portable, and it should be possible to compile it under other operating systems with little additional effort.

Appendix B

$\mathcal{H}_\infty$ Synthesis Plots

This appendix presents the plots resulting from the $\mathcal{H}_\infty$ synthesis performed in section 6.5.2. Linearisations are performed, unless for the variable specified in each plot, around the point $V_{in} = 50\,V$, $I_L = 200\,A$ and $D = 0.5$. Variables are scaled as on page 96, with v_C scaled to a nominal maximum of 200 V, v_{in} to 50 V, i_{out} to 200 A and no scaling for d.

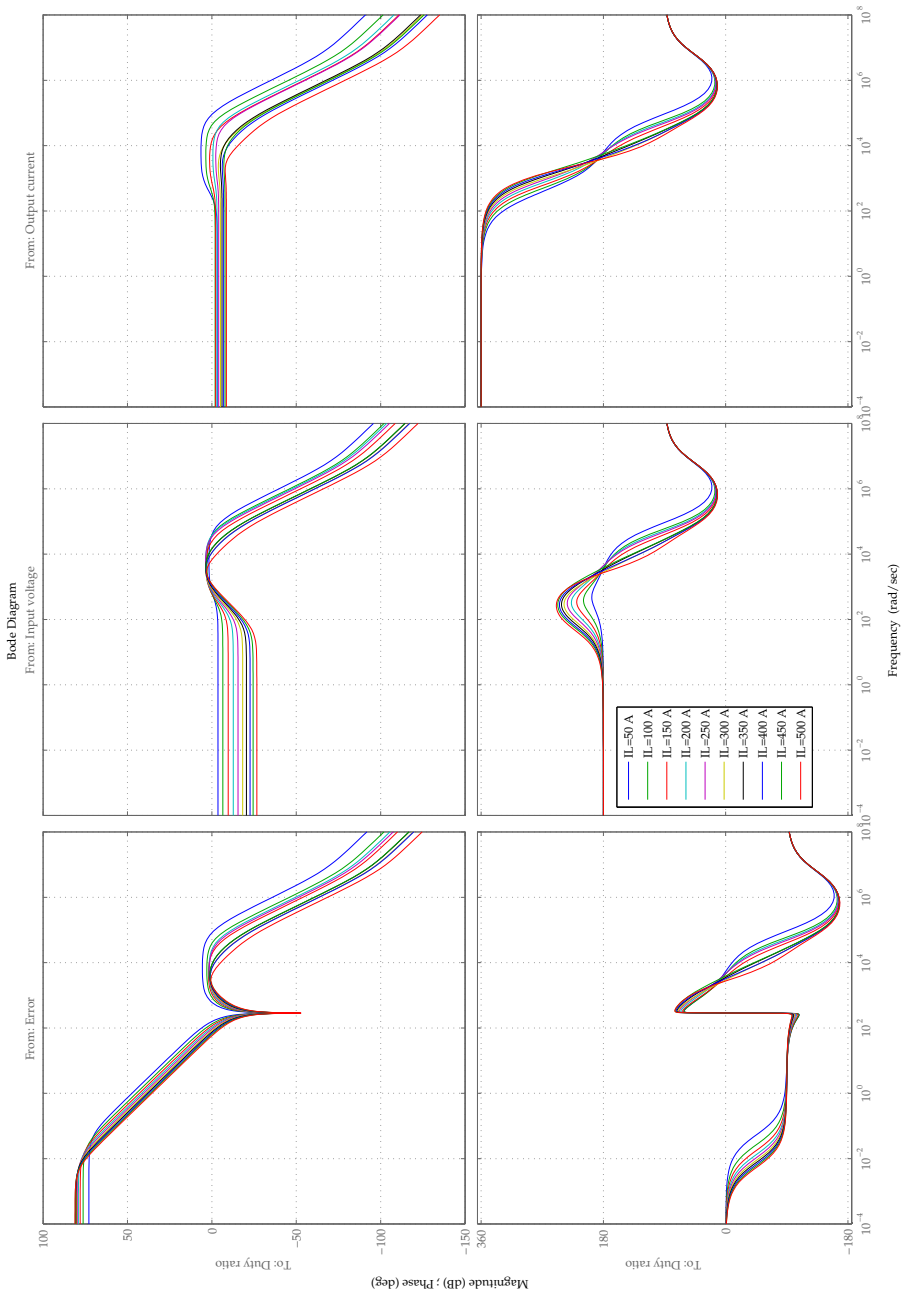

Figure B.1: Bode plots for the $\mathcal{H}_\infty$ controller at various values of I_L, fixing D at 0.5 and V_{in} at 50 V.

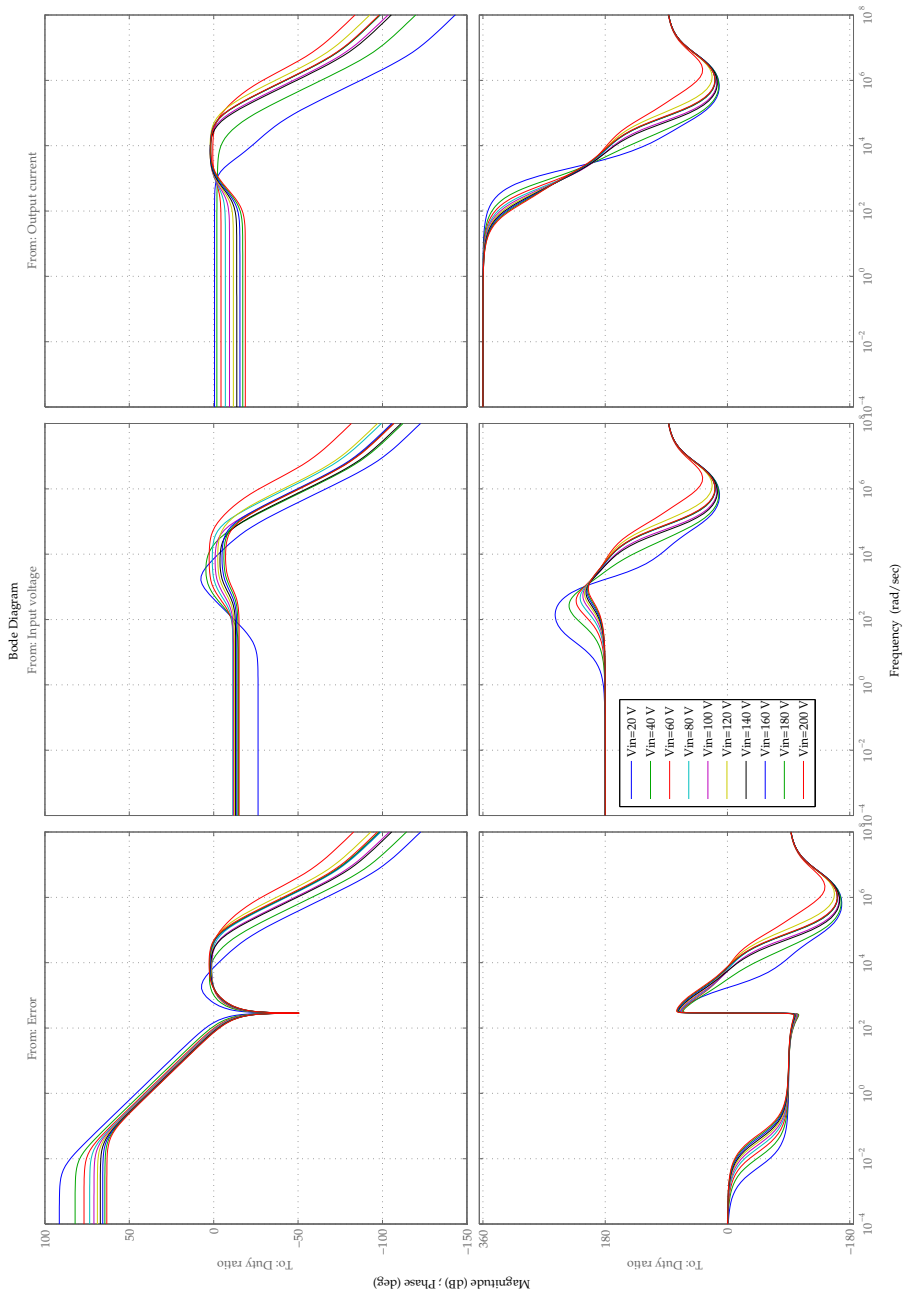

Figure B.2: Bode plots for the $\mathcal{H}_\infty$ controller at various values of V_{in}, fixing D at 0.5 and I_L at 200 A.

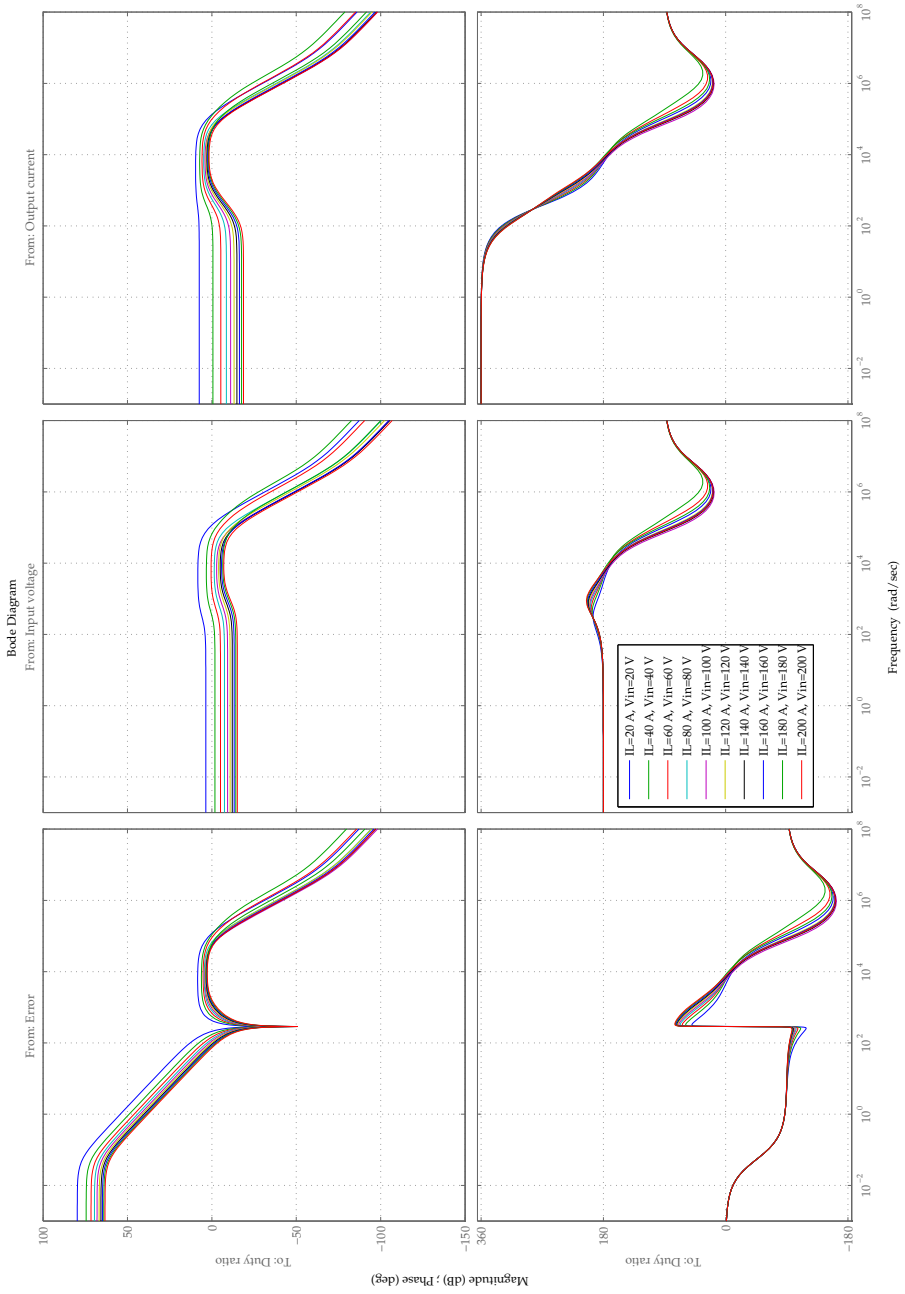

Figure B.3: Bode plots for the $\mathcal{H}_\infty$ controller at various values of I_L and V_{in}, fixing D at 0.5 and the ratio $\frac{I_L}{V_{in}}$ at 1 A/V. In this way, the RHP zero in the plant remains constant.

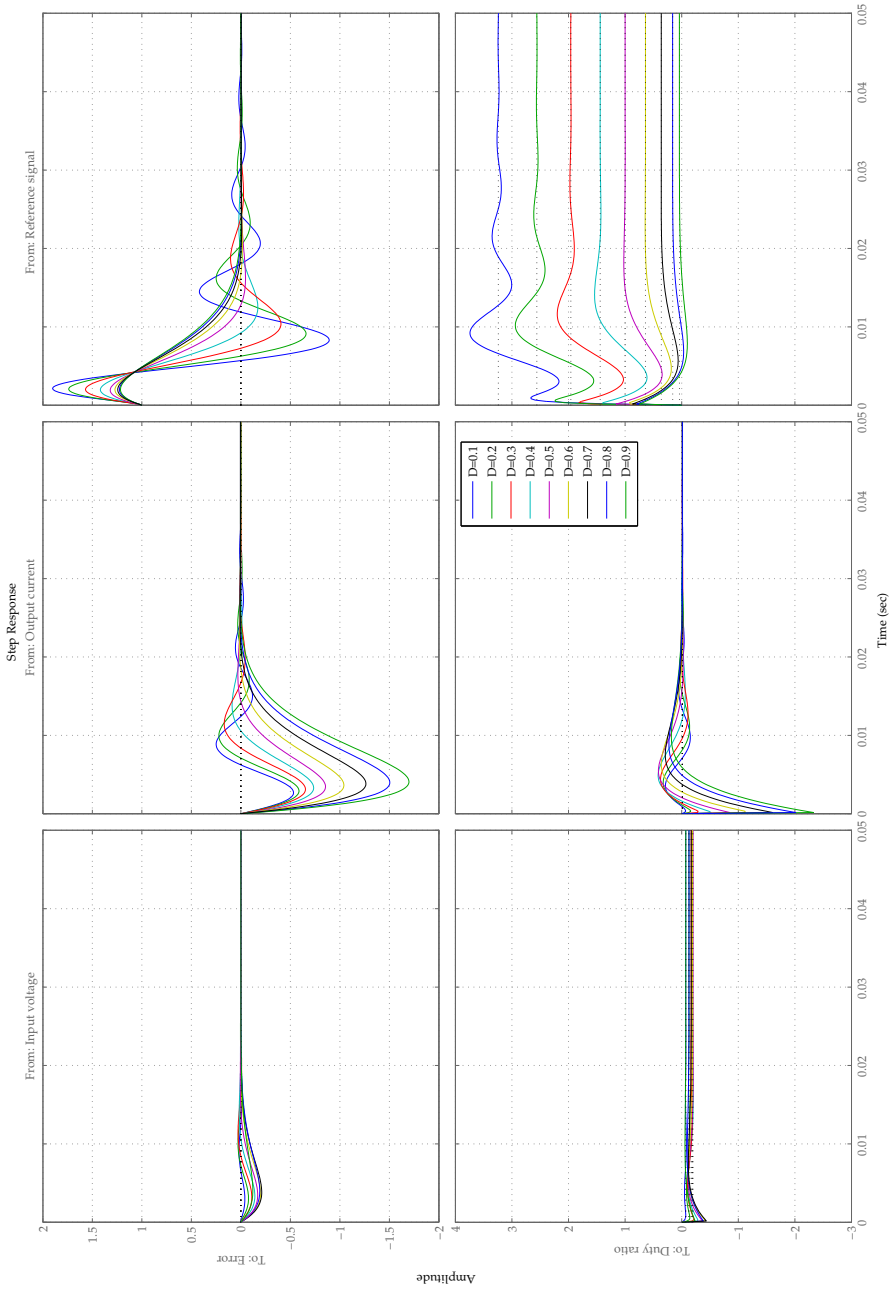

Figure B.4: Step responses for the closed $\mathcal{H}_\infty$-controlled system at various values of D, fixing I_L at 200 A and V_{in} at 50 V.

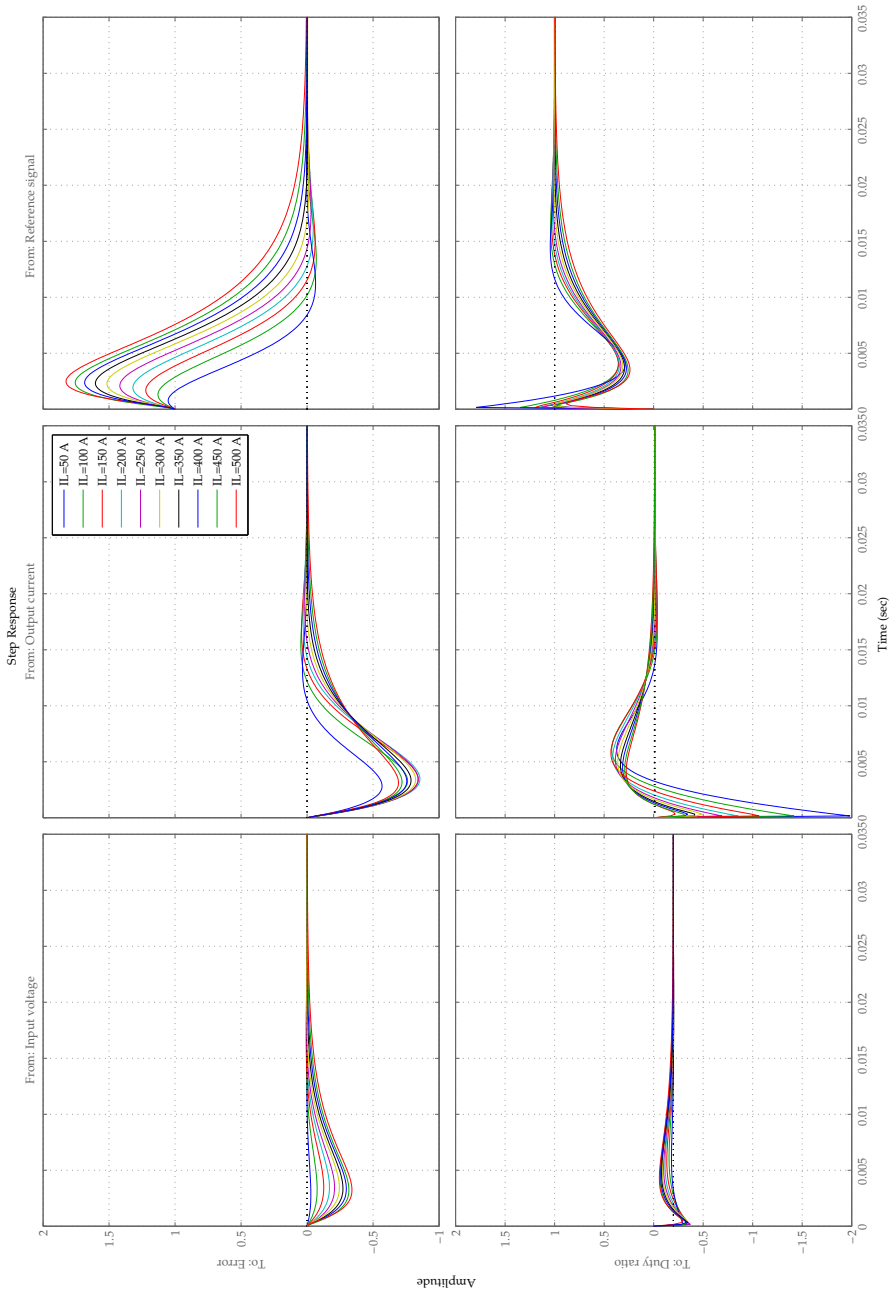

Figure B.5: Step responses for the closed $\mathcal{H}_\infty$-controlled system at various values of I_L, fixing D at 0.5 and V_{in} at 50 V.

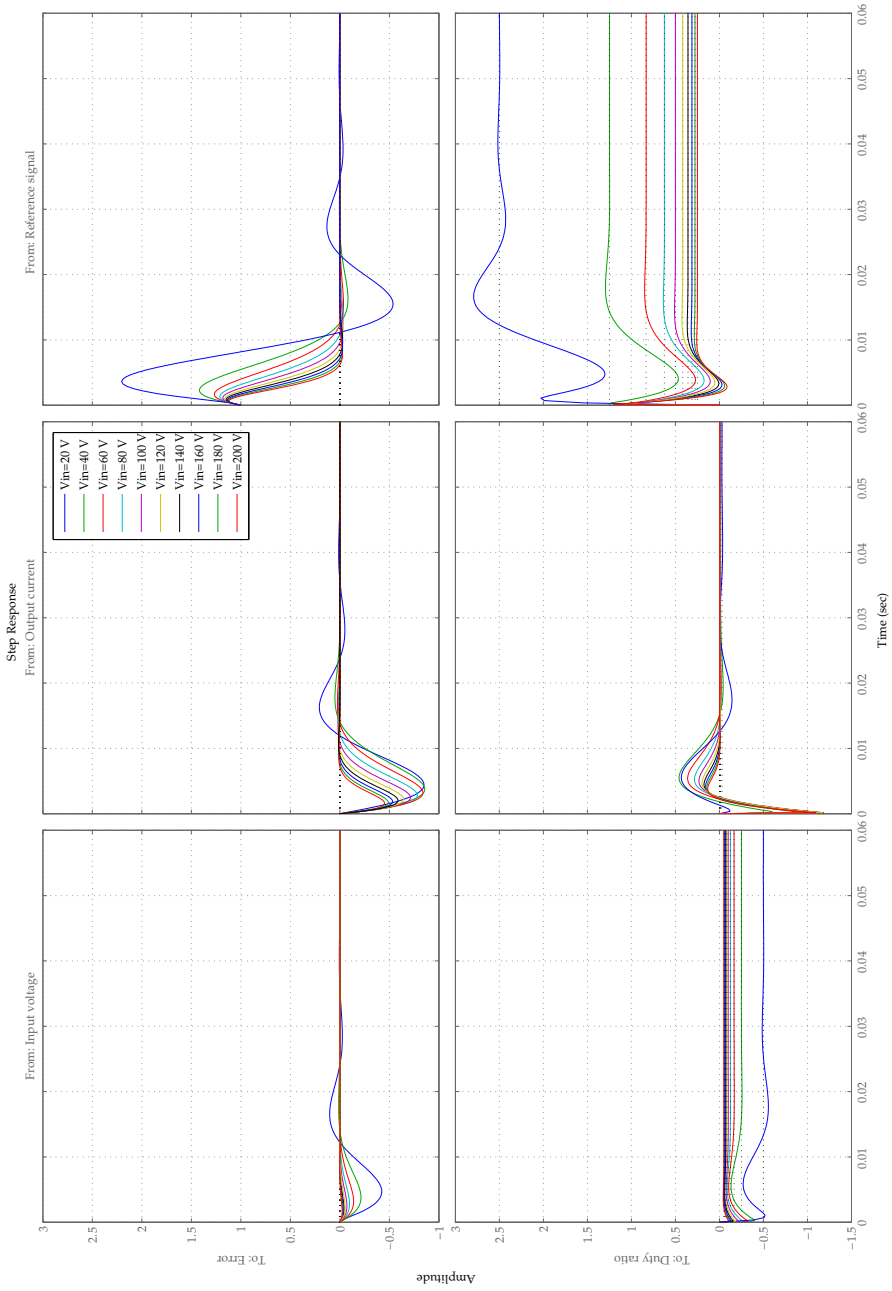

Figure B.6: Step responses for the closed $\mathcal{H}_\infty$-controlled system at various values of V_{in}, fixing D at 0.5 and I_L at 200 A.

Index

A

Adaptive control 70, 93
Air flow 67, 68, 131, 133, 137, 139
Anode 26, 31, 53, 126

B

Bulk composition 25, 53
Butler-Volmer equation **32**, 73

C

Carbon monoxide 5, 135
Cathode 31, 130
  Capacitance 26, 37
  Kinetics 31
Cell voltage 30
Charge double layer 24, 33
Companion form 104
Computational fluid dynamics 50
Continuity equations 26
Control
  Composition 130
  Power output 72
  Pressure 126
  Temperature 57, 76, **133**
    Cooling 57
    Heating 58
    Reference 135
Control structure 77
Controllability 95
Converter 70, 71, 75, **84**
  Boost 71, 85
  Buck 84
  Buck-boost 85
  Parameters 86
Correlation 36
Crossover current 31
CSTR reactor 12, 54

D

Dimensioning criteria
  Actuator power 133
  Actuator throughput 142
  Anodic manifold volume 129
  Oxygen composition reference . 139
Distributed layer thickness 29
Dynamic modes 71

E

Electric motors 88–90
  Control 90
Electrochemical impedance 38–40
Energy balance 57, 58
Equivalent layer thickness 28
Exchange current density 32, 51
Experimental uncertainty 14

F

Feedback control 4, 110, 127, 138
Feedforward control 101, 129, 138

Oxygen composition 131–133
Fuel cells 2
Alkaline 11
Alkaline methanol 67
Direct borohydride 3
Direct methanol 11, 12
Formic acid 3
Hydrazine 67
Microbial 3
Molten carbonate 49, 69
Proton-exchange membrane . 2, 49, 71
Solid oxide 2
Fuzzy control 69

G

Gain scheduling 93, 101
Gas humidification 3, 70

H

Half-delay filtering 102–104
Heat generation rate 126
$\mathcal{H}_\infty$ control 93
Mixed-sensitivity problem 95
Synthesis 97
Variable scaling 96
Weights 95
Hydrogen combustion 76, **136**, 140
Hysteresis 15

I

Input capacitance 88
Input-output linearisation 104
Instantaneous characteristic 41–44
Integrating process 127, 138
Internal dynamics 105
Stabilisation 109
Stability 107
Inverter 69

L

Lie derivative 105
Linear control 74
Lognormal distribution 29

M

Manifold 51
Dead end **51**, 76, 126
Purging 127
Open end **52**, 76, 130
Mass balance 56
Volume 128, 131
Mass-transport limit **28**, 53, 73, 126
Measurement dynamics
Oxygen composition 130
Pressure 127
Temperature 136
Model-predictive control 69
Modelling assumptions 26
MOSFET 38, 74
Multidisciplinarity 2, 71

N

Nafion 2, 3, 50, 51, 57, 61
Neural networks 69
New European Driving Cycle 124

O

Oscillation dampening 111
Overvoltage 24, **32**, 74
Oxygen conversion 126

P

Parameter regression 36

Phosphoric acid 4, 17, 31
Polarisation curve **15**, 41, 53
Polybenzimidazole . . **4–5**, 11, 57, 62, 135
Porosity 26
Pressure drop 61
Pseudo-steady state 134
Pulse-width modulation 71, **91–93**
Frequency 83, **93**, 96

R

Reaction current density 28, **32**
Reaction-site composition 25
Reversible cell potential 30
Right-hand plane zero 95

S

Sliding modes 113
Specific resistance 31
Stacks 3, 5, **60**, 74
Start-up 141
Stefan-Maxwell equations 5, 24, **26**
Simplified form 27
Stoichiometric ratio 70, 137
Switching rules 113
Computational performance . . . 119
Control performance 116
Synthesis 114
Symmetry factor 32

T

Tafel equation 24, **32**
Temperature profile 24, 59
Thevenin equivalent circuit . . 34, 49, 70
Time constants
Diffusion 27
Overvoltage 34
Experimental 17
Graphical representation 44
Oxygen composition 131
Temperature 137
Tortuosity 26

W

Warburg impedance 39
Water management **3–4**, 12, 50
Wind-up 129, 132